**Title**
The Water Neutron Detector (WaND)



**Author**
Asghari, Alexandra

**Publication Date**
2016

Peer reviewed|Thesis/dissertation

**The Water Neutron Detector (WaND)**

by

Alexandra Asghari

A dissertation submitted in partial satisfaction of the

requirements for the degree of

Doctor of Philosophy

in

Engineering – Nuclear Engineering

in the

Graduate Division

of the

University of California, Berkeley

Committee in charge:

Professor Karl van Bibber, Chair
Dr. Steven Dazeley
Professor Michael Nacht

Summer 2016

**The Water Neutron Detector (WaND)**

## Abstract

The Water Neutron Detector (WaND)

by

Alexandra Asghari

Doctor of Philosophy in Engineering – Nuclear Engineering

University of California, Berkeley

Professor Karl van Bibber, Chair

The Water Neutron Detector (WaND) is an efficient and non-toxic alternative to some helium-3 neutron counting applications. The detection volume is comprised of a 1.02 $m^3$ homogeneous mixture of deionized water doped with 0.5% $GdCl_3$. Following neutron capture, gadolinium emits an 8 MeV gamma shower, which in turn creates Cherenkov light that can be detected with photomultiplier tubes. The WaND is particularly well-situated to perform multiplicity counting of small samples because of its high efficiency of $(23.4 \pm 0.8)\%$ and short die-away time (15 $\mu$s). Due to the moderate gamma sensitivity, the WaND system may be suited for neutron-based nondestructive assay of small quantities of spent fuel. It is effective at measuring and identifying minute quantities of plutonium. Using a novel algorithmic approach, the WaND system can effectively differentiate between $^{252}Cf$ and $^{240}Pu$, as well as quantify the mass of $^{240}Pu$ in milligram quantities.

For my mom.
Thanks for being awesome.

# Contents

# List of Figures

# List of Tables

# Acknowledgments

The journey to my dissertation is full of amazing people, unlikely events, and a lot of hard work.

Without my mother, Margarita Holliday, I would live in a different world. I can't ever fully express my gratitude for the sacrifices you made to put me in an environment where I have a real future. Thank you.

My husband, Aaron Asghari, is my rock that keeps me rooted to the ground. Thank you for always being the voice of reason.

My advisers, Adam Bernstein, Steven Dazeley, and Karl van Bibber, supported and guided me to become a better scientist. Adam, thank you for always keeping me on track and being so supportive of my pursuits of science and policy. Your own career path has been a great inspiration to me. Steven, thank you for your infinite patience and answering every single question I ever had (perhaps also an infinite list). Only the most rigorous science made it past your attention to detail. Karl, thank you for always being a bring spark of inspiration in what was often a long and arduous experimental pursuit. Our discussions always reminded me why I was pursuing a PhD, and of the larger nature of the work we were doing.

My undergraduate mentors, William ("Dr. D") DeGraffenreid and Mani Tripathi were instrumental in showing me that I had the potential to pursue a graduate degree. Bill, thank you for never doubting the quirky nineteen year old girl that somehow wandered into the physics department. You always pushed me for bigger and better things, even when I had no idea of what I was capable. Mani, thank you for always being incredibly supportive and allowing me to pursue the opportunities that really defined my undergraduate career. A fleeting hallway conversation we had was one of the most important factors that influenced my decision pursue a graduate degree.

Also an enormous thank you to the great friends I made during my graduate career. You guys are amazing and provided a huge amount of support, without which this journey would have been a lot less fulfilling.

# Chapter 1

# Introduction

## 1.1 Foundations

On July 16, 1945, the United States conducted the world's first nuclear test; the following August, nuclear weapons were deployed to decimate Hiroshima and Nagasaki. Within two decades, the USSR, the UK, France, and China had also tested nuclear weapons. In a 1963 news conference, John F. Kennedy stated that he is "haunted by the feeling that by 1970 ... there may be ten nuclear powers instead of 4, and by 1975, 15 or 20" [1]. Over fifty years later, there are eight known states with nuclear weapons, and one more suspected. This lower-than-anticipated number could be viewed as a success of the international community, but the increasingly turbulent international atmosphere and development of potentially disruptive technologies means that curbing the spread of nuclear capabilities is nonetheless a long-term task.

International collaboration to stem the spread of nuclear weapons can be traced to the pivotal 1953 *Atoms for Peace* speech, in which President Dwight D. Eisenhower pledged that the U.S. would devote its "entire heart and mind" to solving the "fearful atomic dilemma" [2]. He also proposed the establishment of an International Atomic Energy Agency (IAEA) to encourage and facilitate peaceful uses of fissionable material, diminish the destructive power of the world's nuclear stockpiles, demonstrate that the great powers of the world are "interested in human aspirations first rather than in building up armaments of war," and serve as a channel for international cooperation [2].

The legal framework under which the IAEA operates is called the *Treaty on the Non-Proliferation of Nuclear Weapons* (conventionally the "non-proliferation treaty," NPT), which entered into force in 1970. It is designed to curb the spread of nuclear weapons and weapons technology, encourage cooperation for the peaceful use of nuclear power, and promote the goal of nuclear (and general) disarmament [3]. The NPT is considered the foundation of nuclear nonproliferation, with 191 states party to the treaty.

## 1.2 Role of the IAEA in international safeguards

Under the NPT, the objectives of the IAEA are twofold: to "accelerate and enlarge the contribution of atomic energy to peace, health and prosperity throughout the world" and to aid in the "supervision or control" of nuclear materials to ensure that this assistance "is not used in such a way as to further any military purpose" [4]. To this end, the IAEA encourages, assists, and fosters research, development, and scientific exchange on practical applications of atomic energy for peaceful uses. The organization also establishes and administers safeguards in non-nuclear-weapon states to prevent nuclear, or nuclear-related, material from being used for any military purpose [4].

The objective of IAEA safeguards is to preclude the diversion of civilian nuclear materials for military functions. IAEA safeguards are designed to detect the misuse of nuclear material or technology, provide credible assurances that states are abiding by their NPT obligations, and build confidence in the international nonproliferation regime by deterring the misuse of nuclear material and technology. The *Comprehensive Safeguards Agreement* gives the IAEA the right and obligation to ensure that safeguards are applied to all non-nuclear states' nuclear material, and that such material is not diverted for nuclear weapons or other nuclear explosive devices [5]. The technical objective of this agreement is

> the timely detection of diversion of significant quantities of nuclear material from peaceful nuclear activities to the manufacture of nuclear weapons or of other nuclear explosive devices or for purposes unknown, and deterrence of such diversion by the risk of early detection [6].

Alongside this definition, the statutes of the IAEA define *special fissionable material* – nuclear material that can be used to create a nuclear weapon – as $^{239}$Pu, $^{233}$U, uranium enriched in the isotopes $^{233}$U or $^{235}$U, or any combination thereof. Enrichment in $^{233}$U or $^{235}$U means that the material in question contains a ratio of either or both of these isotopes higher than that found in nature [6]. The terms *special fissionable material* and *special nuclear material* are used interchangeably in this dissertation. A significant quantity is the "approximate amount of nuclear material for which the possibility of manufacturing a nuclear explosive device cannot be precluded" [7], as defined as in Table 1.1. The timeliness detection goal is the target detection time for certain materials, and establishes the frequency of inspections. Direct use material, or unirradiated fuel, such as highly enriched uranium (HEU) which does not contain substantial amounts of fission products would require less time and effort to be weaponized and therefore has a shorter timeliness goal. Irradiated direct use material (such as plutonium in spent fuel) contains substantial amounts of fission products and would require more time and effort to be weaponized, and has a longer timeliness goal [7].

The IAEA employs a variety of means to verify the correctness and completeness of states' nuclear materials declarations, both human (such as open-source information gathering and satellite image analysis) and technical (including tamper-evident seals, cameras, physical monitor facilities, and radiation detectors). Radiation detectors play an especially important role in the non-destructive assay of radioactive material, including special nuclear material.

Table 1.1: IAEA significant quantity and timeliness goals [7]

| Material | Significant quantity | Timeliness detection goal |
|---|---|---|
| Pu | 8 kg Pu | one month for unirradiated, three months for irradiated |
| $^{233}$U | 8 kg $^{233}$U | |
| HEU$^{\star}$ | 25 kg $^{235}$U | |
| LEU$^{\dagger}$ | 75 kg $^{235}$U$^{\ddagger}$ | one year |
| Th | 20 tonnes Th | |

$^{\star}$ *Highly enriched uranium,* $^{235}U > 20\%$
$^{\dagger}$ $^{235}U < 20\%$
$^{\ddagger}$ *Or 10 tonnes natural U, or 20 tonnes depleted U*

Neutron detectors are particularly useful for identifying and potentially quantifying nuclear material because such material emits a relatively large number of neutrons in a burst-like temporal pattern – a signature not found often in nature.

Neutron detectors based on helium-3 comprise "essentially all" [8] neutron detectors used by the IAEA, and as such the IAEA is functionally reliant on helium-3 for this component of its detection capabilities. Table 1.2, adapted from *IAEA Safeguards Techniques and Equipment: 2011 Edition*, summarizes the neutron detectors in use by the IAEA – *all* of which are based on helium-3. It is therefore worthwhile to explore the source of the IAEA's helium-3, and to analyze its availability for safeguards instrumentation.

## 1.3 Case study: IAEA inspection at the Rokkasho Reprocessing Plant

The Rokkasho-mura Reprocessing Plant (RRP) is the largest commercial spent fuel reprocessing facility, and poses a major safeguards challenge for the IAEA. This short case study is illustrative of practical IAEA safeguards verification methodologies.

The RRP is designed to process ∼800 metric tons of spent nuclear fuel and recover ∼8 metric tons of plutonium annually. The RRP is safeguarded by the Japanese government (including the Japan Safeguards Office) and the IAEA. The IAEA must be able to draw conclusions of "nondiversion of declared nuclear material and the absence of undeclared nuclear material and activities" [9]. In order to do so, the IAEA relies on comprehensive and diverse verification measures including materials accountancy, process monitoring, inspection and verification, and containment and surveillance [9].

The accountancy structure is divided into five material balance areas (MBA). Verification is performed at all material entrance and exit points for each MBA. Samples that are taken from each MBA analyzed at the On-Site Laboratory (OSL) [10]. For example, solid waste in the form of leached hulls and fuel end-pieces are verified by measuring the $^{244}$Cm content using the Rokkasho Hulls Monitoring System (RHMS) at the OSL. The RHMS consists of

Table 1.2: Summary of neutron detectors used by the IAEA.

| Code | Equipment name | Primary measurement |
|---|---|---|
| | *Gross neutron counters* | |
| HHNM | Hand-held neutron monitor | Localizing neutron radiation sources |
| PNUH | Portable neutron uranium hold-up | Uranium hold-up in enrichment plant cascade halls |
| | *Passive neutron coincidence counters* | |
| BCNC | Birdcage neutron counter | Plutonium mass in special storage configurations |
| DRNC | Drawer counter | Plutonium mass in facility-specific containers |
| FAAS | Fuel assembly/capsule assay system | Plutonium mass in MOX fuel assemblies |
| FPAS | Fuel pin/pallet assay system | Plutonium mass in MOX fuel pins |
| GBAS | Glovebox assay system | Plutonium hold-up in gloveboxes |
| HBAS | Hold-up blender assay system | Plutonium hold-up in facility blenders |
| HLNC | High-level neutron coincidence counter | Plutonium in 20-2000 g canned samples |
| INVS | Inventory sample counter | Plutonium in 0.1-300 g samples |
| LNMC | Large neutron multiplicity counter | Plutonium in contaminated/impure items |
| MAGB | Material accountancy glovebox counter | Plutonium mass in facility gloveboxes |
| PCAS | Plutonium canister assay system | Plutonium mass in MOX canisters |
| PNCL | Passive neutron coincidence collar | Plutonium mass in MOX fuel assemblies |
| PSMC | Plutonium scrap multiplicity counter | Plutonium in 1-5000 g canned samples of scrap |
| PWCC | Passive well coincidence counter | Plutonium mass in CANDU MOX fuel bundles |
| UFBC | Universal fast breeder counter | Plutonium ( 16 kg) in fast breeder reactor fuel |
| UWCC | Underwater coincidence counter | Plutonium in fresh MOX fuel assemblies |
| | *Active neutron coincidence counters* | |
| AWCC | Active well coincidence counter | Uranium-235 in highly enriched uranium samples |
| UNCL | Uranium neutron coincidence collar | Uranium-235 in low enriched U fuel assemblies |
| WCAS | Waste crate assay system | Waste materials |
| WDAS | Waste drum assay system | Low-level waste drums for plutonium mass |

three helium-3 detectors to actively and passively interrogate samples. The passive phase of the measurement cycle measures the number of single neutrons emitted from $^{244}$Cm, then the plutonium and uranium content can be calculated from the Pu/Cm and U/Cm ratios of the solvent [11]. Neutron detection is also used in the accountability tank to determine the $^{244}$Cm content, in the product measurements to measure the plutonium mass in canisters in temporary storage, and in glove box assay of the holdup plutonium content [9].

The results of the OSL measurements are compared to the declared materials in a manner similar to a financial book inventory. The book inventory is determined as the gross product after additions and subtractions of material. The IAEA will determine the shipper/receiver differences to ensure that no material is unaccounted for and material unaccounted as a quality indicator of the control of nuclear material. The IAEA relies heavily on helium-3 neutron detectors for the safeguards verification of the RRP, which poses a potential weak point in the international safeguards regime, as is shown in the following section.

## 1.4 The helium-3 shortage

Because the United States is "the major supplier" [12] of helium-3 to the IAEA, the effectiveness of safeguards is tied directly to the United States's federal stockpile of the material. However, as demonstrated in Figure 1.1, the U.S. helium-3 reserve is in decline following a peak around the year 2000.

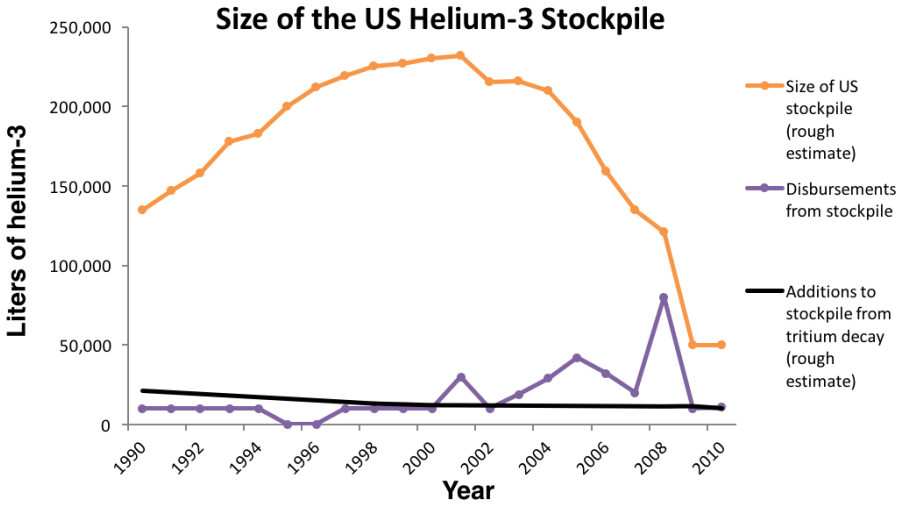


Figure 1.1: Additions, disbursements, and total size of the U.S. federal helium-3 supply.

Because helium-3 comprises only one part per million of naturally occurring helium, it has historically been harvested as a by-product of tritium decay in the nuclear weapons complex. Therefore, the supply and demand for tritium and *not* helium-3 – determines the helium-3 supply [13].

The U.S. supply of helium-3 is severely limited due to the halt in nuclear weapons production. From 1955 to 1988, the Department of Energy (DOE) produced approximately 225 kilograms of tritium at the Savannah River Site in Georgia, and on a smaller scale at the Hanford Reservation in Washington State [14]. However, due to the isotope's 12.32-year half-life, only about 26 kilograms of tritium produced during this period remains in 2015. The U.S. continues to replenish its tritium supply by recycling existing tritium from dismantled nuclear warheads, and limited tritium production was resumed at the Watts Barr reactor near Chattanooga, Tennessee in 2003 to maintain a five-year reserve supply. However, by 2010 tritium leakage into the Watts Barr reactor's coolant water had reached near-regulatory limits, and as a result the amount of tritium produced fell [15]. From this limited supply, the Savannah River Site Tritium Facility recovers, purifies, and bottles helium-3 before shipping it to Linde Electronics and Specialty Gasses in Munich, where it is sold to customers or vendors under the direction of the U.S. federal government [16].

The demand for helium-3 has nonetheless increased dramatically since 1955 due to the discovery of novel uses for the isotope – such as in neutron detectors. After 2001, increased concern about nuclear terrorism led the U.S. Department of Homeland Security to rapidly increase the number of deployed helium-3 radiation portal monitors (RPMs) [13]. Neutron detectors based on helium-3 are now used in over 1,400 domestic and 2,000 overseas RPMs at ports and border crossings to detect the trafficking of illicit nuclear material. Large-area neutron detectors for conducting materials research in medicine, energy, and transportation also rely on helium-3 [13].

Although the U.S. helium-3 stockpile began to decrease in 2001, efforts to resolve the discrepancy between additions to and disbursements from the stockpile did not begin until 2009, when the Interagency Policy Committee (IPC) was created to address the shortage. The IPC concluded that helium-3 allocation for RPMs should cease, and future allocations follow more stringent criteria. Domestically, the IPC recommendations resulted in the regulation of helium-3 allocations to conserve the remaining stockpiles, but these efforts are insufficient to sustainably provide helium-3 for both domestic applications and the international safeguards regime because the supply is limited by tritium production [17]. This shortage has caused prices to increase significantly. In 2010, the cost of helium-3 purchased through the DOE Isotopes Program was between $100 and $400 per liter; in 2011, the price per liter was $600 to $1000 [17, 18, 19]. Further, helium-3 prices outside the heavily subsidized U.S. market are even higher – for example, in 2011 helium-3 was available on the commercial market from Linde for $2,400 per liter [18, 19].

The uncertainty of supply levels, the eventual depletion of existing stockpiles, and the cost increases on the open market have all coalesced to further strain the IAEA's technical capability [8]. Supply disruptions caused by the dwindling stockpile in the United States are already evident: as of 2011, the U.S. has severely reduced allocations for safeguards (and for IAEA safeguards in particular), creating an uncertainty about future helium-3 availability [8]. Short-term ramifications aside, the IAEA cannot rely on helium-3 for neutron detection in the future because the material is intimately tied to nuclear weapons. Simply put, if the ultimate goal of the NPT is nuclear disarmament, then the IAEA cannot rely on a nuclear weapons-derived material for inspection. It is of international interest to develop neutron detectors not based on helium-3.

## 1.5 Spent fuel nondestructive assay

Though still an unsolved problem, neutron multiplicity counting (measuring the number of times a single, double, or triple neutron coincidence occurs within a specified time window) of spent fuel potentially offers a direct measurement of plutonium content. The Next Generation Safeguards Initiative (NGSI) of the U.S. Department of Energy has identified plutonium mass determination in spent fuel a high priority. Currently, the IAEA looks for gross or partial defects of spent fuel assemblies. Gross defects are those in which the entire assembly is either missing or has been replaced with a dummy, while partial defects involve

one-half or more of the assembly rods as missing or dummies. Gross measurement is problematic because the core of a typical pressurized water reactor (PWR) can contain roughly 330 kg of plutonium, about 170 kg of which is $^{239}$Pu – 40 significant quantities (assuming a 1,000 MWe PWR, with a thermal efficiency of 33%, capacity factor of 90%, average burnup of 45 MWd/kgU, and refuel cycle of 1.5 years) [20]. The ability to recover plutonium from spent fuel greatly decreases the breakout time – the amount of time needed to obtain one weapon's worth of nuclear material – compared with enriching uranium. Though the high activity of spent nuclear fuel creates a radiation barrier that hinders separation of plutonium, a reprocessing facility makes chemical separation a possibility. The estimated breakout time for a state with reprocessing capabilities is as little as days to weeks [21].

Spent fuel nondestructive assay (NDA) is currently achieved by the use of the Cherenkov Viewing Device, Fork Detector, and Safeguards MOX Python Detector. The Cherenkov Viewing Device measures the induced Cherenkov signal from fission products, while the Fork Detector and Python Detector measure gamma emission from fission products and neutron emission primarily from curium in spent-fuel cooling ponds. Burnup codes are then used to infer plutonium mass. Direct plutonium mass determination would improve recovery from a loss of continuity of knowledge, quantify the input accountability mass at processing and reprocessing facilities, and quantify plutonium mass to determine shipper/receiver differences. A greater precision of plutonium measurement in spent fuel would aid in deterring the diversion of plutonium from such fuel [22].

## 1.6 Problem statement

This dissertation focuses on developing and characterizing a high fidelity non-helium-3 detector.

First, there is a need for neutron detectors not based on helium-3. The convergence of the global helium-3 shortage with the IAEA's heavy reliance on this isotope has created potential instability in the international safeguards regime. In order for the IAEA to continue to safeguard nuclear material, the viability of detection capabilities must be ensured into the long-term future.

Next, the development of an extremely high fidelity neutron detector that can detect and identify minute amounts of plutonium is beneficial for national and international security. The characterization of minute quantities of residual plutonium on plutonium-contaminated waste would aid in nuclear waste disposal. Internationally, measuring minute quantities of plutonium would aid in the on-site inspection of reprocessing facilities such as the RRP.

Reducing the error on spent fuel plutonium evaluation through more precise measurement decreases the detection timeline, and direct measurement of plutonium in spent fuel can increase the efficacy of deterrence measures. As such, there is a clear need for a non-helium-3 neutron detector that can directly measure plutonium in spent fuel.

## 1.7 Thesis outline

In response to the need for high fidelity alternative neutron detection measures, this dissertation explores the Water Neutron Detector (WaND).

This dissertation first introduces the public policy foundations of the subsequent technical research, then introduces technical background information regarding neutron counting and the WaND. The first research part of this dissertation examines neutron multiplicity and plutonium identification and mass measurements. The second part analyzes neutron detection in the presence of a high gamma flux.

Chapter 2 introduces the theoretical underpinnings of fission neutron multiplicity and offers a survey of current neutron-counting modalities. Chapter 3 describes the WaND detector and data analysis techniques that are used to differentiate between gamma and neutron detector responses. Chapter 4 addresses measuring the neutron multiplicity of various sources, including californium and plutonium. Chapter 5 discusses the issue of measuring neutrons in the presence of a high gamma background. Lead shielding and software padding can mitigate the gamma detector response. Chapter 6 offers an analysis of the feasibility of the WaND detector in IAEA safeguards, and discusses potential future research and development.

# Chapter 2

# Neutron Counting Principles

Compared with electromagnetic radiation, neutrons are rarely found in the ambient environment. Fission, however, produces a relatively large number of time-correlated neutrons, and neutron counting emphasizes the temporal rather than energetic signature of events. The analysis in this chapter forms the basis for neutron coincidence counting as a nondestructive assay (NDA) technique. Specifically, the origin, characteristics, and sources of fission neutrons are discussed, followed by the relationship between the inter-event time distribution of measured neutrons and the factors that influence it. The relationships between single, double, and triple coincidences are explored, as well as the potential to measure higher multiplicities. Alternate neutron detection technologies and detector requirements are also briefly outlined.

## 2.1 On the Origin of Neutrons

The energetic preference for certain nuclei to fission can be understood from the binding energy curve (see Fig. 2.1), as isotopes transform in order to maximize the binding energy per nucleon. It is energetically favorable for heavy nuclei (A>90) to fission either spontaneously or by induced processes. For example, the binding energy per nucleon of $^{238}$U is roughly 7.6 MeV/nucleon; however, if $^{238}$U were to split into two equal parts of atomic weight $\simeq$119, the binding energy would be 8.5 MeV/nucleon. The excess *approximately* 200 MeV is released in the products of fission. Approximately 80% (165 MeV) of that is carried by the kinetic energy of the fission fragments. About 5 MeV is shared between the kinetic energy of the $\sim$2.5 neutrons released at the instant of fission (emitted within $10^{-16}$ seconds of fission). Another $\sim$8 MeV is released in prompt gammas (within $10^{-14}$ seconds). Roughly 19 MeV is split between $\beta$ particles and antineutrinos. The remainder $\sim$8 MeV is emitted from the $\gamma$ decay of radioactive fragments [23].

More formally, total nuclear binding energy can be described as follows:

$$B = a_v A - a_s A^{2/3} - a_c Z(Z-1)A^{-1/3} - a_{sym}\frac{(A-2Z)^2}{A} + \delta, \tag{2.1}$$

where

$B$ = total binding energy of the nucleus,
$A$ = mass number,
$Z$ = proton number,
$\delta$ = pairing term, and
$a_v,\ a_s,\ a_v,\ a_c,\ a_{sym}$= constants:
$a_v = 15.5$ MeV,
$a_s = 16.8$ MeV,
$a_c = 0.72$ MeV,
$a_{sym} = 23$ MeV, and
$a_p = 34$ MeV

In the lowest-order approximation, total nuclear binding energy is proportional to the mass number $B \propto A$, and is given as $a_v A$. The second term in Eq. 2.1 corrects for nucleons that are on the surface of a nucleus and are less tightly bound than those in the central region. The nuclear surface area is proportional to $R^2$, or $A^{2/3}$ as $R \propto A^{1/3}$, and thus the surface-area term is $a_s A^{2/3}$. Coulomb repulsion of the protons also makes the nucleus less tightly bound. Because each proton repels all others in the nucleus, this term is proportional to $Z(Z-1)$ and is given as $a_c Z(Z-1)$. The symmetry term $a_{sym}(A-2Z)^2/A$ favors nuclei with $Z \simeq N$. The pairing force $\delta$ plays a large role in determining which candidate nuclei fission by spontaneous or induced fission; binding energy is increased for paired like nucleons (i.e., even $Z$ or even $N$), and the pairing force is expressed as $+a_p A^{-3/4}$ for even $Z$ and even $A$, $-a_p A^{-3/4}$ for odd $Z$ and odd $N$, and zero for odd $A$. The pairing term increases or decreases the energy needed for fission for odd and even $A$ isotopes, respectively. For example, $^{235}$U readily fissions with the absorption of a thermal neutron, while $^{238}$U requires an $\sim$1 MeV neutron for fission [23].

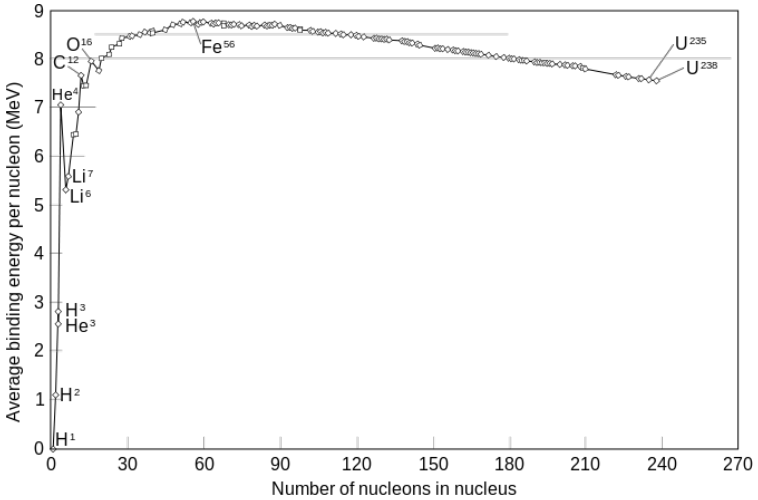


Figure 2.1: Binding energy per nucleon [24].

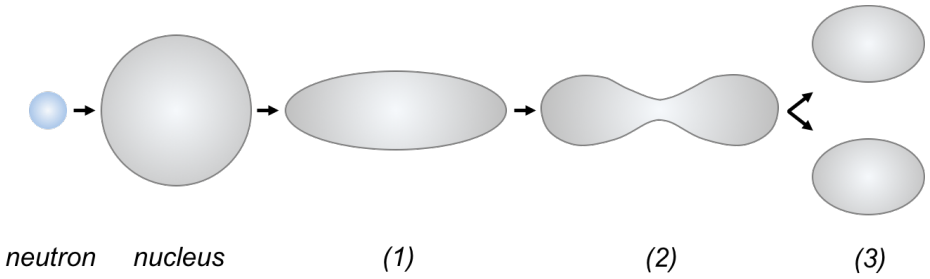


Figure 2.2: A schematic diagram of nuclear shapes during fission. A neutron incident on a nucleus can excite vibrational modes (1 and 2). As the stretching becomes more extreme, the two lobes can separate (3). Adapted from [23].

Fig. 2.2 shows a representation of the fission process. Upon neutron capture, a nucleus can enter vibrational excited states that cause it to stretch. The potential energy of the two lobes can be represented as the potential energy of two fission fragments at various separations. Fig. 2.3 shows this potential energy, from a nearly spherical state at zero separation (the parent nucleus) to complete separation and beyond. The parent nucleus exists in the shallow potential well at low separation distances, and in order for fission to occur it must either gain the activation energy or tunnel through the barrier. If the potential energy of the separated configuration is lower than the conglomerated state and the activation energy is zero, the nucleus instantaneously fissions. If the potential energy is lower than the original configuration and the activation energy is positive yet low, the nucleus can fission. If the activation energy is high enough that spontaneous fission is not observed, the absorption of a relatively low amount of energy (from a photon or neutron) might form a compound nucleus whose fission probability successfully competes with other modes of decay. If the activation energy is even higher, the absorption of a higher-energy particle might be necessary for fission [23].

Table 2.1 (adapted from [25]) shows some common fissioning isotopes relevant to nuclear nonproliferation detection efforts. $^{235}$U and $^{238}$U are common materials in nuclear fuel and weapons, depending on enrichment and matrix composition (metallic or oxide). $^{239}$Pu and $^{240}$Pu are bred in reactor cores, and plutonium with a low ratio of $^{240}$Pu/$^{239}$Pu is favorable for weapons purposes. $^{242}$Cm is a major neutron emitter for spent nuclear fuel, and is often used as a proxy for the plutonium measurements of such fuel. $^{252}$Cf is generally used as a laboratory source, and has a remarkably high neutron emission rate. There is a difference of many orders of magnitude for spontaneous fission yield among $^{239}$Pu, $^{240}$Pu, and $^{242}$Cm, which poses a major technical challenge in identifying $^{239}$Pu based on neutron counting.

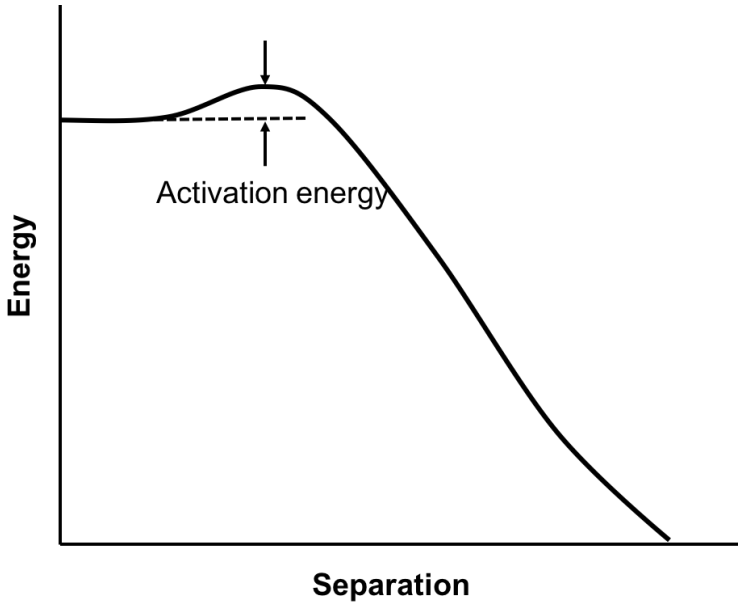


Figure 2.3: Schematic of the potential energy of fission, modeled as the potential energy between two fission fragments. Adapted from [23].

Table 2.1: Selected isotopic neutron sources relevant to nuclear nonproliferation [25].

| Isotope | Total half-life | Spontaneous fission half-life (yr) | Spontaneous fission yield (neutrons/s×g) | Spontaneous fission neutron multiplicity |
|---|---|---|---|---|
| $^{235}$U | $7.04 \times 10^8$ yr | $3.5 \times 10^{17}$ | $2.99 \times 10^{-4}$ | 1.86 |
| $^{238}$U | $4.47 \times 10^9$ yr | $8.20 \times 10^{15}$ | $1.36 \times 10^{-2}$ | 2.1 |
| $^{239}$Pu | $2.41 \times 10^4$ yr | $5.48 \times 10^{15}$ | $2.18 \times 10^{-2}$ | 2.16 |
| $^{240}$Pu | $6.56 \times 10^3$ yr | $1.16 \times 10^{11}$ | $1.02 \times 10^3$ | 2.16 |
| $^{242}$Cm | 163 days | $6.56 \times 10^6$ | $2.10 \times 10^7$ | 2.54 |
| $^{252}$Cf | 2.646 yr | 85.5 | $2.34 \times 10^{12}$ | 3.757 |

## 2.2 Fission neutron characteristics

Though the typical energy release in fission is approximately 200 MeV, neutrons carry away only a few MeV in energy. Fig. 2.4 shows the neutron energy spectrum from spontaneous fission of $^{252}$Cf, modeled by a Maxwellian distribution with an average energy of 2.14 MeV. The energy distribution is $N(E) = \sqrt{E}e^{-E/a}$, where $N(E)$ is the probability at energy $E$ and $a$ is a constant that depends on the isotope ($a = 1.43$ for $^{252}$Cf) [25].

The number of prompt fission neutrons emitted per fission is called the *neutron multiplicity*. The probability that $\nu$ neutrons are emitted in a fission follows a Gaussian distribution

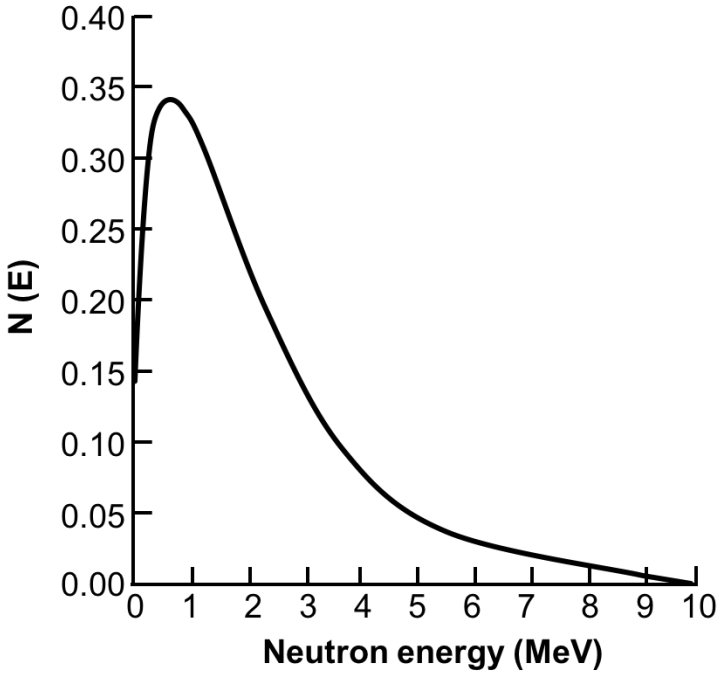


Figure 2.4: $^{252}$Cf spontaneous fission neutron energy distribution [25].

and is given by

$$P(\nu) = \frac{1}{\sqrt{2\pi\sigma^2}} e^{-(\nu-\bar{\nu})^2/2\sigma^2},$$

where $P(\nu)$ is the probability that $\nu$ neutrons are emitted, and the Gaussian width is $\sigma = 1.21$ for $^{252}$Cf and $\sigma = 1.08$ for all other isotopes.

Appendix A more specifically tabulates the multiplicity distributions of several isotopes of interest, and Fig. 2.5 shows the same data plotted graphically. Note that although the distributions follow a Gaussian shape, some are clearly distinguishable from others, such as $^{238}$Pu and $^{252}$Cf. It might be possible to identify pure or mixed fissioning sources based on the measured neutron multiplicity distributions.

All multiplicity distributions are normalized to unity and have a mean value $\nu_1$ [26]:

$$\sum_{\nu=0}^{max} P(\nu) = 1 \tag{2.2}$$

and

$$\sum_{\nu=0}^{max} \nu P(\nu) = \nu_1. \tag{2.3}$$

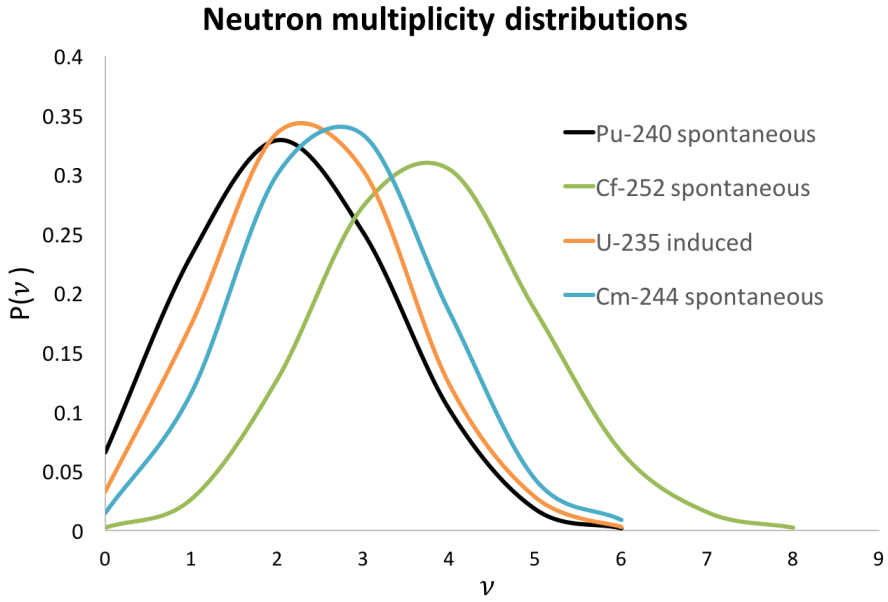


Figure 2.5: Neutron multiplicity distributions $P(\nu)$ for the isotopes listed in Appendix A.

## 2.3 Neutron counting

Because neutrons can be a telltale signature of fission, fission neutron characteristics are important in nuclear safeguards – in particular, the unique temporal signature of fission neutrons can be utilized in neutron multiplicity counting to assay the sample. *Multiplicity counting* refers to recording the occurrence of single, double, and triple neutron coincidences. Singles counting tracks the number of single neutrons detected, and is the simplest and most widely used form of neutron counting in applications including neutron-source location and dose measurement. Doubles counting tracks the rate of a coincidence of two neutrons within a designated time window, and can be employed to gain information about a fissioning isotope. Multiplicity counting tracks the occurrence of the coincidence of 1, 2, 3, ... neutrons within a given time window. Although it is more complex than singles or doubles counting, multiplicity counting offers deeper insights into the nature of a fissioning isotope because it requires fewer assumptions [27].

Neutron counting is much more useful than spectroscopy for most neutron measurements (including safeguards) because it is far simpler and because environmental neutron moderation can be unpredictable

### 2.3.1 Inter-event time distribution

The event times can be used to create inter-event time and multiplicity distributions. Historically, this was done with analog electronics and shift registers; however, modern digital

DAQ systems can record all events that meet certain threshold requirements and perform software-based multiplicity analysis. For example, inter-event times can be used to generate a multiplicity distribution simply by keeping a running tally of the number of neutron events following an initial trigger event.

When a fission occurs, a burst of neutrons is emitted almost instantaneously (within $10^{-16}$s of fission [23]); however, background events generally occur at random intervals. Particles, including neutrons, that originate from a single physics event are therefore designated as correlated, and those that do not are uncorrelated. A neutron counter monitoring a source of neutrons (such as a fissioning isotope) will measure both correlated and uncorrelated particles, but a timing analysis can highlight features of either.

The *inter-event time distribution*, shown in Fig 2.6 gives the likelihood that following an initial event, a second event will occur a certain time later. The distribution includes uncorrelated events that originate from a random coincidence and can have a relatively long inter-event time. A portion of events will occur due to correlated events, which originate from the same physics event (such as a fission) and have a relatively short inter-event time. However, due to the random nature of these events, some uncorrelated events will occur within a relatively short timescale and appear in the same inter-event time region as correlated events. Further, uncorrelated and correlated events can mix together to create mixed signals. Therefore an individual event from Fig. 2.6 cannot be classified as correlated or uncorrelated a priori. However, the relative number of uncorrelated and correlated events can be deduced by fitting the distribution.

Following an event at $t = 0$, the probability that the next event from a set of uncorrelated random events will take place in a time period of $dt$ after a delay of $t$ is given by the product of the probability of no events occurring from 0 to $t$ multiplied by the probability of an event occurring during $dt$. Specifically,

$$I(t)dt = P(0) \times r\ dt \tag{2.4}$$

and the Poisson probability of no events from 0 to $t$ is

$$P(0) = \frac{(rt)^0 e^{-rt}}{0!} = e^{-rt}. \tag{2.5}$$

Combining Equations 2.4 and 2.5 leads to

$$I(t)dt = re^{-rt}dt, \tag{2.6}$$

where the distribution of intervals between adjacent random events exponentially decreases with time. Equation 2.6 can be modified to include multiple terms, such as a source term and a background term that have differing emission rates. The most probable interval is zero, and the mean is

$$\bar{t} = \frac{\int_0^\infty tI(t)dt}{\int_0^\infty I(t)dt} = \frac{\int_0^\infty tre^{-rt}dt}{1} = \frac{1}{r},$$

where $r$ is the average rate.

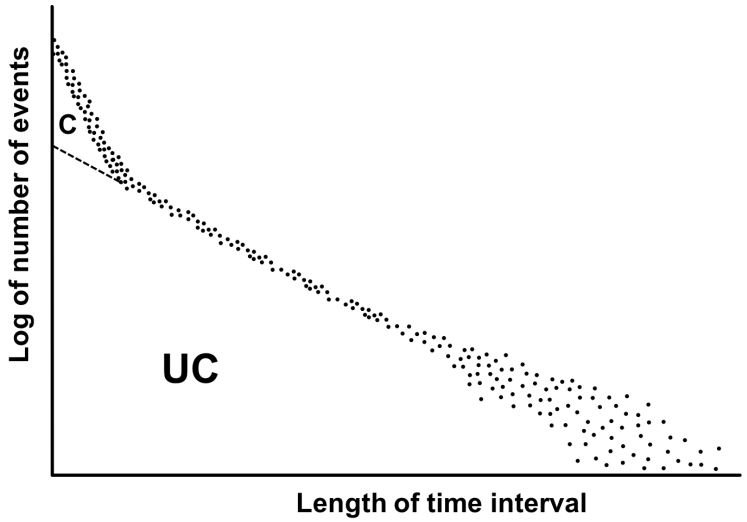


Figure 2.6: An inter-event time formed by correlated (C) and uncorrelated (UC) coincidences. Adapted from [25].

### 2.3.2 The Rossi-$\alpha$ distribution

The unique burst-like nature of fission neutrons can be exploited by neutron counting. This discussion is based on the historical nomenclature of uncorrelated coincidences described as "accidentals" (A) and correlated coincidences as "reals" (R). Historically, neutron counting relied on shift-register electronics that count the number of neutrons within a predesignated gate width (G). Two neutron events within a time coincidence can originate from a single fission event (a real coincidence) or from uncorrelated events, such as two background events (an accidental coincidence). The Rossi-alpha distribution shown in Fig. 2.7 describes the number of detected events at a given time after an initial trigger neutron event at time $t = 0$. Following a short pre-delay gate P, the next gate G contains both accidental coincidences A and real correlated events R. After a long delay gate D (typically $1000\mu s$), the next gate G measures only the accidental coincidences A. Because the rate of A is constant in time, the subtraction of the second gate G (only A) from the first gate G(R+A) gives the true coincidence rate R.

Within the first gate G, correlated events, which originate from a single physics event, produce an exponentially-decaying distribution in time. The number of neutrons counted at time t after an initial trigger at $t = 0$ is given by [25]:

$$N(t) = A + Re^{-t/\tau},$$

where $\tau$ the die-away time. Die-away time depends on the size, shape, composition, and efficiency of the neutron counter, and is $\sim 30$ to 100 $\mu s$ for typical $^3$He-based systems. Short die-away times allow for a shorter G, reducing the probability of false-positive coincidence

events [25], [28]. At very short times, a pre-delay gate of $P \sim 3$ to 6 $\mu s$ eliminates pulse pileup and deadtime issues [25].

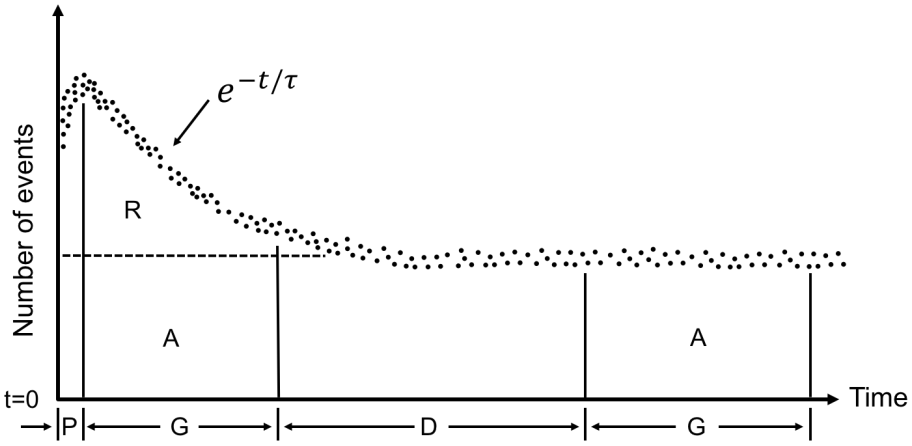


Figure 2.7: An example of the Rossi-alpha distribution. $R$ shows real coincidence events, $P$ is the predelay, $G$ shows the prompt and delayed gates, $D$ is the long delay, and $\tau$ is the die-away time. Adapted from [25].

The Rossi-$\alpha$ analysis was developed for analog and fixed-gate electronics. However, with flexible gate widths and digital electronics, it is not necessary to measure and analyze the Rossi-$\alpha$ distribution because all triggers can be recorded and analyzed post-process.

### 2.3.3 Multiplicity counting mathematics

This section outlines the factors that influence traditional neutron multiplicity counting and how measured quantities can be utilized to determine plutonium mass. The techniques outlined here form the basis of neutron multiplicity counting with fixed-gate time windows. A discussion of an updated method that was developed as a part of this dissertation will be discussed in latter chapters.

A number of factors affect the measured neutron multiplicity: the spatial variation in neutron detection efficiency, the energy spectrum effects on detection efficiency, the energy spectrum of the $(\alpha, n)$ neutrons, the spatial variation of neutron multiplication, neutron capture in the sample, neutron die-away in the detector, sample multiplication, the $(\alpha, n)$ production rate in the sample, and the sample spontaneous fission rate. The latter factor is the signature of most interest. This section examines how each of these factors is obtained and used to mathematically solve for sample plutonium mass.

Neutron counting was developed because of the penetrability of neutrons – they are readily shielded only by hydrogenous materials and by some isotopes that absorb them. However, singles counting cannot accurately assay a sample of plutonium because this method requires

many assumptions. Doubles counting is an improvement, in that it can identify the occurrence of correlated neutrons that point to fission. Doubles counting is also not directly influenced by the $(\alpha, n)$ rate, as the reaction does not produce time-correlated neutrons. However, even singles and doubles rates together cannot definitively assay a fissioning sample – assumptions must be made regarding either mass, self-multiplication, or $(\alpha, n)$ rate, and incorrect assumptions can lead to large error bars or unreliable results. Multiplicity counting increases the number of measured quantities for more accurate plutonium assay [27].

The detection of neutrons originating from a fissioning sample can generally be influenced by nine detector and sample characteristics, outlined in Table 2.2. In order to solve for these nine unknowns, in principle nine observables must be recorded. However, the spatial variation and energy spectrum effects on detection efficiency can be accounted for with proper detector characterization. Spontaneous fission and $(\alpha, n)$ neutrons are assumed to have the same energy distribution, such that detection efficiency, fission probability, and neutron-induced fission multiplicity are the same for both types of sources. This is a vital simplifying assumption because plutonium samples often contain oxides that readily produce both fission and $(\alpha, n)$ neutrons. It is also assumed that the detection efficiency and the probability of fission are uniform over a sample volume, that all induced-fission neutrons are emitted simultaneous with the original spontaneous fission or $(\alpha, n)$ reaction, and that the neutron die-away time in the detector can be approximated by a single exponential time constant. Three unknowns remain: self-multiplication, $(\alpha, n)$ reaction rate, and spontaneous fission rate. These can be solved for with three observables: singles, doubles, and triples rates. All derivations in this section follow the assumptions outlined in Table 2.2 [27].

### Spontaneous fission and the $^{240}\mathrm{Pu}_{\mathrm{eff}}$ mass concept

Ideally, neutron counting would provide an unambiguous measure of fission source isotopics and mass. However, the relative neutron emission intensities of some isotopes over others, similar neutron multiplicity distributions, and complexity of analyses hinder a true isotopic unfolding of an assayed sample. For example, Table 2.1 demonstrates that the $^{240}$Pu neutron emission rate is five orders of magnitude greater than that of $^{239}$Pu, with identical average spontaneous fission multiplicities. Because of these physical constraints, differentiating isotopes of plutonium is currently an open problem.

A simplified model uses the $^{240}\mathrm{Pu}_{eff}$ concept, a proxy for plutonium mass defined as the mass of $^{240}$Pu that would give the same double coincidence response as obtained from a sample containing even isotopes of Pu ($^{238}$Pu, $^{240}$Pu, and $^{242}$Pu) [27], [26]:

$$^{240}Pu_{eff} = 2.52\ ^{238}Pu +^{240}\ Pu + 1.68\ ^{242}Pu$$

The constants 2.52, 1, and 1.68 are the ratios of the spontaneous fission decay rates of each isotope, with $^{240}$Pu the most prolific neutron emitter. Other methods such as gamma spectroscopy can be used to determine the isotopic distribution of Pu isotopes to give total plutonium content [27], [26]:

$$^{total}Pu =\ ^{240}Pu_{eff}/(2.52f_{238} + f_{240} + 1.68f_{242}),$$

Table 2.2: Unknowns associated with multiplicity counting and how to determine them.

| **Unknown** | **Remedy** |
|---|---|
| Spatial variation in neutron detection efficiency | Detector characterization |
| Energy spectrum effects on detection efficiency | Detector characterization |
| The energy spectrum of the ($\alpha$,n) neutrons | Assumption: ($\alpha$,n) neutrons and spontaneous fission neutrons have the same energy spectrum, such that detection energy-dependent efficiency, fission probability, and induced-fission multiplicity are the same for both neutron sources |
| Spatial variation of the neutron multiplication | Assumption: Neutrons are emitted uniformly over a sample volume and the detector efficiency for a given neutron is constant |
| Neutron capture in the sample | Assumption: All induced-fission neutrons are emitted simultaneously with the original spontaneous fission or ($\alpha$,n) reaction |
| The neutron die-away time in the detector | Assumption: Neutron die-away time in the sample/detector combination is well approximated by a single exponential time constant. |
| Sample multiplication | Solved for |
| The ($\alpha$,n) reaction rate in the sample | Solved for |
| **Spontaneous fission rate** | **Characteristic of interest, solved for** |

where $f_{238}$, $f_{240}$, and $f_{242}$ are the fractions of $^{238}$Pu, $^{240}$Pu, and $^{242}$Pu contained in the sample.

### ($\alpha$,n) reactions

Plutonium and uranium emit high-energy alphas that readily undergo ($\alpha$,n) reactions with oxides in the sample. Alpha decay dominates spontaneous fission by five orders of magnitude for $^{238}$U, and by six for $^{240}$Pu [29]. Furthermore, the relatively short range ($\sim$0.006 cm) of alphas in oxide leads to a high probability that an emited alpha will be stopped in the sample. The high energy of the alphas (4.19 MeV for $^{238}$U and 5.15 MeV for $^{240}$Pu) implies a high probability for the ($\alpha$,n) reaction in oxide. The $^{238}$U alpha yield is $1.2 \times 10^4$ $\alpha/(s \times g)$, and the ($\alpha$,n) yield in oxide is $8.3 \times 10^{-5}$ $n/(s \times g)$ [30]. $^{240}$Pu emits $8.4 \times 10^9$ $\alpha/(s \times g)$ and $1.41 \times 10^2$ $n/(s \times g)$ from the ($\alpha$,n) reaction, compared with $1.02 \times 10^3$ $n/(s \times g)$ from spontaneous fission [30]. Consequently, ($\alpha$,n) neutrons potentially constitute a major fraction of $^{240}$Pu neutrons, and therefore must be well understood for accurate sample assay [27], [26].

The parameter $\alpha$ is defined as the ratio of ($\alpha$,n) to spontaneous fission neutrons (including

$^{241}$Am ingrowth) [27], [26]:

$$\alpha = \frac{13400 f_{238} + 38.1 f_{240} + 141 f_{241} + 2.0 f_{242} + 2690 f_{Am241}}{1020(2.54 f_{238} + f_{240} + 1.69 f_{242})}, \tag{2.7}$$

where $f_{238}$, $f_{240}$, and $f_{242}$ are the fractions of $^{238}$Pu, $^{240}$Pu, and $^{242}$Pu contained in the sample.

For a pure metal sample with no oxides, $\alpha = 0$. Following an ($\alpha$,n) reaction on oxygen, the outgoing neutron is 2.03 MeV, which is close to the average spontaneous fission neutron energy of 1.96 MeV. This validates the first assumption in Table 2.2 to a first approximation. However, fission neutrons have a very high energy tail that can render the assumption invalid for detectors that are sensitive to high energy gammas.

### Sample multiplication

A sample neutron can increase the neutron population by induced fission or $(n, xn)$ reactions, or reduce the population by absorption through $(n, \gamma)$ or $(n, p)$ reactions or by leaking out of the sample without interaction. Sample multiplication seeks to characterize the neutron population in the sample as a function of time.

The multiplication factor $k$ is used to compare the number of neutrons in one generation with the number in the previous generation in an infinitely large sample. For example, $k < 1$ indicates that the sample is sub-critical and the neutron population will decrease exponentially over time, $k = 1$ that the sample is critical and the number of neutrons is constant, and $k > 1$ that the sample is supercritical and the neutron population will increase exponentially. The multiplication factor for a finite sample is termed $k_{eff}$ and follows the same definition as $k$ for a finite sample.

Similarly, the total multiplication $M_T$ tracks the current number of neutrons divided by the initial number. In this context, $k$ is the multiplication factor $p\nu_i$, where $\nu_i$ is the average number of neutrons created by induced fission and $p$ is the probability that a neutron will induce fission. So [26]

$$M_T = \frac{1}{1 - p\nu_i} = \frac{1}{1 - k}, \; k < 1$$

Parallel to $k_eff$, $M_L = M$ is the leakage multiplication and reflects the fact that some neutrons will leak from the sample; it is always less than $M_T$. The net leakage multiplication is then

$$M = \frac{1 - p}{1 - p\nu_i} \tag{2.8}$$

$M$ can be calculated with Monte Carlo codes or from observables using multiplicity counting [27], [26].

### Measured count rates

Historically, the Rossi-$\alpha$ (Fig. 2.7) distribution has been analyzed with shift registers to compute the rates of singles, doubles, and triples. A shift-register circuit would tally the

number of times that $N$ neutrons were counted in the R+A (real and accidental coincidences) and A (accidental coincidences) gates – for example, if five neutrons were counted in the R+A gate, then the count on the register that tallies fives would increase by one [27], [26].

The number of neutrons detected and counted in the gate interval following a trigger in the R+A gate is given as $f(i)$. The distribution of randomly triggered accidental A neutrons is denoted as the background, $b(i)$. Subscripts 1 and 2 denote the occurrence of singles and doubles. The singles rate $S$ is the total sum of all triggers, not just the number of singles tallies. The doubles rate is[27], [26]:

$$D = S(f_1 - b_1), \tag{2.9}$$

and the triples rate is:

$$T = S(f_2 - b_2 - 2b_1(f_1 - b_1))/2. \tag{2.10}$$

### Neutron multiplicity moments

*Neutron multiplicity moments* are related to the probability of detecting the coincidence of a certain number of neutrons, and are used in the final calculation to solve for the three unknowns. Appendix A shows the multiplicity distributions of several isotopes, and Equations 2.2 and 2.3 show that the distributions are both normalizable and have a singles average of $\nu_1$. Extending this argument, higher moments can be defined [26] as follows:

$$\nu_1 = \sum_{\nu=1}^{max} \nu P(\nu), \tag{2.11}$$

$$\nu_2 = \sum_{\nu=2}^{max} \nu(\nu-1) P(\nu), \tag{2.12}$$

$$\nu_3 = \sum_{\nu=3}^{max} \nu(\nu-1)(\nu-2) P(\nu), \tag{2.13}$$

where $P(\nu)$ is the probability of obtaining an event with multiplicity $\nu$, from Appendix A. The generalized expression for factorial moments is then this [26]:

$$\nu_k = \sum_{\nu=k}^{max} \frac{\nu!}{(\nu-k)!} P(\nu). \tag{2.14}$$

### Putting it all together

In order to solve for the relevant sample quantities, measured values must be related to the unknowns. The analytical definitions of singles, doubles, and triples that can be solved for the desired unknowns is as follows [27], [26]:

$$S = F\epsilon M \nu_{s1}(1+\alpha), \tag{2.15}$$

$$D = \frac{F\epsilon^2 f_d M^2}{2}\left[\nu_{s2} + \left(\frac{M-1}{\nu_{i1}-1}\right)\nu_{s1}(1+\alpha)\nu_{i2}\right], \tag{2.16}$$

$$T = \frac{F\epsilon^3 f_t M^3}{6}\left[\nu_{s3} + \left(\frac{M-1}{\nu_{i1}-1}\right)[3\nu_{s2}\nu_{i2} + \nu_{s1}(1+\alpha)\nu_{i3}] + 3\left(\frac{M-1}{\nu_{i1}-1}\right)^2 \nu_{s1}(1+\alpha)\nu_{i2}^2\right], \tag{2.17}$$

where

$F$ = spontaneous fission rate,
$\epsilon$ = neutron detection efficiency,
$M$ = neutron leakage multiplication,
$\alpha = (\alpha, n)$ to spontaneous fission neutron ratio,
$f_d$ = doubles gate fraction,
$f_t$ = triples gate fraction,
$\nu_{s1}$, $\nu_{s2}$, $\nu_{s3}$ = factorial moments of spontaneous fission neutron distribution, and
$\nu_{i1}$, $\nu_{i2}$, $\nu_{i3}$ = factorial moments of induced fission neutron distribution.

For a given gate width $G$, the doubles gate fraction $f_d$ is the fraction of counted detected doubles and is determined by [26]

$$f_d = e^{-P/\tau}(1 - e^{-G/\tau}) \tag{2.18}$$

where $\tau$ is the detector die-away time, $G$ the shift-register gate width, and $P$ the shift-register predelay. The triples gate fraction is $f_t = f_d^2$ and is generally determined experimentally [27], [26].

### Solving for mass, multiplication, and $\alpha$

Equations 2.9 and 2.10 relate measured quantities to the doubles and triples rate, while the singles rate is the sum of all triggers. Equations 2.15 through 2.17 give the analytical expressions that can be applied in conjunction with the measured singles, doubles, and triples rates to solve for $M$, $F$, $\alpha$, and $m_{240}$ to determine total plutonium mass. If the sample contains a small or diffuse quantity of plutonium, it might be safe to assume $M = 1$. If not, Equations 2.9 through 2.17 can be solved for $M$ [27], [26]:

$$a + bM + cM^2 + M^3 = 0$$

where the coefficients $a$, $b$, and $c$ are in terms of measured quantities $S$, $D$, $T$:

$$a = \frac{-6T\nu_{s2}(\nu_{i1}-1)}{\epsilon^2 f_t S(\nu_{s2}\nu_{i3} - \nu_{s3}\nu_{i2})},$$

$$b = \frac{2D[\nu_{s3}(\nu_{i1}-1) - 3\nu_{s2}\nu_{i2}]}{\epsilon f_d S(\nu_{s2}\nu_{i3} - \nu_{s3}\nu_{i2})},$$

and

$$c = \frac{6D\nu_{s2}\nu_{i2}}{\epsilon f_d S(\nu_{s2}\nu_{i3} - \nu_{s3}\nu_{i2})}.$$

After $M$ is calculated, the sample fission rate is given by

$$F = \frac{\left(\frac{2D}{\epsilon f_d} - \frac{M(M-1)\nu_{i2}S}{\nu_{i1}-1}\right)}{\epsilon M^2 \nu_{s2}}.$$

The sample's $\alpha$ value is then

$$\alpha = \frac{S}{F\epsilon\nu_{s1}M} - 1.$$

Finally,

$$m_{240} = \frac{F}{473.5 fissions/s \times g}$$

If the fractions $f_{238}$, $f_{240}$, and $f_{242}$ are known (either assumed or measured with gamma spectroscopy), then the total mass of plutonium is [27], [26]:

$$Pu = \frac{m_{240}}{2.52 f_{238} + f_{240} + 1.68 f_{242}}$$

### 2.3.4 Beyond singles, doubles, and triples

Time-correlated neutron detection techniques that track high-order multiplicity events can be utilized in arms control, threat detection, and nuclear material assay. In particular, Kakae et al. used fast, low-efficiency detectors to identify fissioning material based on high-order neutron multiplicity. Fig. 2.8 shows a comparison between random sources of counts and a correlated highly multiplying plutonium ball. Each cycle represents a measurement window of 0.512 ms. After only 52 s, there is a clear distinction between the correlated and uncorrelated sources [31].

By measuring high-order multiplicities and comparing them with a random source, it is potentially possible to differentiate between different spontaneous fission sources [31]. However, liquid scintillator detectors are sensitive only to high-energy neutrons, and thus might be blind to a shielded neutron source.

## 2.4 Conventional slow neutron detectors

Neutron detection is typically classified as "fast" or "slow." Fast neutron detection relies on elastic collisions between neutrons and hydrogen nuclei of scintillating material, creating energetic secondary particles and therefore scintillation light. Slow neutron detection, the focus of this dissertation, relies instead on a conversion material with a high neutron absorption cross section that undergoes a reaction to create detectable products.

Such materials are both readily available and inexpensive [32]. Potential candidate isotopes include $^{10}$B, $^{6}$Li, $^{3}$He, and $^{157}$Gd, for which Fig. 2.9 shows the total neutron absorption cross section. Note that the thermal neutron absorption cross section of $^{157}$Gd is approximately two orders of magnitude greater than that of the other plotted isotopes. In fact,

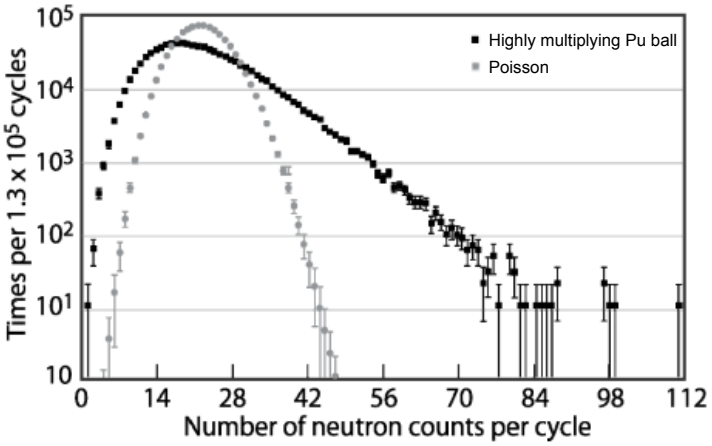


Figure 2.8: Multiplicity data comparing an expected Poisson distribution with a highly multiplying plutonium ball. Adapted from [31].

$^{157}$Gd's 255,000 barn thermal neutron absorption cross section is the highest of any stable isotope, second only to the two-million barn cross section of radioactive $^{135}$Xe [32].

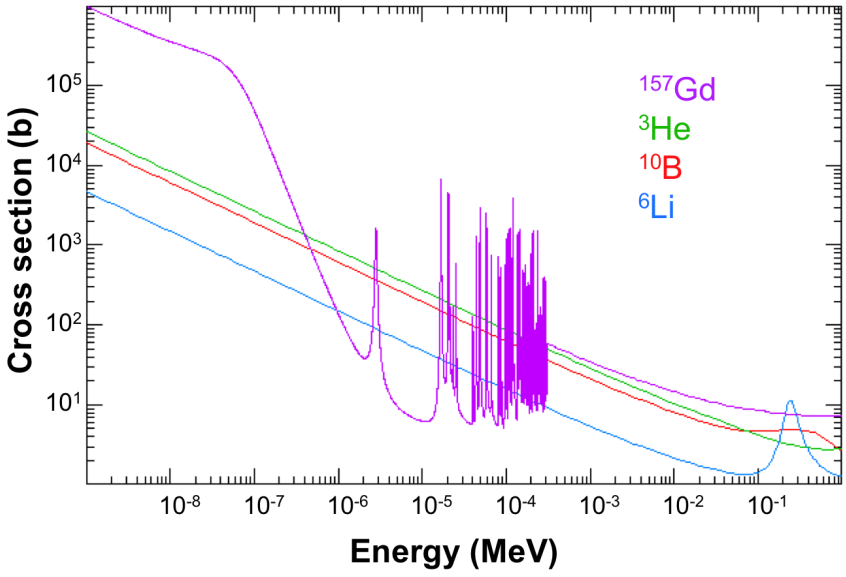


Figure 2.9: Total neutron absorption cross section for $^{10}$B, $^{6}$Li, $^{3}$He, and $^{157}$Gd [33].

### 2.4.1 $^3$He-based detectors

Because the IAEA relies heavily on $^3$He for neutron detection, this section focuses on an analysis of $^3$He as the current detection gold standard. $^3$He undergoes the following neutron absorption reaction:

$$ {}^3_2He + {}^1_0n \rightarrow {}^3_1H + {}^1_1p + 0.764MeV $$

where the 0.764 MeV Q-value is shared between the proton and $^3$H kinetic energies ($E_p$=0.573 MeV and $E_{^3H}$=0.191 MeV). The thermal neutron absorption cross section is 5330 barns and follows a $1/v$ energy dependence, as shown in Fig. 2.9. Because $^3$He is a noble gas, no solid compounds exist and typical detectors use $^3$He as the medium in a Geiger mode proportional counter. The neutron detection efficiency of a neutron impinging on the detection volume of a $^3$He-based counter is as follows:

$$ \epsilon(E) = 1 - exp(-\Sigma_a(E)L), $$

where $\Sigma_a(E)$ is the macroscopic neutron absorption cross section of $^3$He at energy $E$ ($\Sigma = N\sigma$, $N$ is the atomic density in $atoms/cm^3$, and $\sigma$ is the microscopic cross section in $cm^2$) and $L$ is the detector thickness perpendicular to the incident neutron direction. Because the neutron absorption cross section is maximized at low energies (see Fig. 2.9), $^3$He-based neutron detectors are typically set in a hydrogenous material to thermalize neutrons prior to their impingement on the detector volume. Fig. 2.10 shows a schematic of three potential neutron histories in a heterogeneous detector volume where the detection medium is separate from the moderator – the neutron can escape the moderator, or be moderated and absorbed into either the moderator or the detector volume [32]. Only the latter history creates a detector signal, and care must be taken to optimize the moderator to detector volumes and geometries. However, nondetection due to escape or moderator capture is always a possibility, and homogeneous detector designs can improve on this.

Some specialized detectors are designed for extremely high-fidelity neutron multiplicity counting with maximized efficiency ($\epsilon$) and minimized deadtime ($\tau$). A convenient measure of the effectiveness of a neutron multiplicity counter is the Figure of Merit (FOM), emphasizing the efficiency and die-away time. An example is the Plutonium Scrap Multiplicity Counter (PSMC) used to verify 1 to 5000 g canned plutonium-containing samples, for which the PSMC FOM is as follows:

$$ FOM = \frac{\epsilon}{\sqrt{\tau}} = \frac{55\%}{47\ \mu s} \approx 8, \tag{2.19} $$

where $\epsilon$ is the single neutron detection efficiency as a percentage, and $\tau$ is the thermal neutron capture time in $\mu s$.

### 2.4.2 Merits of $^3$He-based detectors

In general, $^3$He exhibits favorable neutron detection characteristics because it has a high neutron absorption cross section and the reaction products are heavy charged particles

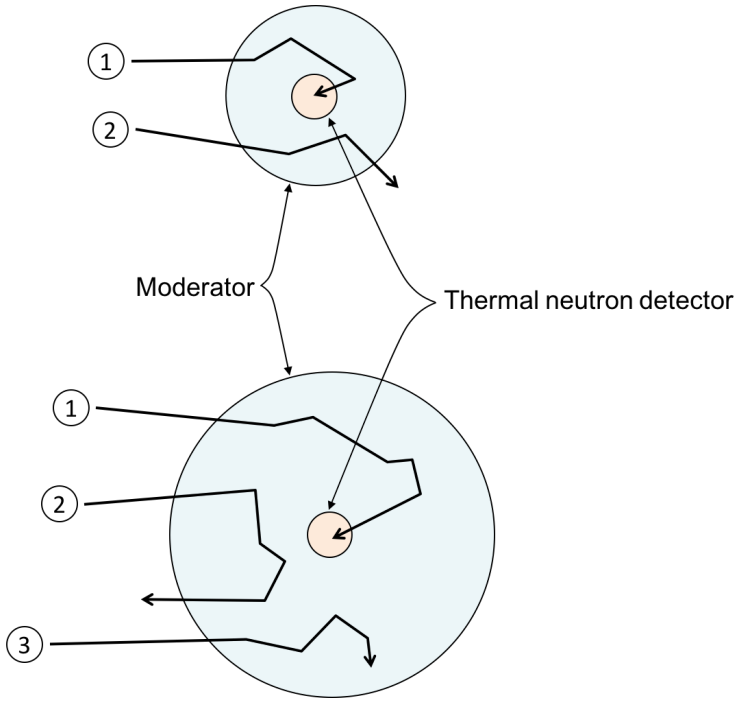


Figure 2.10: Schematic demonstrating a heterogeneous neutron detector. Neutron tracks labeled (1) illustrate fast neutrons that are successfully moderated and detected. Tracks labeled (2) are partially or fully moderated, but escape without detection. Tracks labeled (3) show neutrons that are absorbed into the moderating material. Adapted from [32].

that deposit a large amount of energy per unit path length in the detector, allowing for gamma/neutron discrimination. Additional favorable characteristics include the following [8]:

- High efficiency,
- Low gamma interference (no performance degradation below a flux of 100 R/hr),
- High maximum neutron count rate (above 100 counts/sec-cm$^2$),
- Uniform spatial and energy response,
- Practical considerations: long-term stability, non-hazardous, safe, low maintenance requirements, low power requirements (less than 5 kV), small footprint, low mass, reliable, non-cryogenic,
- Mass production characteristics: commercial availability, availability of production quantities, robustness, historically low price, mature technology, temperature stability

Because of these characteristics, $^3$He-based neutron detectors have come to dominate IAEA safeguards.

## 2.5 Possible alternatives to $^3$He-based neutron counters

Detectors not based on $^3$He are nonetheless an active field of research in academia, national laboratories, and industry because of the $^3$He shortage. A number of alternate detection methods are under development, while some detectors (such as $BF_3$) are mature technologies that are re-emerging. Others are being developed for specific niche applications, such as organic liquid scintillators. Although no alternate detector demonstrates all of the beneficial aspects of $^3$He-based systems, certain detectors are an improvement in some aspects – for example, scintillators that can provide energy information and have low decay times. This section outlines some of the potential alternates that were directly identified by the IAEA Workshop: $^{10}$B and $^6$Li-based systems, as well as liquid and plastic scintillators.

### 2.5.1 $^{10}$B-based systems

$^{10}$B is an attractive neutron detection medium because it offers a neutron absorption cross section comparable with $^3$He (see Fig. 2.9), it is a mature technology, and it is potentially a drop-in replacement for existing $^3$He-based detectors. Upon neutron capture, the $(n, \alpha)$ reaction leaves ${}^7_3Li$ in a ground or excited state [32]:

$$ {}^{10}_{5}B + {}^{1}_{0}n \rightarrow {}^{7}_{3}Li + {}^{4}_{2}\alpha + 2.792\ MeV\ (ground\ state;\ 6\%\ branching\ ratio) $$

$$ {}^{10}_{5}B + {}^{1}_{0}n \rightarrow {}^{7}_{3}Li^{*} + {}^{4}_{2}\alpha + 2.310\ MeV\ (excited\ state;\ 94\%\ brancing\ ratio) $$

At thermal energies (0.025 eV), the $^{10}$B neutron absorption cross section is 3,840 barns, 72% of the $^3$He cross section of 5330 barns [32].

The most common implementation of boron in neutron detection is $BF_3$-based proportional counters that provide good gamma/neutron discrimination properties and high count rate capabilities [34]. However, the IAEA has precluded the use of $BF_3$ gas due to its corrosive and toxic nature [8] and the dangers this poses in sensitive nuclear facilities. That said, it should be noted that there have been no known leaks in the 250,000 non-pressurized and hermetically sealed $BF_3$ detectors during either transportation or use over the past seventy years [35].

Boron-lined tubes offer an alternative to toxic $BF_3$ gas, and consist of a solid boron coating on the interior wall of a proportional tube. Following $^{10}$B$(n, \alpha)^7$Li reaction in the solid boron region, the 1.47 MeV $\alpha$ and 0.84 MeV $^7$Li have a range of $\sim$4 $\mu$m in solid boron. If the $\alpha$ or $^7$Li is created on the surface of the solid region and emitted directly into the proportional gas, it will deposit its full energy. If it does not escape the solid region, then no energy will be recorded. Consequently, a continuum of energy is deposited from zero to the maximum 1.47 MeV $\alpha$ energy. However, because there is no clear divide between gamma and neutron energy deposition, gamma discrimination is more complicated and boron-lined tubes are about seven times less efficient than $^3$He [32]. While these boron tubes technically

do offer drop-in replacement for $^3$He tubes, the decrease in efficiency necessitates either tolerating longer dwell times or increasing the number of tubes in a detector, which has a diminishing effect as the volume of moderator decreases (see Fig. 2.10) [34]. Some high-surface-area detectors have been developed for example, through the use of multiple straw cathodes in a larger tube volume – but this configuration suffers from self-shielding effects, and the increased complexity leads to an increase in price [34].

### 2.5.2 $^6$Li-based systems

Much like $^{10}$B, $^6$Li$(n, \alpha)$ undergoes the following reaction with a 940 barn thermal cross section [32]:

$$^6_3Li + ^1_0 n \rightarrow \ ^3_1H + ^4_2 \alpha + 4.78MeV.$$

The diminished $^6$Li cross section is partially offset by the higher Q value. Because it has a high Q value and a lithium-containing proportion gas does not exist [32], $^6$Li is generally incorporated into lithium-containing scintillators.

Lithium iodide crystals have a typical decay time of approximately 0.3 $\mu$s, and poor gamma/neutron discrimination because a single gamma interaction can produce a pulse height approximately proportional to its energy – roughly equal the energy of neutron-induced reaction products. Furthermore, lithium iodide is highly hydroscopic and must be sealed against water vapor. Scintillators based on small ($\sim$0.6 mm) lithium compounds dispersed in a matrix of ZnS(Ag) are commercially available, and boast 25-30% neutron detection efficiency for 0.1 eV neutrons [32].

Lithium glass scintillators can be loaded with up to 7.7% lithium and offer a fast response compared with gaseous detectors, $\sim$70-100 ns. However, they exhibit nonlinear light output with respect to incident particle energy, and light output is also diminished for heavy charged particles compared with gammas, resulting in poor gamma/neutron discrimination [32].

### 2.5.3 Scintillators

Unlike the previously described neutron detection methods, which use an absorption reaction, scintillators instead can utilize the recoiling nucleus from an elastic collision for neutron detection. An incident fast neutron can elastically scatter and dislodge a target nucleus (such as a hydrogen nucleus), creating a secondary heavy charged particle with a highly concentrated energy deposition that then excites molecules in the scintillator. The excited molecules will de-excite by fast or slow processes depending on the density of energy deposition. While neutrons create secondary particles with high energy deposition, gamma energy deposition tends to be less concentrated, leading to different de-excitation time scales for gammas and neutrons. Pulse-shape discrimination can then distinguish between gammas and neutrons [32]. Scintillators can be found in organic, inorganic, crystalline, plastic, and liquid forms.

Liquid organic scintillators have historically been precluded from use in IAEA applications because of their low flash point, toxicity, and relatively complex data acquisition and

offline analysis. However, the recent development of high flash point and non-hazardous compounds, as well as advances in data processing, have made them more attractive. Two key benefits of liquid scintillators are that the response time is less than 100 ns (compared with tens of microseconds for typical thermal detectors) and that they exhibit relatively high efficiency (tens of percent for typical systems). This makes liquid scintillators especially attractive for neutron-coincidence counting applications. However, key outstanding technical issues include gamma rejection, neutron/gamma coincidence effects, and thermal stability [8].

Plastic scintillators are a new and advancing technology. R&D programs generally focus on concerns regarding pulse-shape discrimination, production, material uniformity and quality, and environment, temperature, and long-term stability effects [8].

## 2.6 Detector need

Though many exciting detector developments have been made because of the $^{3}$He shortage, no new design is yet a like-for-like replacement [8]. High-fidelity non-$^{3}$He based detectors are necessary in order to maintain high caliber IAEA nuclear safeguard verification. Within the realm of non-$^{3}$He-based neutron detectors, systems are needed that excel at high-order neutron multiplicity measurements – that is, detectors with high efficiency and low deadtime. Ideally, such systems would also prove tolerant against gammas for general neutron multiplicity measurement, and be practical in extreme situations such as the direct measurement of plutonium in spent fuel. The remainder of this dissertation focuses on one such potential alternative: the Water Neutron Detector (WaND).

# Chapter 3

# The Water Neutron Detector

## 3.1 Standing on the shoulders of giants

The Water Neutron Detector (WaND) is a water Cherenkov based detector that builds on the detection principles utilized for large-scale neutrino and antineutrino detectors. This chapter outlines the most influential neutrino and antineutrino detectors and describes the WaND system – the detector itself, signal generation, and critical parameters – then concludes with a canonical detector response spectrum.

Water-Cherenkov neutrino and antineutrino detectors have several attributes in common: size, detection medium, detection principle, and shielding. Because neutrino interaction cross-sections are so small (on the order of $10^{-47}\mathrm{m}^2$), their mean free path is extremely long (roughly a light year for lead). Consequently, detectors must either be close to an intense source (such as a nuclear reactor, an enormous source of antineutrinos), or be enormous. Most detectors are very large (many kilotons), making water a practical detection medium. Large antineutrino water detectors rely on inverse beta decay,

$$\bar{\nu_e} + p \rightarrow n + e^+,$$

where the positron and neutron reaction products can be used to identify the antineutrino event. If the detector is loaded with a neutron capture agent (like gadolinium), the time signature of positron and neutron capture can be used to identify the inverse beta decay interaction. Because neutrino and antineutrino interactions are so rare, massive shielding is required to reduce background radiation, typically achieved by situating the detector deep underground [36].

Table 3.1 outlines major water Cherenkov neutrino and antineutrino detectors: Irvine-Michigan-Brookhaven (IMB) [37], Sudbury Neutrino Observatory (SNO) [38], Super-Kamiokande [39], [40], and WATer CHerenkov Monitoring of Anti-Neutrinos (WATCHMAN) [41]. The IMB was the first of its kind, and paved the way for future detectors. Director of the SNO experiment Art McDonald was awarded the 2015 Nobel Prize in Physics for the detector's contribution to the discovery of the non-zero mass of the neutrino [38]. Super-Kamiokande

Table 3.1: Water-Cherenkov neutrino and antineutrino detectors

| **detector** | **active dates** | **detection medium** | **weight (kt)** | **shielding (km underground)** |
|---|---|---|---|---|
| IMB | 1979-1991 | water | 8 | 0.6 |
| SNO | 1999-2006 | heavy water | 1 | 2 |
| Super-Kamiokande | 1996-current | water | 50 | 1 |
| WATCHMAN | proposed | Gd-doped water | 3.540 | |

is the world's largest water Cherenkov detector, following a long line of upgraded detectors including Kamiokande and Kamiokande-II, and which will ultimately be upgraded by adding gadolinium. Over 11,000 photo multiplier tubes (PMTs) are used in Super-Kamiokande to search for Cherenkov signals resulting from solar, atmospheric, supernova, gamma ray burst, and artificial neutrino sources; Masatoshi Koshiba was awarded the 2002 Nobel Prize in Physics partially for the detection of cosmic neutrinos [39], [40]. The proposed WATCHMAN detector would employ gadolinium-doped water for a six-fold increase in detection efficiency by using the temporal signature of positron annihilation followed by neutron capture [41].

The WaND system employs a detection technique for neutron counting similar to that of these large-scale neutrino and antineutrino detectors. The WaND system is in most respects a scaled-down WATCHMAN: while WATCHMAN utilizes the inverse beta decay neutron and positron-electron product signals, the WaND system counts neutrons directly via neutron capture on gadolinium. The detector is smaller in mass because neutrons have a much shorter path length in water than neutrinos or antineutrinos.

## 3.2 The physical detector

The WaND system, as shown in Fig. 3.1, is composed of 1.03 $m^3$ of 18 M$\Omega$ deionized water doped with 0.5% gadolinium-chloride ($GdCl_3$) in a stainless steel tank (121.9 cm $\times$ 91.4 cm $\times$ 119.4 cm). The inside of the tank is coated with baked-on Teflon to protect the stainless steel from corrosion that can lead to a degradation of water quality [42]. The inner detector volume is also coated with a 1.0 mm reflective layer of GORE ® DRP ®, a Teflon-based highly reflective material (>99% in blue and near UV). Looking down into the water are eight Hamamatsu R7081 waterproof 10-inch PMTs mounted onto a scaffolding that maintains PMT-water contact and PMT neutral buoyancy. All PMT supports are constructed out of clear acrylic or reflective white polypropylene, relatively inert polymers that interact minimally with deionized water. Extending 45 cm into the water volume is a 19 cm wide cylindrical sample cavity [43]. The gadolinium-doped water Cherenkov neutron detection system is filed under patent US8373133 B2 [44].

Signals from each of the eight PMTs are amplified with a CAEN V975 fast amplifier and then split between a CAEN V814 discriminator and a Struck SIS3320 waveform digitizer. The trigger is generated by a threefold discriminator signal coincidence in a CAEN V1495

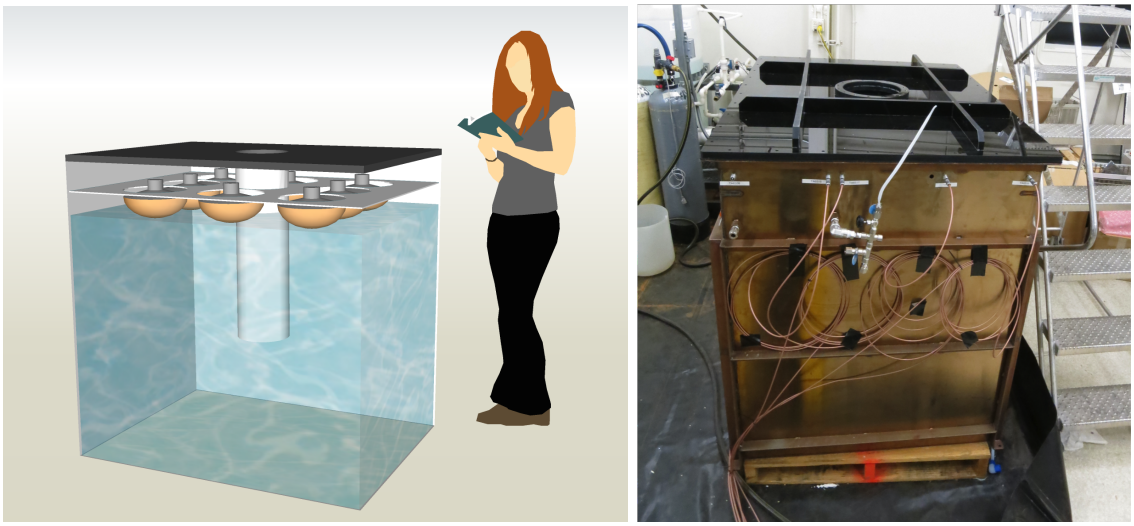

Figure 3.1: (left) A Sketchup rendering of the WaND system. Gadolinium-doped water (blue) comes partway up the stainless steel tank to meet the face of eight PMTs (orange) that surround a central sample well. (right) A photo of the assembled detector. The outside of the stainless steel container is visible (orange), as well as the light-tight lid with central sample well (black).

FPGA. After a trigger, the waveform digitizer can either record a microsecond-long pulse at a 5 ns sampling interval or digitize a set of independently integrated waveform sections for each PMT.

## 3.3 Detection principle

The WaND detection mechanism is similar to the water Cherenkov detectors outlined in Table 3.1. However, the WaND system counts neutrons directly, not as a product of inverse beta decay. Following a fission event, a high-energy neutron enters the water volume and downscatters until it reaches thermal equilibrium with the water. The neutron is then captured by a gadolinium nucleus, which enters an 8 MeV excited state and de-excites by emitting a gamma shower. The gammas Compton scatter and eject electrons with an energy high enough to emit Cherenkov radiation, which the PMTs detect.

### 3.3.1 Neutron moderation

At the instant of fission, approximately two to four neutrons with energies ∼1-2 MeV neutrons are emitted. A high-energy neutron traveling through matter (such as the detector water volume) can undergo either elastic or inelastic scatting, or absorption reactions with the hydrogen, oxygen, gadolinium, or chlorine nuclei. The total macroscopic cross-section

$\Sigma$ describes the likelihood of various interactions and is defined as the probability per unit path length traveled that the neutron will undergo a reaction with a sample nucleus:

$$\Sigma = \sigma \rho_A,$$

where $\sigma$ is the microscopic cross section and $\rho_A$ is the atomic density. Appendix C shows the relevant microscopic cross sections, $\sigma$. Gadolinium and hydrogen are of particular interest because gadolinium exhibits an exceptionally high neutron absorption cross section and hydrogen is the most abundant element in the detection volume.

Fig. 3.2 shows the macroscopic cross section for hydrogen and $^{157}$Gd. Hydrogen scattering interactions dominate at high energies down to approximately $10^{-8}$ MeV, at which point the gadolinium macroscopic cross section begins to dominate. In general, a neutron will fully thermalize before it captures on a gadolinium nucleus. At thermal energies, hydrogen scattering and $^{157}$Gd absorption compete.

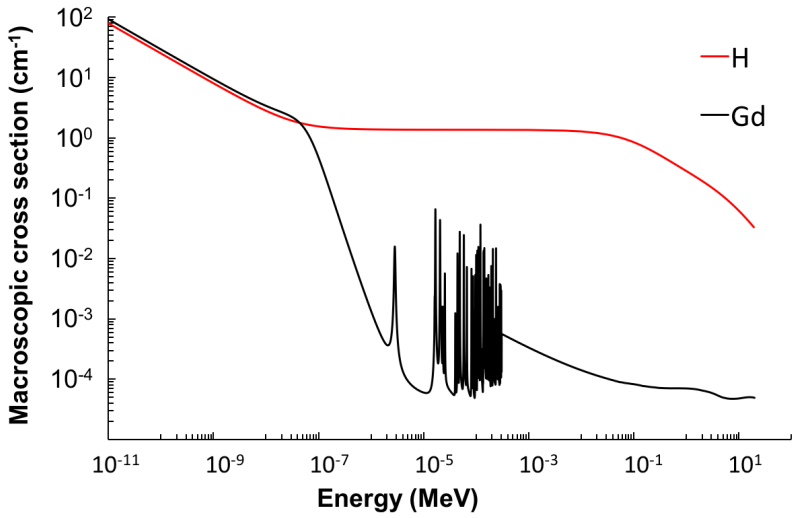


Figure 3.2: Macroscopic cross section of H and $^{157}$Gd, assuming 0.25% gadolinium. Data adapted from [33].

A 2 MeV neutron that enters the water volume will collide with nuclei until it reaches thermal equilibrium with the water (0.025 eV). The average energy loss per collision is

$$\overline{E - E'} = \frac{2EA}{(A+1)^2},$$

where $E$ is the neutron energy before the collision, $E'$ is the energy after, and $A$ is the atomic mass of the target nucleus. The maximum average energy loss of $\overline{E - E'}_{max} = E/2$

Table 3.2: Number of elastic collisions to thermalize

| Element | Atomic mass | Number of collisions (2 MeV → 0.025 eV) |
|---|---|---|
| H | 1 | 26 |
| O | 16 | 155 |
| Cl | 35 | 328 |
| Gd | 157 | 1438 |

is achieved when $A = 1$; hydrogen is therefore the most effective thermalization medium. The average number of collisions for a neutron to go from initial energy $E_0$ to final energy $E_n$ is

$$n = \frac{-log_{10}(E_n/E_0)}{log_{10}[(A^2+1)/(A+1)^2]}. \tag{3.1}$$

Using Eq. 3.1, the number of elastic collisions for a 2 MeV neutron to thermalize with the elements that constitute the detector volume in a homogeneous mixture is given in Table 3.2. Because of hydrogen's abundance and low number of requisite collisions, an energetic neutron will thermalize primarily via collisions with hydrogen.

Fig. 3.3 shows a Geant4 simulation (described in Section 3.4) of the depth at which neutrons capture on gadolinium in an environment similar to a simplified WaND. In the simulation, 1 MeV neutrons are shot into a 250 mm × 250 mm × 1 m cell containing water doped with 0.4% $GdCl_3$. The density plot demonstrates that most neutron captures occur approximately 35 mm into the water volume. Extrapolating to the detector itself, it is very likely that a high-energy neutron impinging on the detector volume from the sample well will thermalize within the water.

### 3.3.2 Gadolinium capture and gamma cascade

Neutron capture on heavy nuclei produce highly excited states just above the neutron separation energy, and de-excite via a gamma shower. This shower consists of a high-energy primary cascade, followed by a secondary component consisting of low-energy transitions from low-lying excited states to ground. No strong selection rules dictate the primary cascade [23].

$^{155}$Gd and $^{157}$Gd are the primary capture agents because of their relatively high isotopic content in natural gadolinium (Table B.1) and dominant cross section (Fig. C.4). Following neutron capture, gadolinium enters an excited state and de-excites by emitting ∼3-4 gammas in a cascade with a sum total energy of 8 MeV [45]. Fig. 3.4 shows the emitted gammas following thermal neutron capture of natural gadolinium. Note the cluster of primary high-energy (∼5-8 MeV), and secondary low-energy (∼0-1.5 MeV) gammas.

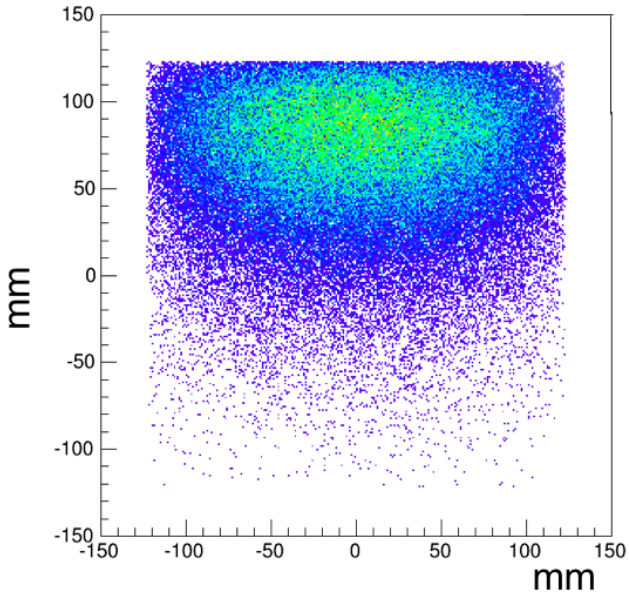


Figure 3.3: A Geant4 simulation of the capture of 1 MeV neutrons impinging on a 250 mm × 250 mm × 1 m cell filled with 0.4% $GdCl_3$ doped water in the negative vertical direction on the top horizontal edge. The X and Y axes display millimeters centered at the middle of the water cell. The density plot shows the relative number of neutrons captured at each $(x, y)$ coordinate. The white region surrounding the density plot is empty of matter.

### 3.3.3 Compton scattering

Gammas produced in the gadolinium cascade will attenuate in the water volume as

$$\frac{I}{I_0} = e^{-\mu x}, \tag{3.2}$$

where $I_0$ is the incident gamma intensity and $I$ is the gamma intensity at a distance $x$ in the absorbing medium [32]. The linear attenuation coefficient $\mu$ consists of the photoelectric, Compton scattering, and pair-production coefficients [32]:

$$\mu = \mu_{ph} + \mu_{cs} + \mu_p. \tag{3.3}$$

The mean free path – the average distance traveled in the absorber before an interaction takes place – is [32]

$$\lambda = \frac{\int_0^\infty x e^{-\mu x}}{\int_0^\infty e^{-\mu x}} = \frac{1}{\mu}.$$

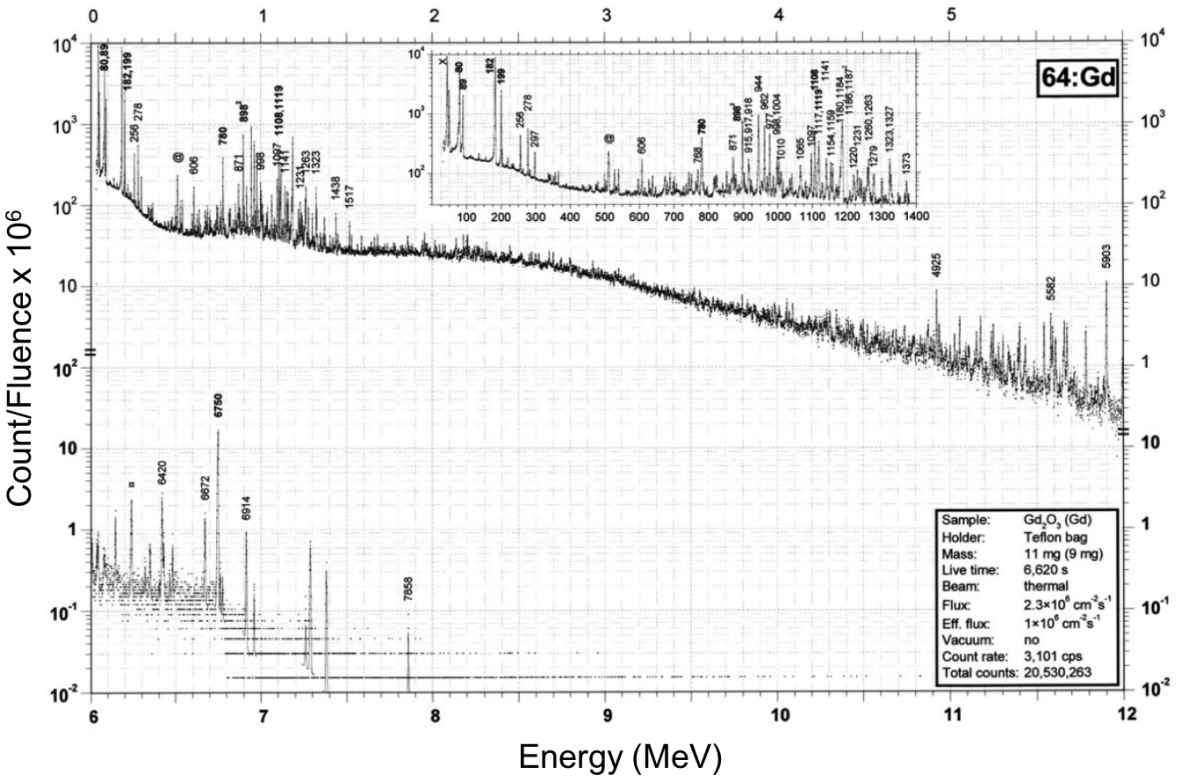


Figure 3.4: Gamma cascade following gadolinium neutron capture [46]. Note that the top axis corresponds to the top spectrum and the bottom axis to the bottom spectrum.

Fig. 3.5 shows mass attenuation ($\mu$) and absorption ($\mu_a$) coefficients for water, categorized by photoelectric, Compton, and pair-production interactions. Because 1-1.5 MeV gammas dominate the gadolinium cascade (Fig. 3.4), Compton scattering dominates gamma interactions in the detector.

Following a scattering event, the outgoing gamma will have an energy of

$$E_\gamma^{'} = \frac{E_\gamma}{1 + \frac{E_\gamma}{m_0 c^2}(1 - cos\theta)},$$

where $E_\gamma$ is the energy of the incident gamma, $\theta$ is the angle of the outgoing gamma, and $m_0 c^2 = 0.511$ MeV is the rest mass energy of the electron [32]. The scattered electron will have a kinetic energy equal to the difference in incoming and outgoing gamma energy:

$$T_e = E_\gamma - E_\gamma^{'} = E_\gamma \left(1 - \frac{1}{1 + \frac{E_\gamma}{m_0 c^2}(1 - cos\theta)}\right).$$

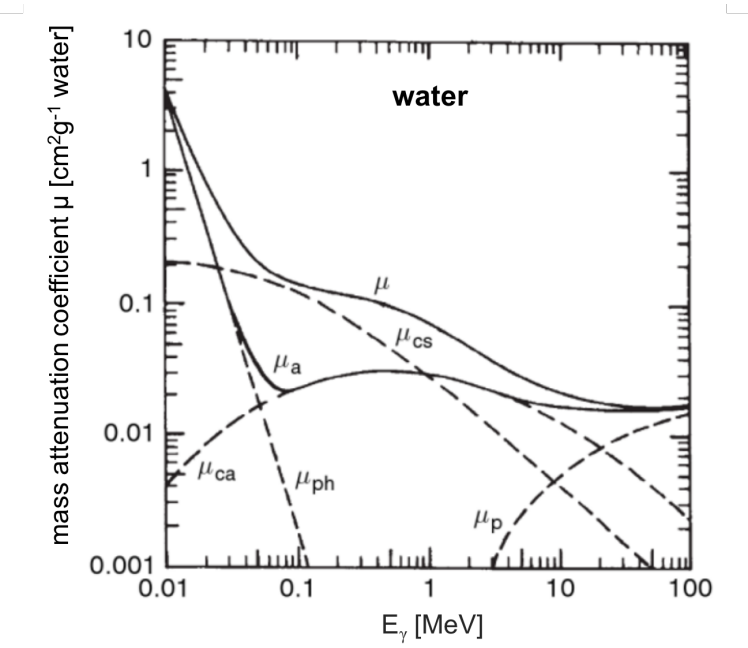


Figure 3.5: Mass attenuation ($\mu$) and absorption ($\mu_a$) coefficient as a function of energy in water. $\mu_{ph}$ describes the photoelectric effect, $\mu_{cs}$ describes Compton scattering, $\mu_{ca}$ describes Compton absorption, and $\mu_p$ describes pair production. $\mu_a$ is the total mass absorption coefficient ($\mu_a = \mu_{ph} + \mu_{ca} + \mu_p$), and $\mu$ is the total mass attenuation coefficient ($\mu_a = \mu_{ph} + \mu_{ca} + \mu_{cs} + \mu_p$) [47]

Maximum energy is transferred to the electron in a head-on collision when $\theta = \pi$:

$$T_e = E_\gamma \left(1 - \frac{1}{1 + \frac{2E_\gamma}{m_0 c^2}}\right).$$

Higher energy gammas transfer more energy to the electron – above approximately $E_\gamma = 2$ MeV, over 90% of the incident gamma energy is transferred to the electron.

To maximize the efficiency of the WaND, its size should be sufficient to thermalize and capture most of the neutrons, and the Compton scatter resulting gammas. From Fig. 3.3, approximately 5 cm is sufficient to capture nearly all neutrons, while 95% of ∼1 MeV gammas will Compton scatter within ∼30 cm. Added in quadrature, the water column should therefore have a minimum thickness of ∼30 cm from the well to the outer wall of the detector.

### 3.3.4 Cherenkov production and detection

Following a Compton scatter event, the ejected high-energy electron can emit Cherenkov radiation. Cherenkov radiation was first theorized in 1888 by Oliver Heaviside, and discovered by Pavel A. Cherenkov in 1936. The Cherenkov effect involves the production of visible

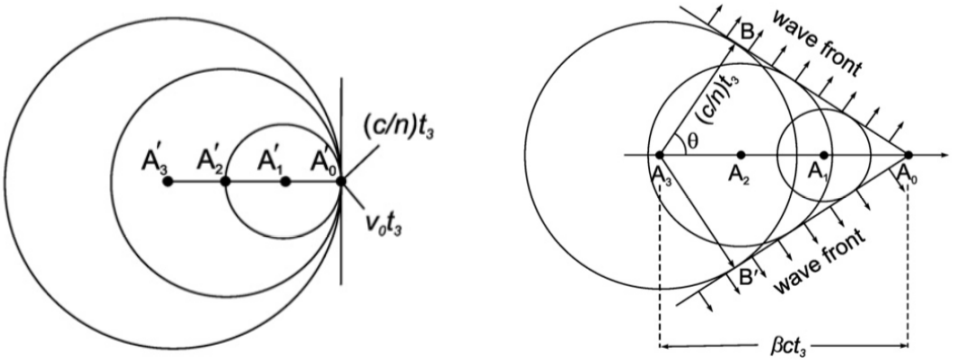


Figure 3.6: A Huygens interpretation of the Cherenkov effect, where a charged particle moves at the same speed as light travels through the medium $\beta n = 1$ (left) and faster than the speed at which light travels through the medium $\beta n > 1$ (right). Adapted from [28].

photons when a charged particle travels through a transparent medium at a speed greater than the speed at which light travels through the medium [28].

As a charged particle traverses a dielectric medium, it creates local polarization. If the particle is traveling slowly compared with the speed at which light travels through the medium, then the local dielectric polarization will relax back to equilibrium as the particle moves; however, if the particle is traveling faster than the relaxation time of the medium, energy radiates as a coherent shock wave.

Fig. 3.6 shows a diagram based on Huygens's Principle to demonstrate the Cherenkov effect. A charged particle travels from position $A_3$ at time $t_3$ to position $A_2$ at time $t_2$ to position $A_1$ at time $t_1$, and an observation is made at position $A_0$ and time $t_0$. The spherical dielectric perturbations travel outward from the particle at a phase velocity of $c/n$, where $c$ is the speed of light in a vacuum and $n$ is the index of refraction of the medium. The radius of each sphere is $(c/n)t_{1,2,3}$ for the spheres centered around $A_{1,2,3}$ and 0 for position $A_0$. According to Huygens's Principle, the wave fronts are defined by the radius vector drawn from the center of the sphere to the tangent of the sphere and the envelope. If the particle is moving more slowly than the wave propagation, each sphere will be contained within the previous sphere. If the particle is moving at the speed of light in the medium, the wave front spheres are contained within each other, but have a single point of tangency ($A'_0$ in Fig. 3.6 left) and create a plane wave perpendicular to the direction of motion. If the particle is moving faster than the waves can propagate, it will out-pace previous wave fronts. Fig. 3.6 right shows an example where the particle is traveling faster than the perturbation phase velocity, creating a conical wave front with an apex at $A_0$.

As implied in Fig. 3.6, Cherenkov radiation is produced only when a charged particle moves faster than the speed at which light travels through the medium. Therefore, the Cherenkov threshold condition is

$$\beta > 1/n, \tag{3.4}$$

where $\beta = v/c$, $v$ is the particle velocity, $c = 2.99 \times 10^{10}$ cm/s is the speed of light, and $n$ is the medium index of refraction. The energy of a relativistic particle is

$$E = m_0 c^2 \left[ \frac{1}{(1-\beta^2)^{1/2}} - 1 \right] \tag{3.5}$$

where $m_0$ is the particle rest mass ($m_0 = 511$ keV for electrons) and $E$ is the kinetic energy. Applying the threshold condition Eq. 3.4 to Eq. 3.5 gives the minimum-energy Cherenkov threshold:

$$E_{min} = m_0 c^2 \left[ \left( 1 - \frac{1}{n^2} \right)^{-1/2} - 1 \right]. \tag{3.6}$$

Thus, the Cherenkov threshold energy of a particle depends only on the index of refraction of the medium and its mass. For example, the kinetic energy threshold for an electron traveling through water ($n = 1.333$) is 262 keV.

From Fig. 3.6, the angle of the Cherenkov cone $\theta$ is

$$cos\ \theta = \frac{A_3 B}{A_3 A_0} = \frac{(c/n)t_3}{\beta c t_3} = \frac{1}{\beta n}.$$

The final step in the signal generation process is the detection of Cherenkov light by PMTs. The number of photons emitted for a short length of the electron track (assuming a constant $\beta$ and $n$) is [48]

$$\frac{dN}{dx} = 2\pi\alpha \left( 1 - \frac{1}{\beta^2 n^2} \right) \int_{\lambda_1}^{\lambda_2} \frac{1}{\lambda^2} d\lambda, \tag{3.7}$$

where $\alpha \sim 1/137$ is the fine structure constant. Fig. 3.7 additionally shows the correlation between emitted Cherenkov photons and PMT quantum efficiency. The number of Cherenkov photons is calculated in 10 nm bin widths from a discretized form of Eq. 3.7. Note that most Cherenkov photons are emitted in the ultraviolet portion of the spectrum. Although there is not a perfect match between Cherenkov photon emission and PMT quantum efficiency, the highest region of sensitivity is between 325 and 400 nm.

### Total energy deposition

Although the total energy of excited gadolinium is 8 MeV [45], the full energy is rarely measured. For example, a high-energy electron will emit Cherenkov radiation from high energy down to 252 keV. Fig. 3.8 shows the measured gadolinium neutron capture energy spectrum in the very large Super-Kamiokande water detector. Since the gamma scattering length is small relative to the dimensions of the detector, the gammas an be assumed to scatter entirely within the detector [45]. Though the histogram extends to 8 MeV, the average energy deposition is roughly half of the gadolinium excited state energy, 4.3±0.1 MeV. This is because some energy escapes detection, such as when an electron deposits energy below the Cherenkov threshold of 252 keV.

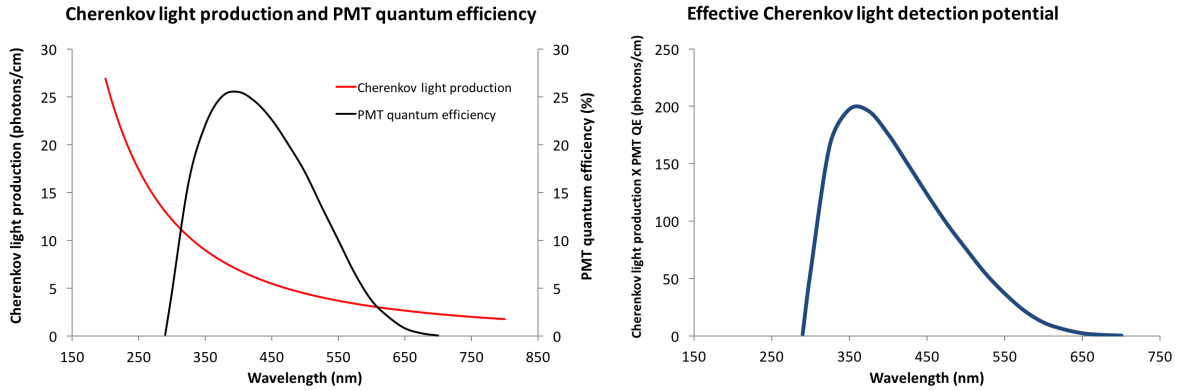


Figure 3.7: Cherenkov photon production and PMT quantum efficiency (QE). (left) Cherenkov light production and PMT quantum efficiency. (right) Convolution of Cherenkov light production and PMT quantum efficiency. Y-axis arbitrary. Adapted from [28] and [49].

Because the WaND is smaller than Super-Kamiokande, some gammas will leak out of the detector. As such, another conversion efficiency is applied to Fig. 3.8, discussed in Section 3.5.

## 3.4 The simulated detector

To determine neutron detection efficiency and test various hypothetical sources, a Geant4 [50], [51] model of the WaND was created. The simulation includes all relevant physics processes described in Section 3.3, including neutron scattering and absorption, gadolinium gamma emission, Compton scattering, and Cherenkov radiation generation, but *not* detector threshold effects. The geometrical and material description of the detector allows for any source to be inserted into the sample well.

The simulation was tuned by adjustig the wall reflectivity, water attenuation, and PMT efficiency until the best agreement with real data was obtained. The optimal values were 93% for average wall reflectivity, water attenuation length of ∼35 meters, and PMT efficiency of 85% nominal.

The measured and simulated neutron spectra match above ∼25 photoelectrons, but not below because the simulation does not account for PMT trigger effects. The simulated small peak centered around ∼15 photoelectrons most likely results from the 2.2 MeV [46] gamma from hydrogen capture, which is not visible in the measured spectrum because such low-energy events do not trigger the PMTs. The simulated spectrum includes neutrons that escaped out of the system (such as out of the top of the sample well), which accounts for the spike at zero photoelectrons in Fig. 3.9.

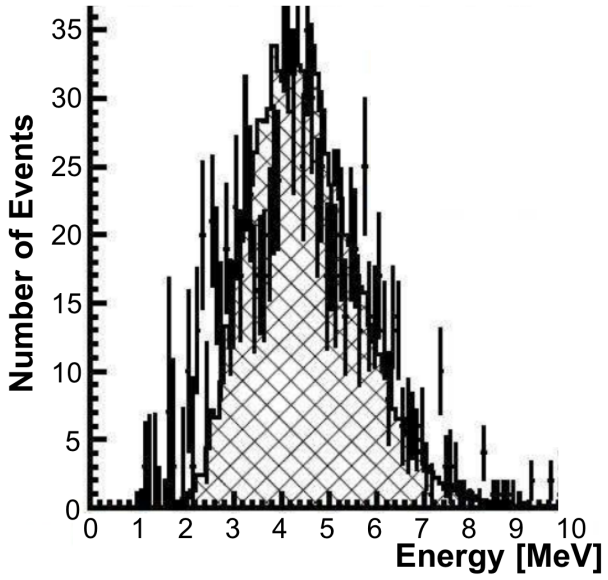


Figure 3.8: Gadolinium neutron capture energy spectrum as measured by Super-Kamiokande (points), and simulated (hashed histogram) [45].

## 3.5 WaND event generation

This section outlines the practicalities of neutron extraction: calibration, and utilizing the inter-event time distribution to extract the detector response to neutron capture. The WaND system records deposited energy and a time stamp for each triggered event. Event time stamps can be used for determining the gamma-neutron discrimination energy value and for multiplicity counting. When the WaND counts single neutrons, energy is used to discriminate between gamma and neutron events.

### 3.5.1 Single photoelectron calibration

The PMTs operate at roughly $10^7$ gain, and are calibrated in the laboratory for single photoelectrons by using a green LED installed inside the detector [43] and controlled via an external pulse shape generator. For calibration, the trigger is set to record events in phase with the blinking LED pulsed at 1 kHz. The LED voltage and trigger frequency are adjusted until a single photoelectron pulse is clearly distinguishable from the baseline, as shown in Fig. 3.10. Various high voltages are then applied to the PMTs, and the difference in Gaussian mean between the zero and one photoelectron values is tabulated (fits demonstrated in red in Fig. 3.10). Finally, voltages are set to equalize all arbitrary gains (in terms of ADC values). This gives the conversion between ADC and photoelectrons, or the single photoelectron

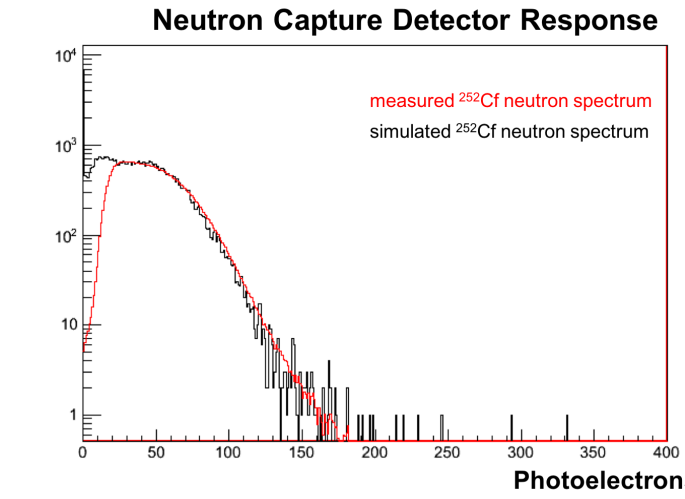


Figure 3.9: A comparison between measured and simulated neutron energy spectra. The simulated source in Fig. 3.9, like the experimentally measured source, was located at the bottom of the sample well. For simplicity, source neutron energies were set to 1 MeV [43].

calibration. Software calibration allows for final fine-tuning.

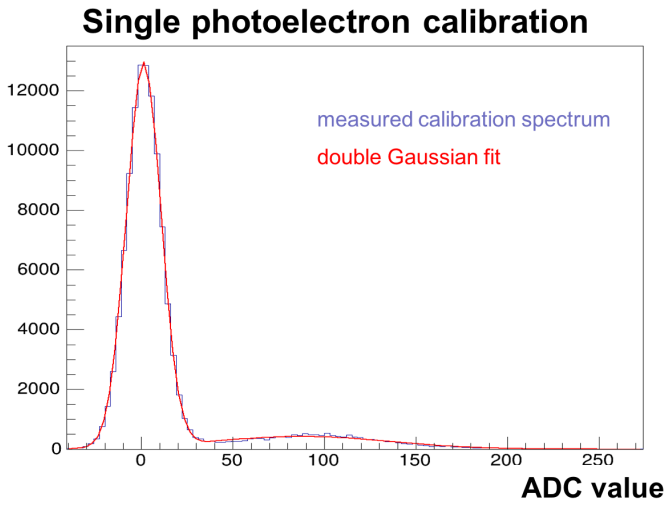


Figure 3.10: Zero (centered around zero ADC) and single (centered around 90 ADC) photoelectron calibration curve. Bold red lines are Gaussian fits to blue histogram.

### 3.5.2 PMT trigger multiplicity

*Trigger multiplicity* is the number of PMTs that must trigger above a preset threshold value before an event is recorded. For example, if only one PMT must trigger (a multiplicity of one), then any PMT dark current or detector noise will cause an event trigger; however, this would result in an overabundance of events caused by PMT noise triggers. The opposite extreme is to require a multiplicity of all eight PMTs; this would reject any event that does not deposit light in all eight PMTs, such as a real neutron event whose Cherenkov light is shadowed from one PMT by the sample well. Too high a trigger multiplicity will reduce the signal level. There is consequently an optimum PMT multiplicity that maximizes the signal-to-noise ratio.

When choosing the PMT trigger threshold and multiplicity, two aspects are considered. First, background gammas from the laboratory environment tend to dominate at low energies. If the threshold is set too low, the DAQ will be overwhelmed by background. Second, if the threshold is too high, neutron capture events will be missed. For this work the PMT trigger multiplicity was set so that the detector efficiency curve reaches 100% as quickly as possible. Fig. 3.11 shows the measured trigger efficiency as a function of deposited energy. Each curve represents a different PMT trigger multiplicity, from one to eight. The vertical axis shows the fraction of measured-to-simulated spectra heights (Section 3.4), and the horizontal axis is binned in single photoelectron values. Low photoelectron values demonstrate a low efficiency because the simulated spectrum includes these values, but they do not trigger the WaND in the laboratory. Higher photoelectron values (above ∼25 photoelectrons) show 100% efficiency because the measured and simulated spectra match. The three-fold PMT trigger efficiency in Fig. 3.11 has the steepest slope, and was considered the best trigger setting for maximizing neutron efficiency while rejecting low energy backgrounds.

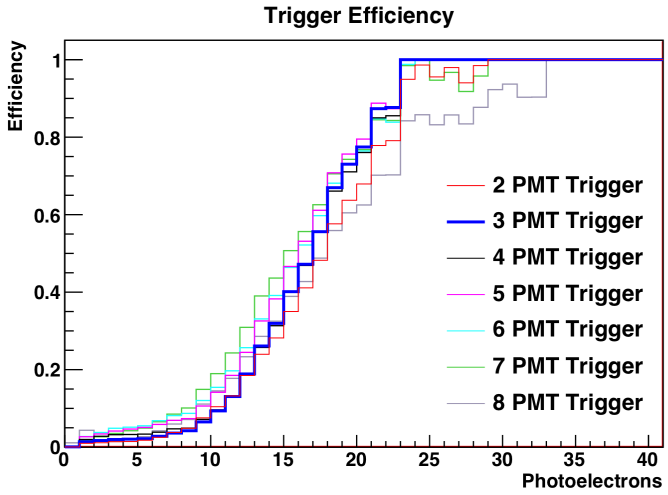


Figure 3.11: Trigger efficiency calculated as measured divided by simulated neutron spectrum as a function of photoelectrons.

### 3.5.3 The determination of the detector response to neutron capture via inter-event time

This section will describe how the inter-event time distribution can be used to extract the pure neutron capture detector response spectrum. The time stamp of each event can be used to isolate correlated bursts of neutron events from a wash of uncorrelated background events. Section 2.3 describes the basics of neutron counting and the origin of correlated and uncorrelated events. Fig. 3.12 shows that a measured WaND inter-event time distribution is comprised of two exponential functions: a steep function at low inter-event times (∼0-50 $\mu$s) and a shallow function at high inter-event times (∼200-1000 $\mu$s). A small additional component (∼50-100 $\mu$s) is due to neutrons that thermalize in the polypropylene sample well and capture on gadolinium. The shallow function at high inter-event times represents uncorrelated background events because these events have a relatively long inter-event time. The steep function represents correlated fission neutron events atop the uncorrelated background, because bursts of fission neutrons have a relatively short inter-event time. The intermediate function was experimentally discovered, and represents neutrons thermalizing in the polypropylene sample well before entering the water volume. For the sake of simplicity, the following discussion focuses on the steep and shallow exponential functions, but modification could be made to incorporate the intermediate function as well.

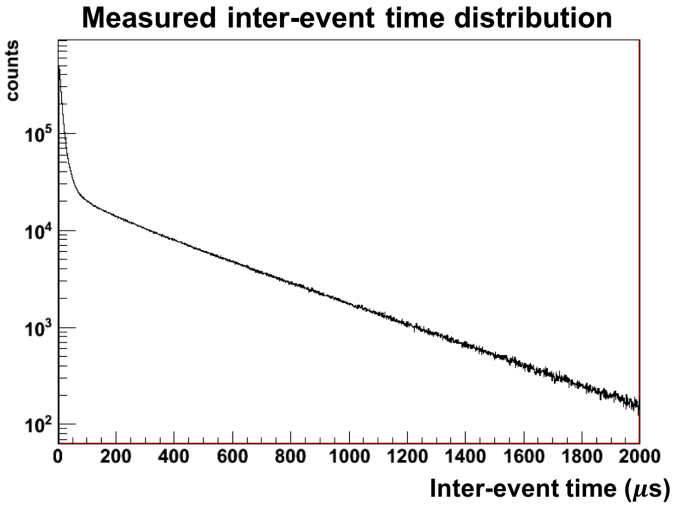


Figure 3.12: Measured inter-event time distribution for a 1-hour measurement of a 0.82 $\mu$Ci $^{252}$Cf source.

An algorithm was written to describe correlated fission neutrons from uncorrelated backgrounds. Fig. 3.13 illustrates the following algorithm steps:

(a) Plot events. This includes all long inter-event time uncorrelated (region II) and short inter-event correlated and uncorrelated (region I) events.

(b) Fit an exponential function $f(t)$ to long inter-event times, then extend that function to include short inter-event times, as shown by the red dashed line. The slope of this line is the background singles rate.

(c) Integrate $f(t)$ in region I at low inter-event times, define as variable $A$. $A$ is the number of uncorrelated background events in region I.

(d) Beginning at a high inter-event time where no correlated events exist, integrate a small section of the uncorrelated region I and define the integral as variable $B$. While $A > B$, increase the region I end point and integrate again. When $A = B$, regions I and II have the same number of uncorrelated events. However, region I also includes correlated events, while region II does not.

(e) Now the events from regions I (uncorrelated and correlated events) and II (only uncorrelated events) can be plotted and compared. The difference between the two spectra indicates the energy of only correlated events, as shown in Fig. 3.14.

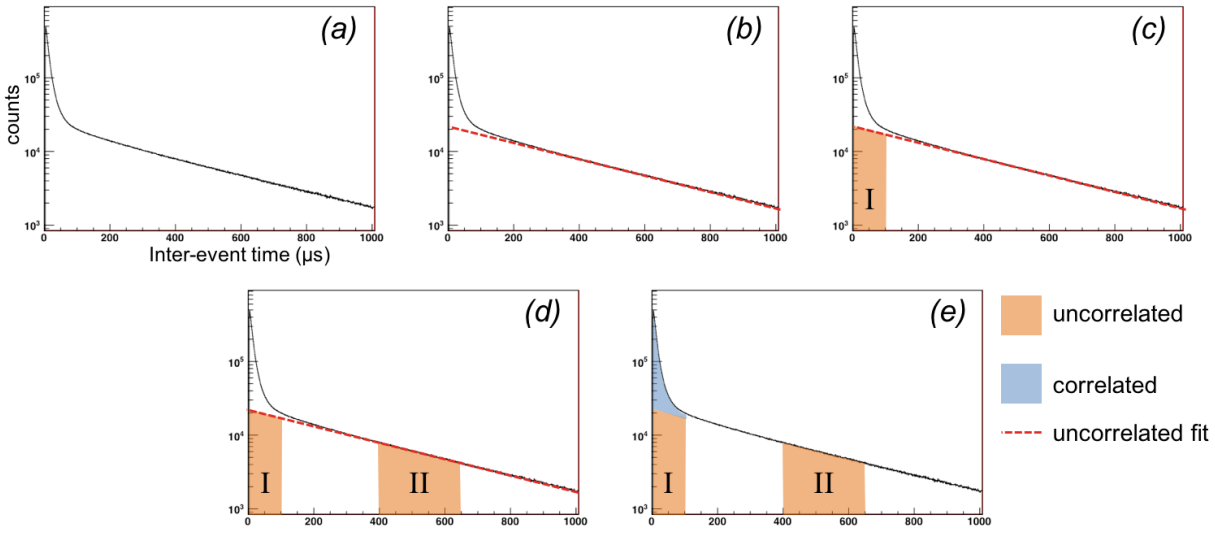


Figure 3.13: Schematic describing algorithm for isolating correlated events. Region I includes both correlated and uncorrelated events, while region II only includes uncorrelated events. Because the number of uncorrelated events in regions I and II are equal, the excess events in region I are only from correlated events.

Fig. 3.14 shows all events recorded from a 1-hour 0.82 $\mu$Ci $^{252}$Cf source, including correlated neutron events and random and correlated background events. By using the technique outlined in Fig. 3.13, the number of uncorrelated background events can be calculated. The statistical subtraction of correlated and uncorrelated events minus uncorrelated events then isolates correlated neutron events that originate from a $^{252}$Cf fission.

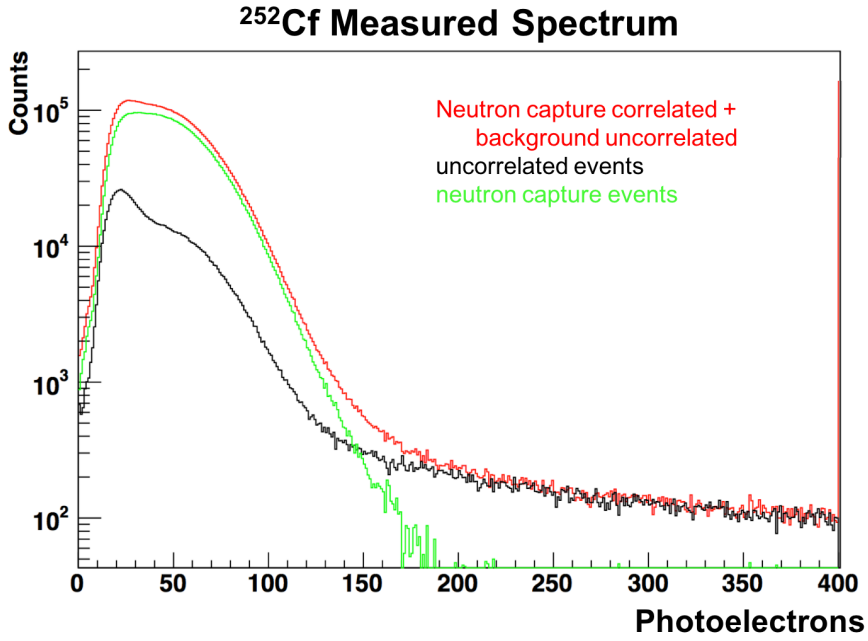


Figure 3.14: Energy spectrum of mixed and isolated uncorrelated and correlated events from a 1-hour measurement of a 0.82 $\mu$Ci $^{252}$Cf source. The statistical subtraction of (uncorrelated plus correlated) minus (uncorrelated) events leaves only correlated events due to neutron capture.

## 3.6 Detector response energy spectra

The extracted neutron spectrum from Fig. 3.14 can be compared with a gamma spectrum to determine a gamma/neutron discrimination threshold. Fig. 3.15 shows the detector response spectrum from background, from $^{60}$Co gammas, and from $^{252}$Cf neutrons.

### 3.6.1 Backgrounds

The red background spectrum in Fig. 3.15 exhibits two features: a low-energy peak centered around ∼25 photoelectrons, and a continuous spectrum at higher photoelectron values. The low-energy peak is due to low-energy gamma deposition from naturally occurring radioactivity. The low-energy detector response is a peak because threshold effects suppress very low-energy depositions (below ∼20 photoelectrons). Without threshold effects, the low-energy contributions would form a continuum increasing toward low energies.

The high-energy continuum results from cosmic-ray interactions. The muon flux is approximately 1/(cm$^2$ × min) at sea level, and accounts for approximately 80% of all cosmic-ray particles. The angular distribution follows a $cos^2\theta$ distribution, where $\theta$ is the zenith angle measured with respect to the vertical direction. Muons are minimum ionizing particles that

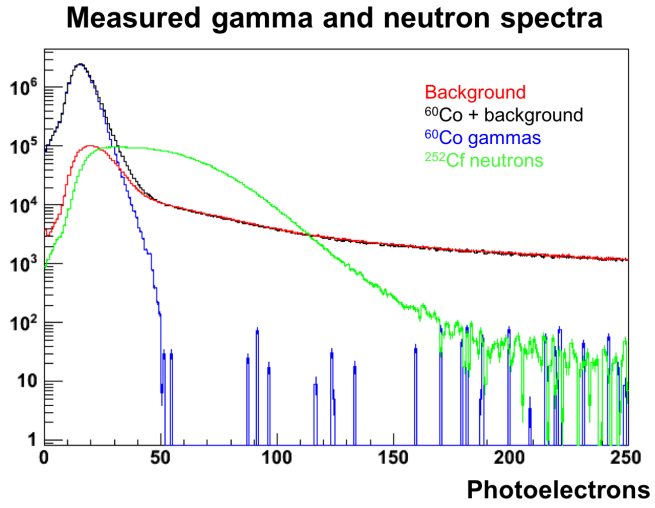


Figure 3.15: A typical detector response to background, to a 5.4 $\mu$Ci $^{60}$Co gamma source, and to a 0.82 $\mu$Ci $^{252}$Cf neutron source.

deposit 2 MeV/cm in water [47]. Due to the relative abundance of muons, their angular distribution, and their linear energy deposition, the detector response from cosmic rays is continuous. While a muon that clips the detector corner might deposit only a fraction of an MeV, a muon that passes through a meter-long section of the detector could deposit 200 MeV.

### 3.6.2 Gammas

To test the effect of low-level gammas on detector response, Fig. 3.15 also includes a 5.4 $\mu$Ci $^{60}$Co detector response spectrum that emits a 1.2 and 1.3 MeV gamma per disintegration. The black curve shows the effect of adding the $^{60}$Co source, atop the red background curve. The statistical subtraction of the background from this curve gives the pure $^{60}$Co gamma distribution shown in blue. The gamma detector response is centered around approximately 25 photoelectrons, and extends to 50 photoelectrons. As with backgrounds, detector threshold affects the shape of this spectrum at very low photoelectron values (below $\sim$20 photoelectrons).

### 3.6.3 Energy discrimination

The neutron detector response spectrum is shown in green in Fig. 3.15. While the $^{60}$Co gamma contribution extends 0 to 50 photoelectrons, the $^{252}$Cf neutron contribution extends to $\sim$200 photoelectrons. A 50-photoelectron energy cutoff can therefore be used on background-subtracted spectra to discriminate between $^{60}$Co gammas and incident neutrons.

With this energy discrimination, the nominal single neutron detection efficiency is 28%, since that fraction of neutrons produce a detector response between 50 and 200 photoelectrons in the tuned Geant4-based detection simulation. This is calculated as the number of simulated events in the neutron region from 50 to 200 photoelectrons divided by the number of neutrons emitted by the $^{252}$Cf source over the same time period.

When last measured in October 2007, the $^{252}$Cf source activity was 185 kBq with approximately 10% uncertainty. In 2015 (2.26 half-lives later), the source strength was (38 $\pm$ 4) kBq. The WaND detected 1230 out of a possible 4400 neutrons per second, implying an efficiency of (28 $\pm$ 3)%, ignoring the possible contribution from fission gammas (efficiency estimated in Section 4.1.5). As will be discussed in Chapter 4, this is the combination neutron and gamma efficiency for $^{252}$Cf because high energy $^{252}$Cf gammas can create a neutron-like detector signal. The measured neutron count was also compared with the simulated neutron spectrum, yielding the same results. The 50-photoelectron energy discrimination also discriminates $^{60}$Co by a factor of $10^8$ [43].

# Chapter 4

# Isotope identification and mass determination using neutron multiplicity counting

Traditional neutron counting has relied on determining the number of single, double, and triple neutron coincidences within a certain time window (Sec. 2.3), then using a deterministic method to predict the $^{240}\mathrm{Pu}_{eff}$ (Sec. 2.3.3). However, advances in data acquisition, digitization, and detector technology now make it possible to use an algorithmic approach to measure $^{240}$Pu mass. The WaND data acquisition system (Sec. 3.2) allows all events that meet certain trigger criteria to be recorded, then analyzed post-process. This affords significant flexibility in data analysis and supports the creation of data-parsing algorithms. Furthermore, because the WaND is a homogeneous detector, the neutron die-away time is relatively simple and can be modeled using an exponential die-away function. This chapter describes using these advanced techniques in neutron counting with the WaND system for element identification and $^{240}\mathrm{Pu}_{eff}$ mass prediction.

## 4.1 Simplistic Monte Carlo simulation of inter-event time distribution

Because the WaND is a homogeneous detection medium, neutron capture event times can be predicted using a simplistic Monte Carlo algorithm. The goal of this section is to describe the timing structure of detected events, as well as elaborate on the Monte Carlo algorithm used to predict the neutron capture inter-event time distributions. This information can be used for isotope identification and plutonium mass determination. Furthermore, because fission events produce high-energy gammas that mimic neutron signals, this simulation also aids in the precise measurement of of gamma and neutron efficiency.

### 4.1.1 Inter-event time distribution of a fission event

After a sample fission, gammas may enter the detector and produce a prompt event which almost exactly corresponds to the time of fission depending on the efficiency of the detector to fission gammas. If neutrons are also produced, they may be thermalized and captured in the detector, producing delayed events. The time at which a neutron event is detected depends on the thermalization and capture time. For fast neutrons immediately following fission, the probability of neutron capture is extremely low because the neutron capture cross-section is low at high energies. However, as the neutrons thermalize, the capture cross-section increases and capture becomes increasingly more likely. Once the neutrons become thermalized, their capture time can be modeled by an exponential capture time distribution. Fig. 4.1 illustrates the time at which the detector will see an event, including thermalization and capture times.

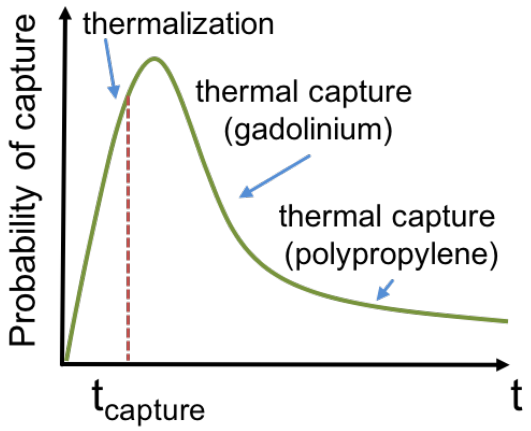


Figure 4.1: A schematic representing the probability of neutron capture following a fission event. The dotted line represents a hypothetical capture time, $t_{capture}$.

More analytically, neutron detection times can be modeled as exponential functions of thermalization and capture time. The time of a neutron capture following a fission event is given by [52]

$$t_{capture} = A_1 e^{-t/\lambda_{Gd}} + A_2 e^{-t/\lambda_H} + A_3 e^{-t/\lambda_T}$$

where $t$ is the time since fission and the unknowns $A_1$, $A_2$, and $A_3$ must be determined. At $t = 0$, $A_1 + A_2 + A_3 = 0$. A simplification can be made that $A_2$ is small compared to the other constants because it is a small correction for the neutrons that thermalize in the sample well, so $A_1 + A_3 \approx 0$. The time constants $\lambda_{Gd}$, $\lambda_H$, and $\lambda_T$ are the gadolinium and hydrogen capture times, and the thermalization time, respectively. $\lambda_H$ is the thermal capture time on hydrogen, and is a small overall correction because $A_2$ is small. The literature value of 200 $\mu$s was chosen [53] and because so few events are seen with this capture time, it is impossible

to precisely tune. $\lambda_{Gd}$ and $\lambda_T$ were tuned until the simulated and measured inter-event time distributions matched. The following values were used in the model:

$A_1 = 1.0$,
$A_2 = 0.015$,
$A_3 = 1.3$,
$\lambda_{Gd} = 18$ $\mu$s,
$\lambda_H = 200$ $\mu$s, and
$\lambda_T = 5$ $\mu$s [52].

$A_1$ does not exactly equal $A_3$ because this combination of constants produced the inter-event time distribution that best matched measured data.

### 4.1.2 Independent model inputs

Events measured from experiment can be categorized into the following for simplification: background uncorrelated events, background correlated, and source correlated events. Background uncorrelated events are ones that occur from single gamma, neutron, muon, etc. events that create a single pulse of detector output. The rate of uncorrelated background events is measured and input into the simulation. Background correlated events are clusters of muogenic neutrons and are input into the model at a rate that fits measured data. Correlated source events are groups of events that come from single fission events. The input fission rate is nominally taken as the source strength, as measured by the manufacturer. In summary, the simplistic Monte Carlo simulation has the following independent inputs [52]:

1. background singles rate,
2. background correlated rate,
3. source fission rate,
4. gamma efficiency, and
5. neutron efficiency.

Inputs 1 and 2 were independently tuned to the model until the background measured inter-event time distribution matched the simulated distribution (Section 4.1.3). The multiplicity distribution for a given isotope is shown in Fig. 2.5 and Appendix A. The multiplicity distribution of the background correlated rate was chosen as a flat function from one to nine neutrons. A source matching the laboratory source was then added (Section 4.1.4). Finally, items 4 and 5 were tuned with the help of a Geant4 simulation and comparison to laboratory data (Section 4.1.5) [52].

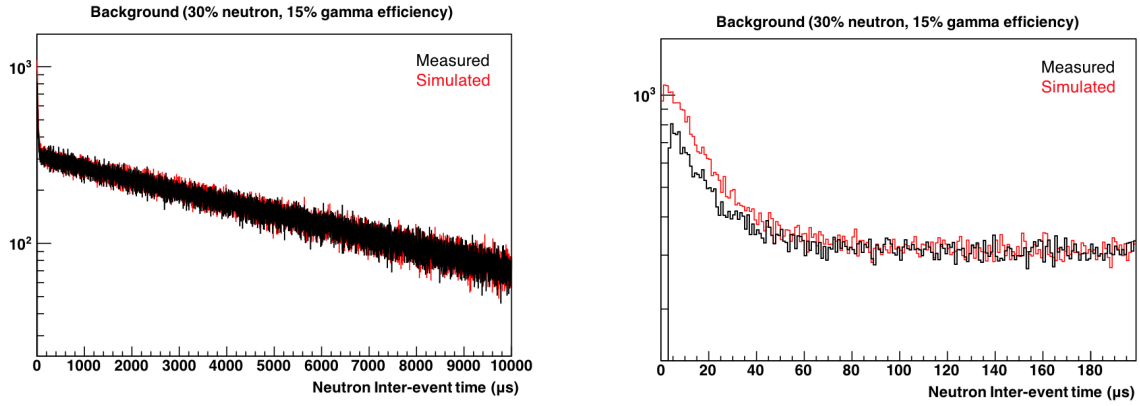


Figure 4.2: An example of poorly-matched background inter-event time distributions. (left) The full inter-event time distribution showing the relatively well-matched long inter-event times, and (right) a zoomed-in view showing the mismatch at short inter-event times.

### 4.1.3 Fitting the model to measured data

To tune the model parameters, the input parameters were tuned and compared to measured data until the two matched. The background singles and correlated rates were tuned until simulated long and short inter-event times roughly matched. The measured background singles rate is 143.55 Hz, and the tuned background correlated rate is 5.0 Hz. The singles rate was measured as the singles rate in the detector, then decreased slightly because the measured data includes the singles and correlated rate. Because the model takes these two parameters as independent inputs, each was slightly tuned to match the measured data. The gamma and neutron efficiencies were then tuned and compared. For example, Fig 4.2 shows a relatively poor match between simulation and real data due to high neutron and gamma efficiency. The background measured data was taken for one hour, and the simulation was run for an equivalent acquisition time of one hour. Long inter-event times match reasonably well because they are dominated by the singles background rate, which was already measured. However, the simulated correlated component does not match the measured data at short inter-event times because the neutron and gamma efficiencies are too high, causing an over-estimation in the number of detected correlated events (more detail in Section 4.1.5).

However, decreasing the neutron and fission gamma efficiencies to more reasonable values creates a better agreement between the measured and simulated data. Fig. 4.3 shows an example of measured and simulated gamma and neutron background spectra that are more in agreement.

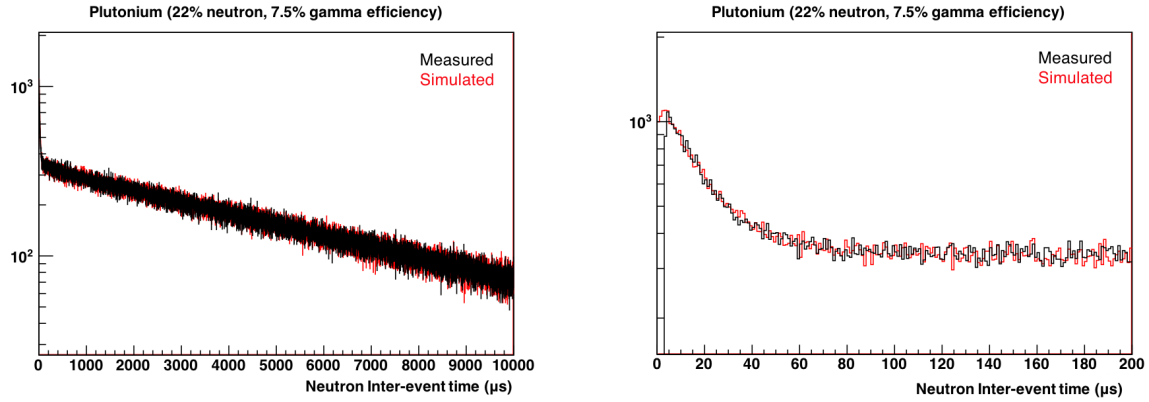


Figure 4.3: An example of well-matched plutonium time distributions at (left) long and (right) short inter-event times. Note that the real data has 3 $\mu$s of dead time, so the algorithm only compares data above 3 $\mu$s.

### 4.1.4 Adding a fissioning source

After the background singles and correlated rates were set to match the corresponding measured data, a plutonium source was added to the simulation. Because the Monte Carlo simulation projects only the timing response of the detector, a fission $^{240}$Pu term was added to insert additional events at a 6.64 Hz fission rate to match the laboratory source described in Section 4.2.

Fig. 4.3 shows a well-matching inter-event time distribution for a sample source and background run. The measured data was taken with the plutonium source described in Section 4.2. The laboratory data was measured for one hour, and the simulation run for an equivalent acquisition time of one hour. Note that compared to Fig. 4.3, the correlated rate is significantly higher, while the background rate is unchanged.

### 4.1.5 Fission neutron and fission gamma efficiency calculation

With the background correctly modeled and the fission source added, the final parameters to tune are gamma and neutron efficiency. However, the inter-event diagrams, such as Figs. 4.2 through 4.3, do not offer a single solution for the correct gamma and neutron efficiency as there are two degrees of freedom. It was therefore necessary to create a systematic measure of goodness of fit between simulation and data to assess which efficiencies fit best.

Many (142) inter-event time distributions were simulated with fission gamma efficiencies ranging from 0 to 30%, and neutron efficiencies 21-31%. A $\chi^2$ goodness of fit test was then applied separately on the uncorrelated and correlated portions of each inter-event time distribution with a unique gamma and neutron efficiency. The $\chi^2$ goodness of fit test is given

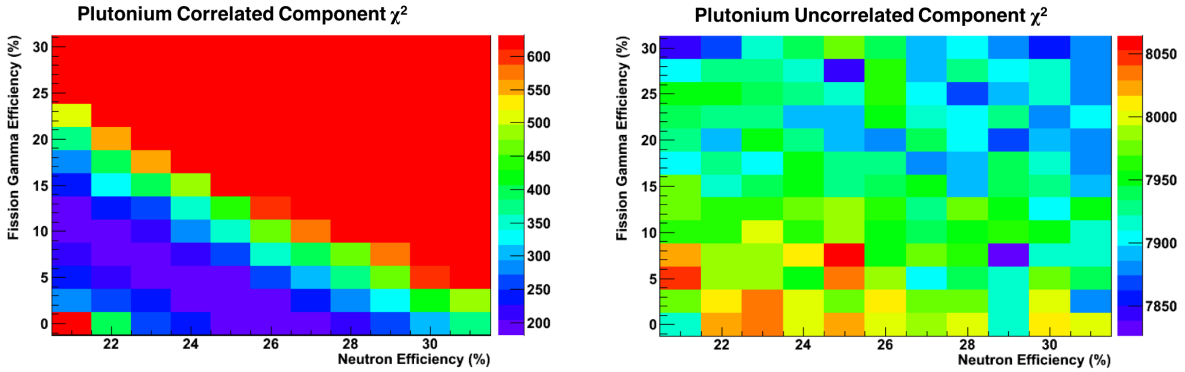


Figure 4.4: $\chi^2$ analysis of the (left) correlated and (right) uncorrelated portions of inter-event time distributions for various gamma and neutron efficiencies.

by

$$\chi^2 = \sum_{i=1}^{n} \frac{(x_{sim,i} - x_{meas,i})^2}{\sigma^2_{meas,i}}$$

where the $\chi^2$ test is performed from bin 1 to $n$ and $x_{sim,i}$ denotes the bin content of the simulated histogram at bin $i$, $x_{meas,i}$ denotes the same for the measured histogram, and the error $\sigma_{meas,i}$ is given by

$$\sigma^2_{meas,i} = (\delta N)^2 = \left(N \times \frac{\delta N}{N}\right)^2 = \left(N \times \frac{\sqrt{N}}{N}\right)^2 = N.$$

For inter-event time distribution, the $\chi^2$ value is calculated for each bin, then summed over the region of interest (correlated and uncorrelated). The correlated region of interest includes the initial 100 bins, and the uncorrelated region contains the last 4000 bins.

Figure 4.4 shows the results of the $\chi^2$ test over the correlated (left) and uncorrelated (right) portions of the inter-event time distribution. Because $\chi^2/NDF \approx 2$ for all values of gamma and neutron efficiency, the uncorrelated $\chi^2$ result is not conclusive regarding which gamma and neutron efficiencies create simulated data that most closely matches the measured data. This is because the background rate is not heavily effected by the neutron and fission gamma efficiency. However, the correlated component shows a definitive trend of lower $\chi^2$ values for fission gamma efficiencies of ~5-15% and neutron efficiencies of ~20-28%. Because no single solution exists for most probable gamma and neutron efficiencies, the Geant4 simulation (see Section 3) was used to determine the fission gamma efficiency, then the simplistic Monte Carlo was used to singularly determine the neutron efficiency by matching to measured data.

### Determining fission gamma efficiency

The Geant4 Monte Carlo WaND detector model, as described in Section 3, was used to simulate plutonium gammas and measure the resulting fission gamma efficiency. In order to break the degeneracy between the fission gamma and neutron capture efficiencies predicted by the simplistic Monte Carlo, the previously tuned Geant4 Monte Carlo WaND detector model (see Section 3) was used to determine the fission gamma efficiency alone.

A plutonium gamma generator was used to more closely model the plutonium gamma energies. The generator first sets the average gamma energy to [54]

$$\bar{E_\gamma} = -1.33 + \frac{119.6 \times Z^{1/3}}{A}.$$

The generator then determines the sum energy of the gamma cascade $E_{total,\gamma}$ from a Gaussian function with a mean of $\bar{E_\gamma}$ and a width of $0.3 \times \bar{E_\gamma}/6.95$ [54]. Then the number of gammas emitted in the cascade are estimated as the ratio of total gamma energy to the average gamma energy, $E_{total,\gamma}/\bar{E_\gamma}$. With the total gamma energy and the number of gammas per fission set, the generator then produces individual gammas. For each gamma produced, the generator samples the input gamma spectrum from Fig. 4.5. The generator keeps a running tally of the total gamma energy minus the energy of the gammas already produced. Once this tally or the number of gammas left in the cascade reaches zero, the gamma cascade is terminated. Sampling in this manner allows the gamma multiplicity and total gamma energy to be conserved.

Fig 4.6 shows the resultant gammas from the gamma generator. The single gamma energy plot (left) shows the energy of every single gamma modeled. The total gamma energy (middle) shows the total gamma energy emitted per fission. The gamma multiplicity (right) shows the number of gammas emitted per fission. All are on a log-linear scale.

After each single gamma is sampled and the energy determined, all gammas in the fission are shot isotropically into the detector and the detector response is calculated. Fig. 4.7 shows the detector response to these plutonium gammas from the base of the well. The simulation was run for extremes of high and low energy gammas sampled to determine the error on fission gamma efficiency. The high-energy extreme gammas were sampled from the high bounds of the error bars in Fig. 4.5, and the low-energy extreme gammas were taken from the low bounds of the error bars. Gamma efficiency was calculated as the proportion of the detector response contained in the neutron search region between 50 and 200 photoelectrons at $(5.25 \pm 0.15)\%$.

### Determining neutron efficiency

Once the fission gamma efficiency was estimated, Fig. 4.4 can be used to determine the corresponding neutron efficiency. To obtain the highest and lowest potential neutron efficiencies, the lowest and highest gamma efficiencies were used to produce $\chi^2$ plots like Fig. 4.4. Each plot was analyzed for the potential corresponding neutron efficiency.

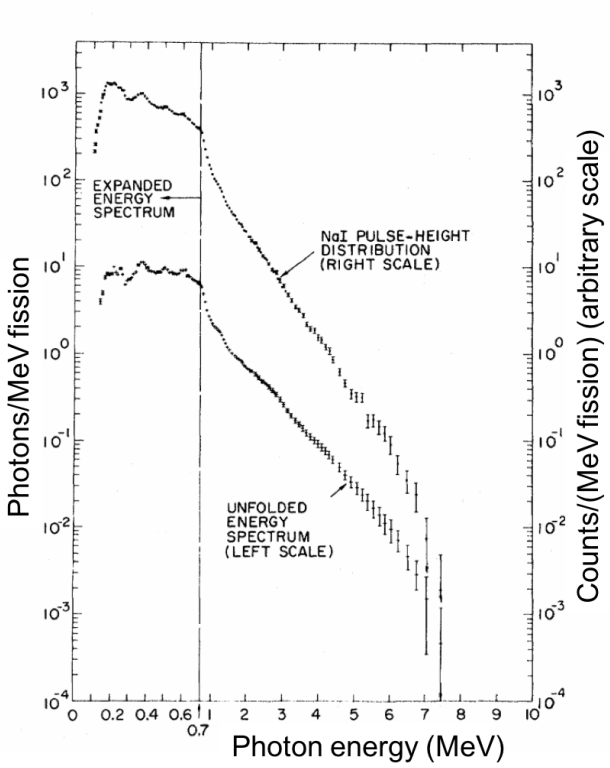


Figure 4.5: Prompt gammas from $^{252}$Cf fission. The unfolded spectrum was used in gamma sampling. Adapted from [55]

First the fission gamma efficiency was set to either 5.1% or 5.4%, then inter-event times were simulated for neutron efficiencies ranging from 20 to 30% at increments of 0.2% to set the upper and lower bounds of the fission gamma efficiency estimate. This technique is essentially equivalent to scanning Fig. 4.4 horizontally for a fixed fission gamma efficiency, but at a finer grain. Fig. 4.8 shows the results of the scan, including a quadratic fit to the $\chi^2$ values. For a fission gamma efficiency of 5.4%, the most probable neutron efficiency is $(23.3 \pm 0.8)$%. For a fission gamma efficiency of 5.1%, the most probable neutron efficiency is $(23.4 \pm 0.6)$%. The neutron efficiency is then $(23.4 \pm 0.8)$%, where uncertainties were estimated from the uncertainties of the fit.

## 4.2 Laboratory plutonium source

These experiments utilized a laboratory mixed-oxide plutonium source contained inside a puck-shaped stainless steel container 1.00 inches in height and 2.8 inches diameter. Inside the puck is a hollow cylindrical sample area with a height and diameter of 0.25 inches. The

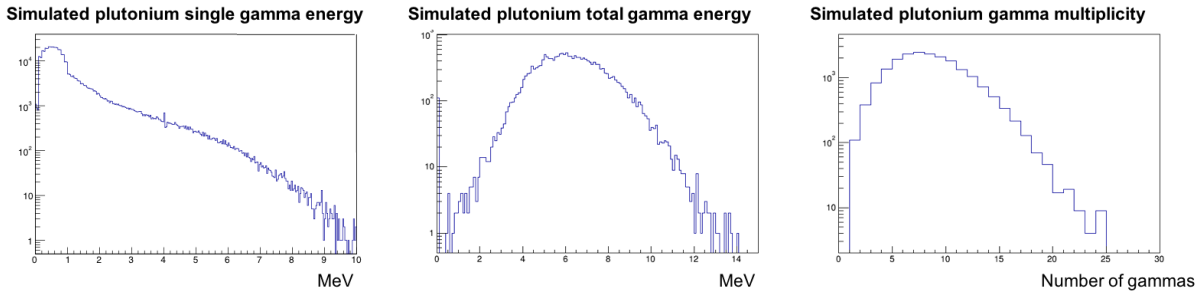


Figure 4.6: Single and total fission gamma energy and gamma multiplicity as simulated by the gamma generator using Geant4. Each vertical axis shows counts.

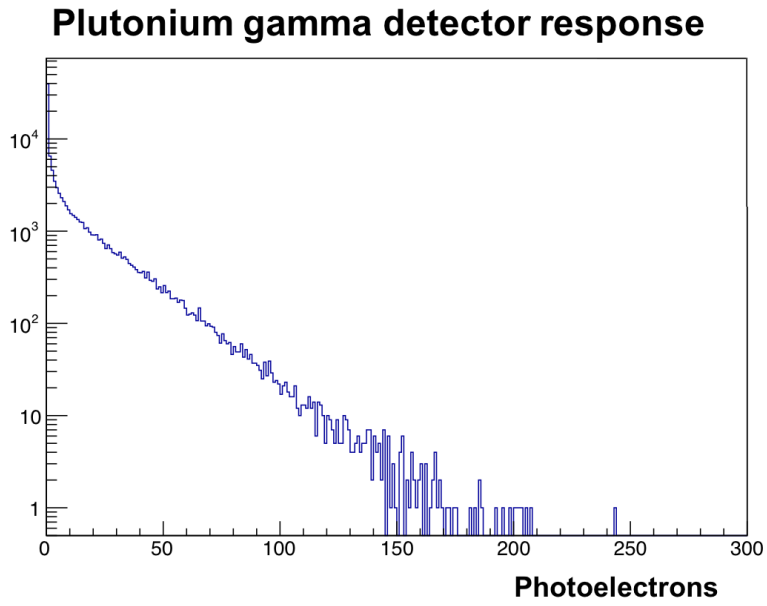


Figure 4.7: Plutonium gamma detector response.

plutonium sample attributes are outlined in Table 4.1. The nominal source fission rate is 6.64 Hz and the average neutron multiplicity is $\bar{\nu} = 2.16$ neutrons/fission. A weak laboratory $^{252}$Cf was also utilized. Because the source is approximately 10 half-lives old, much of the $^{252}$Cf has decayed away, leaving a large fraction of $^{250}$Cf. The source emits ∼280 neutrons/s from $^{252}$Cf and ∼100 neutrons/s from $^{250}$Cf.

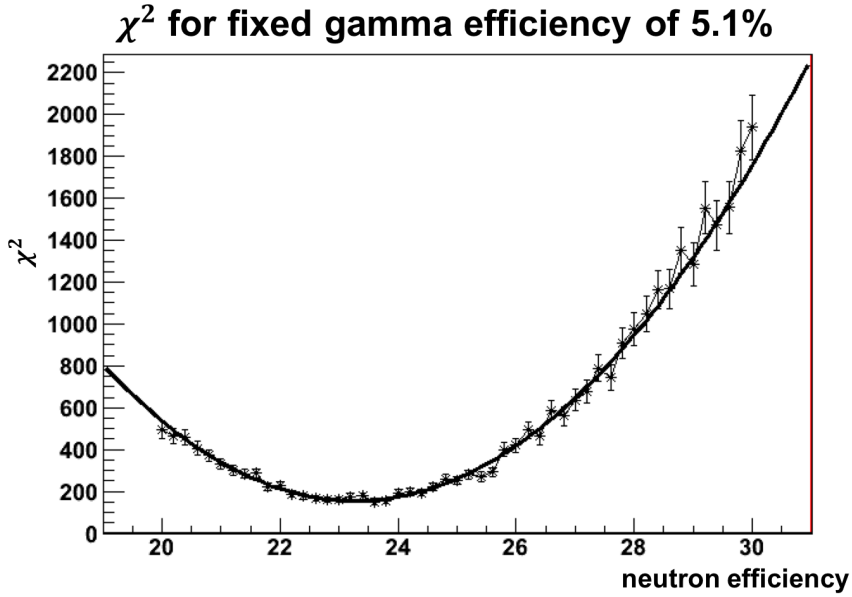


Figure 4.8: Scanned $\chi^2$ values for a fixed gamma detection efficiency of 5.1% and neutron efficiencies ranging for 20-30%. The data is fit with a quadratic equation, the minimum of which represents the most probable neutron detection efficiency.

Table 4.1: Laboratory plutonium source characteristics

| **isotope** | **weight (g)** | **neutrons/s/g** | **neutrons/s** |
|---|---|---|---|
| $^{238}$Pu | $1.00\times10^{-4}$ | $2.59\times10^{3}$ | $2.59\times10^{-1}$ |
| $^{239}$Pu | $2.15\times10^{-1}$ | $2.18\times10^{-2}$ | $4.68\times10^{-3}$ |
| $^{240}$Pu | $1.38\times10^{-2}$ | $1.02\times10^{3}$ | $1.41\times10^{1}$ |
| $^{242}$Pu | $3.00\times10^{-4}$ | $5.00\times10^{-2}$ | $1.50\times10^{-5}$ |
| Total | | | 14.34 |

## 4.3 Element prediction

Following the precise determination of gamma and neutron efficiency, the Monte Carlo model was applied to predict the measured element or isotope.

The isotope identification algorithm compares a measured neutron multiplicity distribution to simulated ones for $^{235}$U, $^{238}$Pu, $^{240}$Pu, $^{244}$Cm, and $^{252}$Cf. Of the neutron multiplicity distributions shown in Fig. 2.5 and Appendix A, $^{235}$U, $^{238}$Pu, and $^{240}$Pu have similar average neutron multiplicity and spread but $^{244}$Cm and $^{252}$Cf have distinct distributions.

The algorithm subtracts a simulated background from each neutron multiplicity distribution, then compares the simulated and measured background-subtracted neutron multiplicity distributions to determine which simulated isotope best fits the measured data. Several

methods were tested for this comparison, and the ratio of doubles to triples was empirically chosen as the best predictor of the measured isotope. The ratio of doubles to triples is an observable based in the neutron multiplicity distribution shape.

Table 4.2: Simulated and measured doubles-to-triples ratios for various isotopes.

| **isotope** | **simulated n=2/n=3** | **measured n=2/n=3** |
|---|---|---|
| $^{235}$U | 10.1 ± 0.8 | |
| $^{240}$Pu | 10.8 ± 0.8 | 8.8 ± 2.6 |
| $^{252}$Cf | 6.0 ± 0.5 | 5.3 ± 0.1 |
| $^{244}$Cm | 9.3 ± 0.7 | |

Table 4.2 shows the result of this study. The measured data is from one-hour runs. The simulated data is from high-statistic runs equivalent to a five day run time for most isotopes and a 12 hour run time for $^{252}$Cf. All simulated data were done with a 10 Hz fission rate and a 100 Hz fission rate for $^{252}$Cf. The simulated $^{252}$Cf fission rate is higher to match the lowest-available laboratory source more closely and the higher fission rate increases the chances of overlapping fissions, skewing the measured multiplicity distribution to higher values. The simulated neutron multiplicity distribution for most isotopes is taken from the spontaneous-fission emitted neutron multiplicity; $^{235}$U, however, is based on the thermal neutron capture $(n, fission)$ reaction.

The simulated errors include both statistical and systematic errors. Because the ratio of n=2/n=3 utilizes the background-subtracted doubles and triples bin counts, both the source and background statistical errors must be taken into account. The background-subtracted statistical uncertainty in the doubles and triples bin is then given by

$$\delta(source - background)|_{n=2,n=3} = \sqrt{\delta(source)^2 + \delta(background)^2} \tag{4.1}$$

where $\delta(source)$ and $\delta(background)$ are the Poisson errors in each bin. The uncertainty in the ratio of n=2/n=3 is then

$$\delta(n = 2/n = 3) = \sqrt{\left(\frac{\delta(n=2)}{n=2}\right)^2 + \left(\frac{\delta(n=3)}{n=3}\right)^2} \tag{4.2}$$

where the uncertainties $\delta(n = 2)$ and $\delta(n = 3)$ are given by Equation 4.1 and $n = 2$ and $n = 3$ are simply the doubles and triples bin contents.

The simulated systematic errors are propagated from the uncertainty in the neutron efficiency from Section 4.1.5. The fractional uncertainty due to neutron efficiency for doubles and triples bins are 4% and 6%, respectively. The total error is the summation in quadrature of the statistical and systematic errors.

The measured errors are purely statistical. The plutonium statistical uncertainty was measured by taking a series of ten one-hour plutonium runs. The double and triple neutron coincidence bin had $(746 \pm 69)$ and $(59 \pm 16)$ counts per hour, respectively to one standard

deviation. The fractional statistical uncertainty is therefore 9% and 29%, respectively for the doubles and triples bins. The californium statistical uncertainty utilized Equations 4.1 and 4.2.

The simulated data in Table 4.2 shows that there is a clear distinction between some fissioning isotopes but not others. For example, it would be difficult, even with extremely high statistics, to differentiate between the $^{235}$U and $^{240}$Pu because the simulated doubles to triples ratio is within error of each other. However, measuring the difference between $^{235}$U/$^{240}$Pu and either $^{252}$Cf or $^{244}$Cm is more feasible. From the measured data, it would be possible to differentiate between the laboratory $^{240}$Pu and $^{252}$Cf within one hour.

The measured data slightly under-predicts the expected doubles-to-triples ratio, due most likely to an unaccounted-for effect in the simulation that increases the triples or decreases the doubles rate. Also, because the measured data was taken for an hour to simulate real laboratory conditions with time constraints, the error bars are relatively large.

## 4.4 Plutonium mass prediction

If the source is identified as plutonium, the rate of triple neutron coincidences can be used to determine the plutonium mass. This discussion can be extended to other fissioning isotopes; however, plutonium was chosen as a proof of principle.

The simplistic Monte Carlo algorithm now has good estimates of fission gamma and neutron detection efficiencies and capture times that match the observed detector inter-event times combined with a model that fits the background timing distribution. These detector parameters can be applied to measure the unknown fission rate of any $^{240}$Pu source. First, a set of simulated neutron multiplicity distributions is created for plutonium at various fission rates. The measured neutron multiplicity distribution is compared to the simulated ones, and the best match predicts the fission rate. As with the isotope identification algorithm, several different comparison methods were attempted, and the method that best and most consistently predicted fission rate is the rate of triple neutron coincidences. While the ratio of doubles to triples is an observable related to the shape of the neutron multiplicity distribution, the rate of triples is an observable related to the height of the distribution – in other words, the rate of triples is proportional to the mass of the fissioning isotope.

Fig. 4.9 shows an example of the simulated rate of triples per hour, compared with measured data for the $^{240}$Pu 6.64 Hz fissioning source. The simulated data was created with an equivalent run time of 24 hours to minimize statistical error, then converted to triples rate per hour. The measured data was taken for one hour to simulate a reasonable acquisition time in a laboratory setting. The relatively large error bars on the measured data result from statistical uncertainty.

The laboratory plutonium source was used as a proxy for different masses of plutonium to check the robustness of the algorithm. To simulate the presence of a 4.6 mg $^{240}$Pu source with a fission rate of 2.2 Hz (1/3 the nominal source activity of 6.6 Hz), the source would be placed in the well for 1/3 of a fill one hour data acquisition run. Although not ideal,

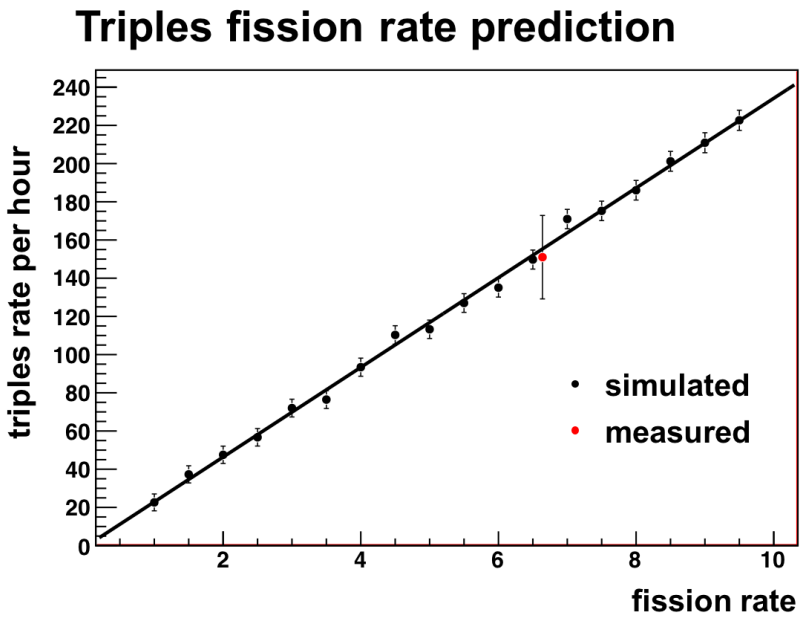


Figure 4.9: Measured and simulated triples rate as a function of fission rate. The input fission gamma efficiency was set to the mean of 5.25%, and neutron efficiency to 24.2%. This exercise was repeated to produce similar plots for various fission rates and a neutron efficiency of 22.6%.

this method is nonetheless valid because of the very low fission rate of the source; however, it is applicable only to sources for which an overlap of fissions is extremely unlikely. Using this method, three different equivalent plutonium masses were measured. Like Fig. 4.9, the measured triples rate is measured. It is then compared to the simulated triples bin rates. The simulated triples bin rate that most closely matches the measured triples rate is then determined. The corresponding fission rate that was used to make the simulated run is then the prediction of source fission rate.

The error on the measured plutonium mass consists of statistical and systematic errors. The fractional statistical uncertainty is 29% from Section 4.3. The systematic uncertainty consists of two parts: uncertainty due to neutron efficiency and the prediction of fission rate. Neutron efficiency uncertainty was accounted for by simulating extremely high statistic runs (five day equivalent run times) at 22.6% and 24.2% neutron efficiency. The background-subtracted triples bin content for 22.6% and 24.2% neutron efficiencies were ∼17,000 and ∼19,000 counts. The fractional uncertainty due to neutron efficiency is therefore 6% from the difference of the bin counts due to the highest and lowest potential neutron efficiencies. The fission prediction systematic error was estimated from the uncertainty in the line of best fit for Fig. 4.9, which was used to calculated measured fission rate. The fractional uncertainty

due to the error in the fission rate prediction is 2.6%. The total systematic uncertainty is the summation in quadrature of the two systematic components, 6.7%. The total fractional uncertainty is the summation in quadrature of the total statistical and systematic errors, 30%.

Fig. 4.10 shows the extent to which the measured and true plutonium masses agree. The laboratory source was measured for 20, 40, and 60 minutes in the well (with the remainder of an hour being background), corresponding to equivalent fission rates of 2.21, 4.43, and 6.64 Hz respectively. This was then converted to $^{240}$Pu masses of 4.6, 9.2, and 13.8 mg because the full 60-minute run with an equivalent fission rate of 6.64 corresponds to 13.8 mg $^{240}$Pu. Note that from Table 4.1, $^{240}$Pu dominates neutron emission by several orders of magnitude, so other isotopes were not accounted for.

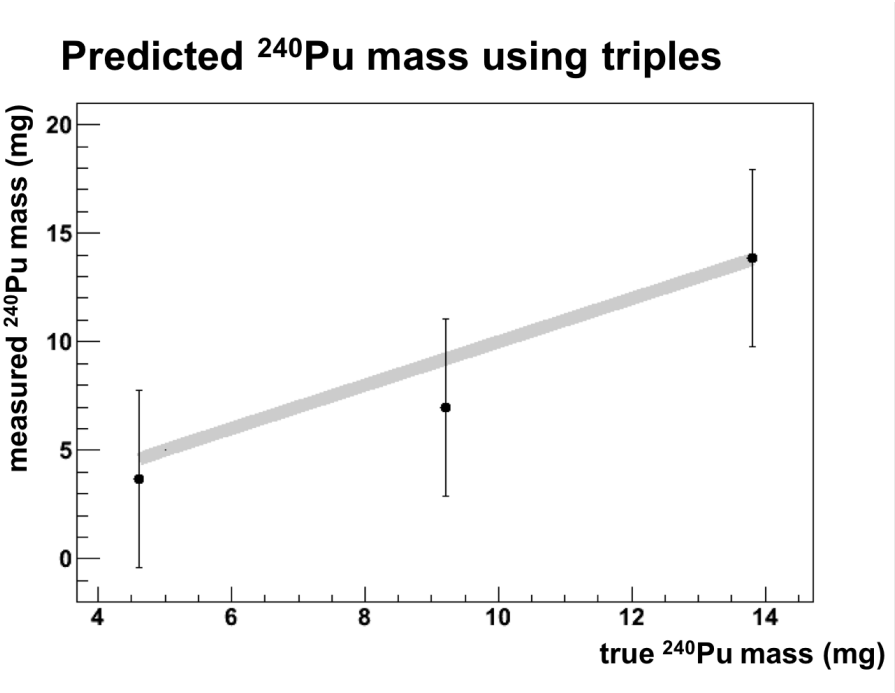


Figure 4.10: Predicted versus true $^{240}$Pu mass. The points represent data, and the thick gray line represents a line of perfect agreement between predicted and true $^{240}$Pu mass, with an intercept at (0,0).

The total absolute uncertainty in plutonium mass determination is 4 mg. The WaND system can therefore potentially predict the mass of $^{240}$Pu down to 4 mg.

## 4.5 Conclusion

The goal of neutron multiplicity measurements with the WaND system is to determine whether isotope identification and fission rate measurements are possible using an algorith-

mic approach to neutron multiplicity analysis. Traditional neutron multiplicity counting, outlined in Chapter 2, relies on a deterministic method for $^{240}\mathrm{Pu}_{eff}$ analysis. However, modern electronics have departed from shift registers and allow for the collection of large amounts of data, resulting in powerful post-process analysis. The combination of modern electronics and a powerful neutron detector has been beneficial in expanding the capabilities of neutron multiplicity analysis.

First, an algorithm was written to create a neutron multiplicity spectrum convoluted with the detector response. The $^{240}$Pu gamma and neutron efficiencies were determined to be $(5.25 \pm 0.15)\%$ and $(23.4 \pm 0.8)\%$, respectively. Another algorithm then used the ratio of measured doubles to triples to predict a measured isotope. Simulated results showed that it is possible to differentiate between $^{235}\mathrm{U}/^{240}\mathrm{Pu}$, $^{252}$Cf, and $^{244}$Cm. Simulated data showed that differentiating between a one-hour measured source of $^{235}$U, $^{240}$Pu, and $^{244}$Cm would prove difficult. However, there is a significant laboratory-measured difference between these and $^{252}$Cf. Another algorithm then correctly predicted the mass of $^{240}$Pu for a range between 4.6 to 13.8 mg with a one hour acquisition. With an error of $\sim$4 mg, it is potentially possible to measure down to 4 mg $^{240}$Pu.

Future work should include refining the isotope-identification algorithm to determine the source of systematic algorithm error and to better predict laboratory sources. This analysis can also be extended to other isotopes. The combination of isotope identification and mass determination could potentially make the WaND system a very powerful tool in radiation monitoring to search for signatures of smuggled fissile material.

# Chapter 5

# Effects of high intensity gamma backgrounds

Gamma/neutron discrimination is a challenge for virtually any neutron detector in the presence of a high intensity ambient gamma flux, and spent nuclear fuel represents the most extreme case. In order to accurately measure spent fuel plutonium content through neutron multiplicity counting, it is critical to determine the effect of a high gamma flux on neutron detection systems.

It has been shown that single low energy gamma events of around ∼1-2 MeV do not cause false positive neutron events in the WaND system [43]. However, an extremely high gamma flux, such as that originating from spent fuel, can have second-order effects on the detector response. First, this chapter explores the effect of $^{60}$Co gammas, followed by the effect of $^{60}$Co gammas on the neutron capture spectrum. Finally, a simulation of spent fuel gammas is shown, followed by using lead shielding to mitigate gamma effects.

## 5.1 Neutron signal degradation due to high gamma rates

The goal of this section is to determine the viability of WaND for neutron counting in the presence of a high gamma flux. The stretch goal and potential applicability lie in plutonium spent fuel assay. Previous work has shown that by employing an energy-based cut, single gammas up to 1.3 MeV ($^{60}$Co) can be removed, while maintaining neutron capture sensitivity of (23.4 ± 0.8)%. However, two problems may occur. While individual gamma events may produce a detector response below the analysis threshold of 50 photoelectrons, they nevertheless trigger the detector. As source activity increases, the trigger rate becomes unacceptably high. This problem is overcome by increasing the trigger threshold from the nominal value of 60 mV to 140 mV per PMT. This increase impacts the neutron detection efficiency slightly as will be shown. The second problem is that an intense flux can produce pileup that distorts the neutron detection response. Because physical and administrative

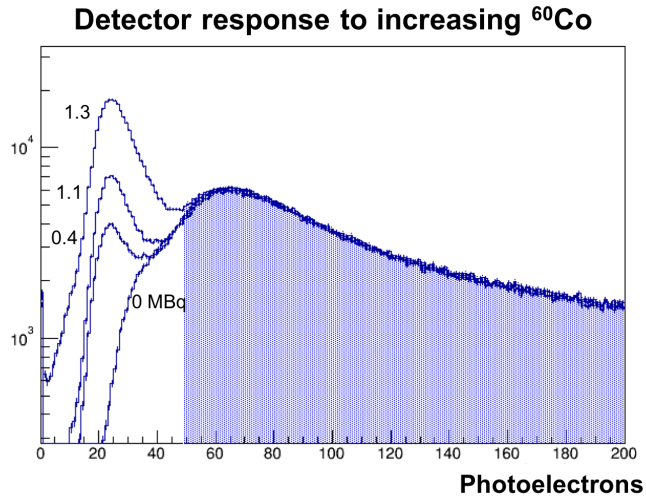


Figure 5.1: 1.3 MBq response with increasing $^{60}$Co activity from 0 to 1.3 MBq with a high (140 mV) PMT threshold. The lowest curve is background with no source present, and the increasing curves represent 0.4, 1.1, and 1.3 MBq of $^{60}$Co. The shaded area denotes the neutron search region between 50 and 200 photoelectrons

constraints preclude the analysis of an actual spent fuel sample, this chapter offers a systematic study of neutron capture response in the presence of high gamma rates with laboratory gamma source proxies and spent fuel simulation.

### 5.1.1 Experiment: $^{60}$Co detector response

#### LED proxy for an intense $^{60}$Co source

Fig. 5.1 shows the measured detector response to various $^{60}$Co sources ranging from 0 to 35.5 $\mu$Ci (1.3 MBq) using a high PMT threshold of 140 mV. The ingrowth of the peak centered around 25 photoelectrons shows that although $^{60}$Co is detectable, its contribution is below the neutron search region (50 to 200 photoelectrons) for these $^{60}$Co activity levels.

Because the highest laboratory-available $^{60}$Co activity of 1.3 MBq did not produce a noticeable degradation in neutron detector response, a pulsed LED was used in conjunction with the available $^{60}$Co sources to simulate high-activity sources. The approximate LED to $^{60}$Co-equivalent activity calibration involved three steps. First, the LED voltage, duty cycle, and flashing rate were adjusted until the LED detector response matched that of a 0.2 MBq $^{60}$Co detector response. The LED voltage was set to 1.22 V for a duration of 60 ns. Next, the LED trigger frequency was adjusted until the detector response spectrum matched the next available $^{60}$Co strength. Finally, to achieve $^{60}$Co-equivalent activity levels beyond what was available in the laboratory, the LED was set to a calibrated $^{60}$Co-equivalent value, a real $^{60}$Co source was added, and a detector response spectrum was measured. The $^{60}$Co source was

then removed and the LED trigger frequency tuned to match the previous detector response spectrum. This process was repeated until a 3.5 MBq $^{60}$Co-equivalent was simulated. Fig 5.2 shows the LED blinking frequencies that were chosen to correspond to the equivalent $^{60}$Co activity and reference [43] details the process for tuning the LED to match the $^{60}$Co source.

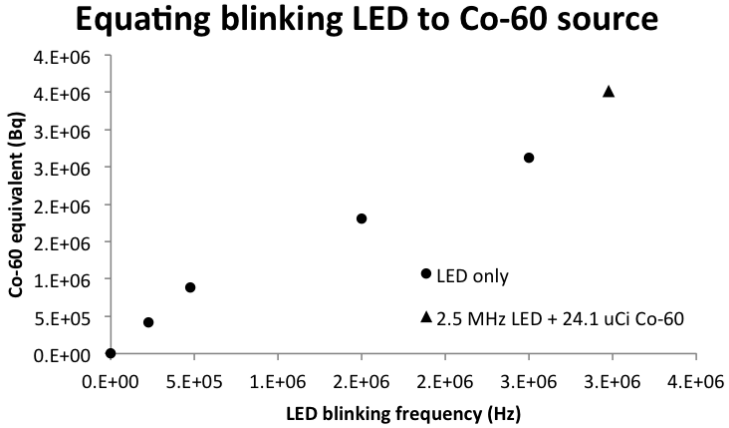


Figure 5.2: Equating LED blinking frequency to $^{60}$Co activity. Circles indicate purely LED spectra that were matched to the corresponding $^{60}$Co activity, while the triangle indicates the final data point for which an LED and a $^{60}$Co source were used to achieve the highest $^{60}$Co-equivalent value.

### Ambient background light level

To systematically test the level of light noise in the detector, a measure of the ambient light level was established. Normally, DAQ electronics integrate a triggered event and a pre-triggered pedestal 200 ns window, then subtract the two for the triggered event integral. Alternatively, if the DAQ were to be triggered externally (via a pulse generator) in a background-free environment, this would produce a very sharp Gaussian spectrum centered around zero photoelectrons because the pedestal and event window integrals would balance. Introducing noise into the system via a nearly-constant light level supplied by a green LED increases the probability that either the pedestal or event window will contain photoelectrons, increasing the width of the Gaussian distribution.

Fig. 5.3 shows two such externally triggered distributions which were obtained by triggering the detector with an external pulse generator. The most prominent feature of both distributions is the sharp and narrow peak centered about zero, which is the distribution of pedestal events. These events would not normally trigger the detector, as they are far below one photoelectron in energy. However, increasing the light noise level in the detector (represented by the red curve, which includes a high rate of $^{60}$Co events) broadens the wider tails distribution. For example, it becomes statistically more likely that two or more low-level

events pile up, creating a detected pulse of higher energy. The events in this narrow peak are referred to as *pedestal events*. The broader distribution at the tail of the pedestal events includes less probable but higher-energy events, such gammas, and the probability of these events increases dramatically with increasing gamma activity. Fig. 5.4 shows the detector response to a 30 kBq (0.82 $\mu$Ci) $^{252}$Cf, along with 0, 0.4, and 2.2 MBq $^{60}$Co-equivalent sources obtained with the help of a flashing LED. Increasing the ambient light noise level distorts the neutron detector response because of the unstable baseline. As the ambient gamma flux increases, the rate of pedestal events increases. A neutron event atop a baseline event will slightly distort the detected energy of that neutron event, having the cumulative effect of smearing out the measured neutron distribution. A small $^{60}$Co peak around 20 photoelectrons also begins to grow at high $^{60}$Co values. Some asymmetry is observed but not well understood.

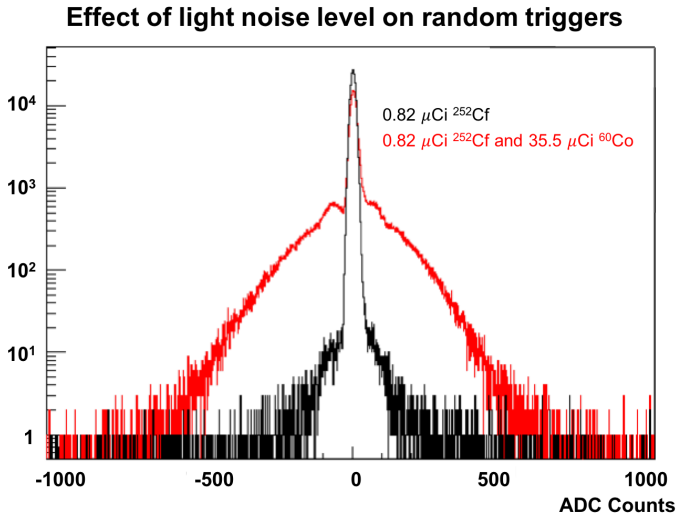


Figure 5.3: The black spectrum shows the ADC charge value of randomly-triggered events summed for all eight PMTs in the presence of a 30 kBq $^{252}$Cf source. The red curve shows the same with the addition of a 1.3 MBq (35.3 $\mu$Ci) $^{60}$Co source. The Gaussian widths of the sharp and narrow peak increases from $(9.45 \pm 0.03)$ ADC counts to $(10.77 \pm 0.04)$ ADC counts with the addition of $^{60}$Co.

Because neutron detection efficiency is obtained as a function of the neutron spectrum integral between 50 and 200 photoelectrons, the changing detector response spectrum shape will influence measured efficiency. Fig. 5.5 (left) shows the number of events between 50 and 200 photoelectrons (neutron-like events) for a $^{252}$Cf neutron source together with various amounts of gamma background (simulated with a flashing LED). Fig 5.5 (right) shows the same results with the $^{252}$Cf source absent (integral between 50 and 200 photoelectrons, with the same experimental parameters). The increase in counts between 50 and 200 pho-

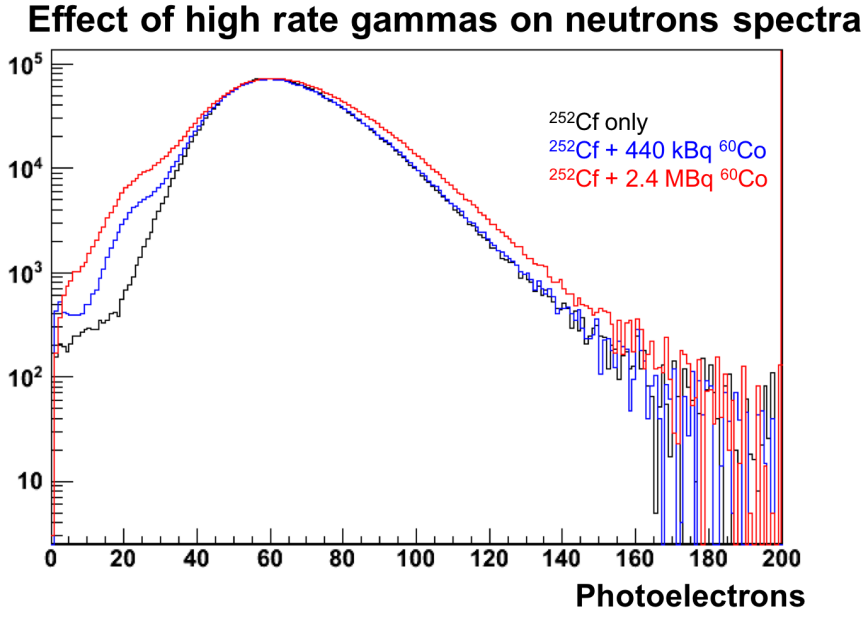


Figure 5.4: High threshold detector response to a 30 kBq (1 $\mu$Ci) $^{252}$Cf source and various $^{60}$Co activities. The black curve shows the detector response with no $^{60}$Co present, and the blue and red curves show the neutron response to the same $^{252}$Cf source in the presence of increasing gammas. All activities of $^{60}$Co were simulated with the use of a calibrated pulsing LED.

toelectrons can be attributed to two effects: the pileup of gamma events into the neutron region, and the broadening of the neutron spectrum. Although it is not wholly obvious from Fig. 5.4 that $^{60}$Co-equivalent events leak into the region above 50 photoelectrons, Fig. 5.5 (right) shows that counts are approximately equal up to $\sim$ 2.5M Bq $^{60}$Co-equivalent but dramatically increase at $\sim$ 3.5M Bq $^{60}$Co-equivalent. A decrease in counts from zero to 0.2 MBq $^{60}$Co is observed, but not fully understood. Because no neutron spectrum is present aside from background neutron events, the increase is due to $^{60}$Co-equivalent events that leak into the integrated region above 50 photoelectrons. Even if the energy of a given $^{60}$Co-equivalent event is below 50 photoelectrons, a pileup of two low-energy events can rise above this threshold. The second process that impacts the measured detection efficiency is the broadening of the $^{252}$Cf spectrum. While the LED-only plot (Fig. 5.5 right) remains roughly constant up to approximately 2.5 MBq $^{60}$Co-equivalent, including $^{252}$Cf (Fig. 5.5 left) increases the counts at a lower level of approximately 3.7 MBq $^{60}$Co-equivalent. This means that while the rate of false positive gammas becomes measurable at around 9.3 MBq $^{60}$Co-equivalent, the neutron detector response degradation begins at much lower ambient light noise levels of approximately 3.7 MBq $^{60}$Co-equivalent.

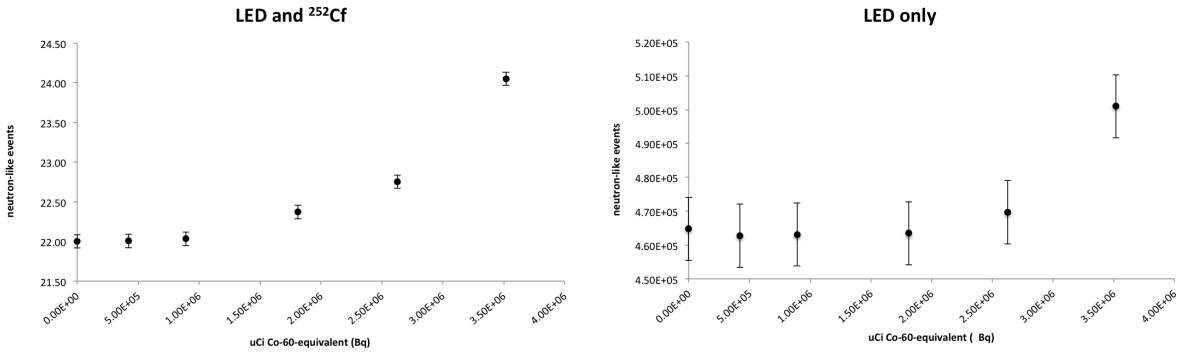


Figure 5.5: (left) Measured detector efficiency as a $^{252}$Cf source and various $^{60}$Co-equivalent levels, simulated by a flashing LED. The PMT threshold was set at a high value to minimize the triggered gamma events. Error bars represent the uncertainty in cosmic ray events due to atmospheric events. (right) The same experiment run without a $^{252}$Cf source present.

The consistency of detector performance can be evaluated from Fig. 5.5 (left). With a high PMT threshold and minimal source gammas, the detector's singles neutron detection efficiency is 22%, known to within 10% of the source neutron emission rate. Although the neutron detection efficiency changes slightly with the introduction of light noise, it is constant at (22% $\pm$ 1)% up to $\sim$ 2.5M Bq $^{60}$Co-equivalent.

Software padding is used in TeV gamma ray astronomy where the amount of ambient starlight present in the field of view may differ between on and off source data runs to equalize background noise between on and off source data runs [56]. The approach to measure the pedestal noise of the on and off source run, and to add noise in software to the least noisy run until they match. An algorithm was created to measure the baseline fluctuation (the width of the pedestal events, shown in Fig. 5.3) in the detector well and then add software padding to the neutron spectrum based on level of gammas in the detector. However, the algorithms utilized in TeV astronomy work only if the background is constant, so it may not be applicable to the WaND. Nonetheless, a more nuanced algorithm might prove useful in the future.

### 5.1.2 Simulation: spent fuel detector response

This study also attempted to determine the detector response to spent fuel, accomplished with the aid of a simulation. Reference [43] documents a preliminary analysis of spent fuel gamma detector response, but includes only gammas above 1.6 MeV. This study now offers a more detailed analysis including the entire spent fuel gamma spectrum and higher statistics.

A simulated spectrum of a single 20 cm spent fuel pin with a burnup of 30 GWd/t and a cooling time of 20 years was obtained from LANL [57] and used as a source term in the Geant4 simulation. Fig. 5.6 left shows the full 15-minute gamma spectrum, containing

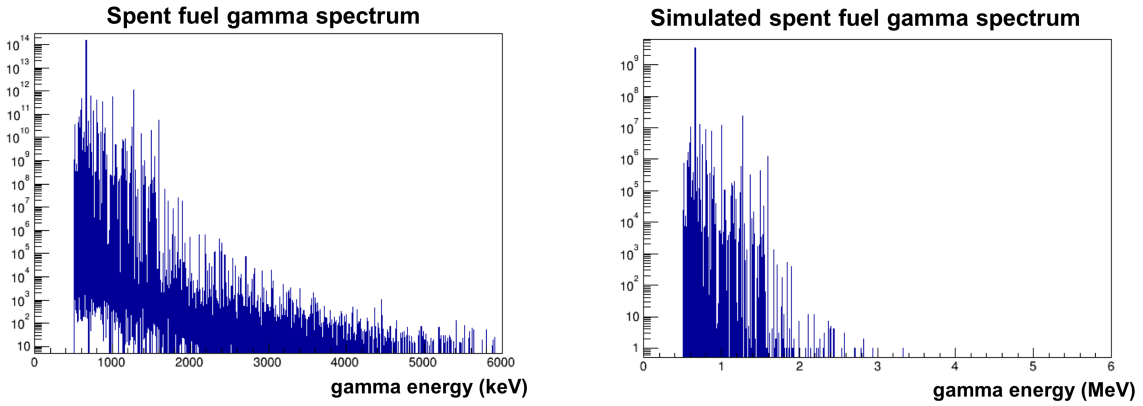


Figure 5.6: Fifteen minute simulated spent fuel gamma spectrum obtained from LANL [57]. (left) Gamma spectrum of spent fuel simulation source term. (right) Sampled gammas from spent fuel source shown in the left plot.

$1.6 \times 10^{14}$ gammas. Of those, $3.5 \times 10^{9}$ gammas were sampled for the simulation and their detector response simulated, resulting in 19.4 ms of equivalent acquisition time from the input spectrum, Fig. 5.6 right. The simulated spent fuel detector response is shown in Fig. 5.7. The Geant4 simulation does not include threshold effects, so the simulated spectrum differs substantially from the measured one at low photoelectron values (as these values would not trigger the detector). The detector response shows no events above 50 photoelectrons, so it might be possible to discriminate gammas from neutrons to a first-order approximation using a 50 photoelectron threshold [43]. The 19.4 ms of simulated spent fuel gamma activity corresponds to $6.5 \times 10^{8}$ detector response events above zero photoelectrons that will create a wash of low-energy wash of Cherenkov photons in the detector, increasing the pedestal width and artificially changing the measured detector efficiency, as shown in Fig. 5.5.

Fig. 5.6 left also demonstrates the dominance of 662 keV $^{137}$Cs gamma in older spent fuel. The WaND system is insensitive to low-energy gammas with a diminished probability of producing Compton scattered electrons above the 260 keV Cherenkov threshold, so it is essentially blind to $^{137}$Cs gammas [43].

## 5.2 Lead shielding as a gamma mitigation technique

Lead is often used as a gamma shield. As such, it was necessary to test the effect of lead shielding on gamma suppression and figure of merit (FOM), both experimentally and in simulation.

In order to verify the validity of the Geant4 simulation, the detector response to 0.9 MBq $^{60}$Co was compared with a simulation featuring varying thicknesses of lead shielding.

Fig. 5.8 shows the full simulated detector response to $^{60}$Co and spent fuel gammas with

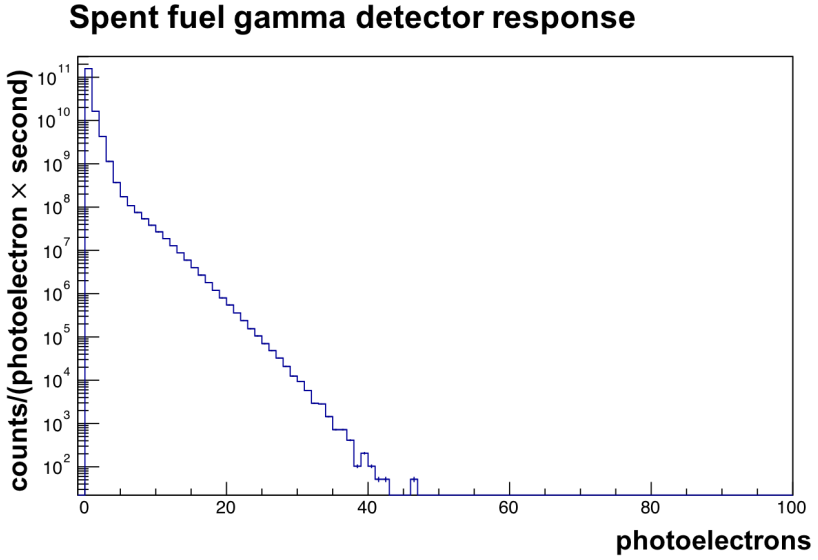


Figure 5.7: Detector response accumulated from the equivalent of 19.4 ms of detector run time to the spent fuel gamma source term shown in Fig. 5.6.

various lead shielding thicknesses. Fig. 5.5 previously showed that 4 MBq of $^{60}$Co demonstrated equivalent light levels, so the $^{60}$Co simulation data in Fig. 5.8 assumes 4 MBq. The spent fuel data assumes 19.2 ms of data for the same spent fuel source as shown in Section 5.1.2. The detector response, in terms of the total integrated detector response rate of photoelectrons per nanosecond, gives a parameter for comparison between $^{60}$Co and spent fuel.

Using photoelectrons per nanosecond as our key parameter, Fig. 5.8 shows that 80 millimeters of lead shielding effectively attenuates two orders of magnitude for $^{60}$Co and three orders of magnitude for spent fuel. Put another way, 70 mm of lead shielding attenuates the simulated 20 cm spent fuel sample gammas to the detector response level of a 4 MBq $^{60}$Co source without shielding, the level at which the ambient level begins to seriously deteriorate the detector response [43]. A negative consequence of adding lead shielding is that it reduces the FOM, often used to compare neutron counters, which is given by

$$FOM = \frac{\epsilon}{\sqrt{\tau}},$$

where $\epsilon$ is the absolute singles neutron detection efficiency and $\tau$ is the neutron capture time in $\mu$s. With no lead shielding and a high PMT trigger of (22% efficiency [43]), the measured neutron capture time is 14.3 $\mu$s and the FOM is 5.8. Introducing lead shielding into the detector well decreases the FOM by approximately 33% for 66 mm of lead shielding (the maximum lead shielding available experimentally), as shown in Fig. 5.9. Extrapolating a

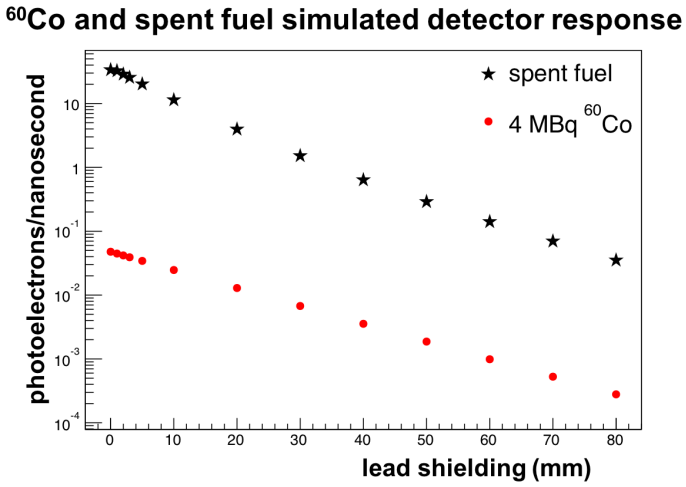


Figure 5.8: The average number of photoelectrons produced per nanosecond in the WaND detector as a function of lead shielding for a 4 MBq $^{60}$Co source compared to a simulated spent fuel source (see text).

linear relationship, 80 mm of lead shielding corresponds to a FOM of 3.4. By comparison, the High Efficiency Neutron Counter (HENC) – a Canberra neutron multiplicity counter that can be used for waste assay – boasts a FOM of 4.6 with no gamma shielding for nominal neutron counting operations. Note that the HENC FOM would likely also drop by a similar fraction if lead shielding were added.

## 5.3 Conclusion

This chapter details an analysis of the WaND system performed to determine its limitations with respect to ambient gamma backgrounds. A high ambient gamma flux creates a low-energy but constant ambient light level in the detector, which distorts the detector response to neutron capture events. It was determined that for a high PMT trigger threshold, $\sim 2.5$ MBq $^{60}$Co-equivalent distorts the measured neutron detector spectrum enough to artificially increase the measured detection efficiency, and $\sim 3.5$ MBq $^{60}$Co-equivalent begins to create false positive neutrons. In the presence of gammas, the WaND neutron detection efficiency is constant at 22% to within 1% up to $\sim 2.5$ MBq $^{60}$Co-equivalent. However, lead serves as an effective gamma shield – 70 mm of lead shielding attenuates two orders of magnitude of $^{60}$Co gammas and three orders of magnitude of spent fuel gammas, bringing the spent fuel gammas to a bearable level.

The applicability of the WaND to direct plutonium measurement of spent fuel was inves-

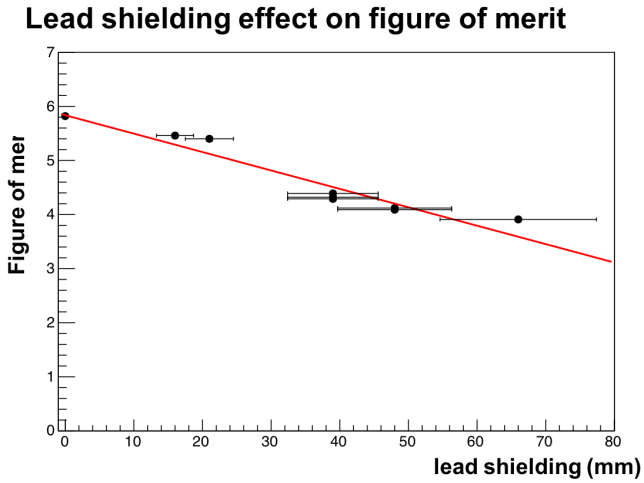


Figure 5.9: Experimentally-measured FOM dependence on lead thickness.

tigated. The WaND is insensitive to $^{137}$Cs gammas, which make up the majority of gamma activity from older spent fuel. It was shown through a combination of measurements and simulation that ∼70 mm of lead shielding could decrease the gamma activity to a bearable level for the spent fuel source shown in Section 5.1.2. It is therefore of interest to continue the investigation of direct plutonium measurement of spent fuel, but this is most likely not the best application for the detector.

# Chapter 6

# Conclusion and outlook

The Water Neutron Detector is a potential replacement for many helium-3 detector systems. Because the U.S. and the IAEA rely on the dwindling stockpiles of helium-3 for neutron detection, the need for alternate detector technology is becoming increasingly critical. While many candidate technologies suffer in detection efficiency or are hazardous, the WaND system is both highly efficient and non-hazardous. However, because the WaND system's detection characteristics are not typical of traditional neutron detectors – including low sensitivity to gammas and high neutron efficiency – two different applications were explored in this dissertation.

First, the WaND system sensitivity to trace quantities of plutonium was tested. This potentially has application measuring the residual plutonium content of waste contaminated with plutonium. For example, the commercially-available Antech N2223-220 High Efficiency Passive Neutron Drum Monitor is sensitive to 20-50 mg $^{240}\mathrm{Pu}_{eff}$ in 20 minutes. It is 2.1 m $\times$ 1.8 m $\times$ 3.3 m in dimension and relies on 128 24.5 mm $\times$ 1000 mm helium-3 tubes at 6 atmospheres [58]. This results in $\sim$360 liters of helium-3 at 1 atmosphere. At a market value of \$600-1000 per liter, the cost is \$216,000-360,000 for the helium-3 alone. The WaND system offers comparable neutron detection characteristics for a fraction of the cost and size, and is not impacted by a volatile commodity.

On the other extreme of plutonium measurement, application of the WaND system to the plutonium measurement of spent fuel was analyzed. However, it was concluded that although the WaND system is relatively insensitive to single spent fuel gammas, the extremely high flux causes a pileup of low-energy events that degrade the neutron signal. Because the shape of the neutron distribution is a measure of neutron efficiency, a degradation in shape destabilizes neutron counting. A noise-equalizing algorithm was implemented to balance the noise between high and low ambient background spectra, but without success. In particular, the noise-equalizing algorithm relies on an accurate measure of the relative ambient light noise between runs, such that an accurate measure of the relative ambient light noise of each run can be made and a correction applied. Ultimately, because nondestructive neutron spent fuel plutonium assay is still an open question and the WaND system is gamma-sensitive, more investigation is necessary to determine the WaND's applicability to plutonium measurement

in spent fuel. For example, the simulations were performed on a 20 cm long section of a spent fuel pin. However, the measurement of a much smaller spent fuel sample, combined with adequate lead shielding, may be possible.

Perhaps the most exciting feature of the WaND system is the homogeneous detection medium, which allows for a flexible form factor. While heterogeneous neutron detection systems rely on specific geometries and designs to maximize neutron detection probability, WaND technology is relatively open to different configurations. The homogeneous detector design allows the detector time response to be modeled with a single exponential die-away time constant. Also the WaND can in principle increase the gadolinium content further to have a very short die-away time. However, a limitation is that the WaND system must be of substantial size for high neutron detection efficiency because enough gammas from the gadolinium cascade must be detected. The system is nonetheless highly applicable in large-area systems. For example, while the water is susceptible to freezing in outdoor environments, WaND can be set up as a radiation portal monitor for cargo in indoor environments. Because of its sensitivity to minute quantities of plutonium, this technology is ideal for passive nuclear material assay. Another potential application is on-line neutron dosimetry of in proton therapy clinics. A version of WaND can be built into (or disguised in) a clinic wall to count the fast spallation neutrons that result from (p,n) reactions in the high-energy proton beam.

In application space, future work should focus on determining proper niches for the WaND system. Because of its unique detection attributes and flexible form factor, the WaND system can not only replace some existing helium-3 detectors, but can also be implemented in novel ways. While this dissertation focused on the proof of principle of this novel detector, a study of commercialization and applicability to a wide variety of detector niches should be performed.

Applicability of the WaND system for safeguards should be explored further. This includes a better understanding of detector capabilities and of safeguards policy. The isotope-identification algorithm should be expanded to identify more sources, as well as the potential for mixed sources. For example, it would be very interesting to measure various uranium or plutonium enrichment levels. The mass measurement algorithm should also be expanded to measure the mass of various isotopes.

Currently the U.S. supplies the IAEA with helium-3, but because of the increasing and volatile nature of the price of helium-3, it may be prudent for the IAEA to begin to invest in alternate neutron detection technologies. For example, an initial investment in the WaND may be offset by the prospect of not having to purchase helium-3 at a market premium in the future, or eventually running out of helium-3 in the far future. A cost-benefit analysis should be performed weighing potential initial investment into the WaND versus the increasing cost of helium-3. A major policy limitation is the credibility of IAEA inspections. Helium-3 is an accepted and well-understood neutron detection medium, and introducing a less-understood technology would have to be done slowly and carefully to ensure its credibility for all states. A thorough analysis should be undertaken to understand the policy implications of this new technology. Lastly, if the detector has some applicability to safeguards, the pathway

to implementation must be carefully studied by both detector developing parties and the IAEA.

In regards to fundamental detector development, this detector should be better understood. For example, it was determined that light noise level negatively effects neutron counting due to the presence of extremely high gamma sources. However, mitigating this may be possible. Potential remedies include a light-noise equalizing algorithm and a study of potential shielding materials. Lead was shown to be an effective shielding material, but the thickness and geometry should be optimized to decrease light noise while still maintaining neutron counting stability. Introducing a wavelength-shifting material in the detector may also increase neutron efficiency.

# Appendix A

# Neutron multiplicity distribution of selected isotopes

Table A.1: Tabulated induced (i.f.) and spontaneous fission (s.f.) neutron multiplicities of selected isotopes (adapted from Ref. [25]).

| $P(\nu)$ | $^{235}$U | $^{238}$Pu | $^{240}$Pu | $^{242}$Pu | $^{242}$Cm | $^{244}$Cm | $^{252}$Cf |
|---|---|---|---|---|---|---|---|
| | i.f. | s.f. | s.f. | s.f. | s.f. | s.f. | s.f. |
| 0 | 0.033 | 0.054 | 0.066 | 0.068 | 0.021 | 0.015 | 0.002 |
| 1 | 0.174 | 0.205 | 0.232 | 0.23 | 0.147 | 0.116 | 0.026 |
| 2 | 0.335 | 0.38 | 0.329 | 0.334 | 0.327 | 0.3 | 0.127 |
| 3 | 0.303 | 0.225 | 0.251 | 0.247 | 0.327 | 0.333 | 0.273 |
| 4 | 0.123 | 0.108 | 0.102 | 0.099 | 0.138 | 0.184 | 0.304 |
| 5 | 0.028 | 0.028 | 0.018 | 0.018 | 0.037 | 0.043 | 0.185 |
| 6 | 0.003 | | 0.002 | 0.003 | 0.003 | 0.009 | 0.066 |
| 7 | | | | | 0.001 | | 0.015 |
| 8 | | | | | | | 0.002 |
| $\nu_1$ | | 2.21 | 2.156 | 2.145 | 2.54 | 2.72 | 3.757 |
| $\nu_2$ | | 3.957 | 3.825 | 3.794 | 5.132 | 5.939 | 11.962 |
| $\nu_3$ | | 5.596 | 5.336 | 5.317 | 8.036 | 10.101 | 31.812 |

# Appendix B

# Detection medium constituents

Table B.1: WaND detection medium isotopics.

| | isotope | natural abundance (%) |
|---|---|---|
| Hydrogen | $^{1}$H | 99.9885 |
| | $^{2}$H | 0.0115 |
| Oxygen | $^{16}$O | 99.757 |
| | $^{17}$O | 0.038 |
| | $^{18}$O | 0.205 |
| Chlorine | $^{35}$Cl | 75.76 |
| | $^{37}$Cl | 24.24 |
| Gadolinium | $^{152}$Gd | 0.20 |
| | $^{154}$Gd | 2.18 |
| | $^{155}$Gd | 14.80 |
| | $^{156}$Gd | 20.47 |
| | $^{157}$Gd | 15.65 |
| | $^{158}$Gd | 24.84 |
| | $^{160}$Gd | 21.86 |

# Appendix C

# Neutron interaction cross sections

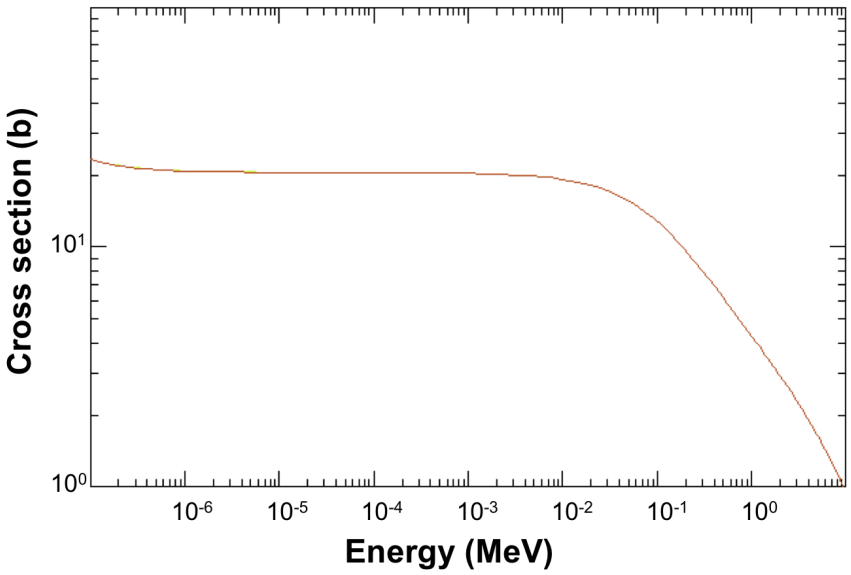


Figure C.1: Total neutron interaction $^{1}$H cross section. Elastic scattering dominates the total cross section for the energy range given.

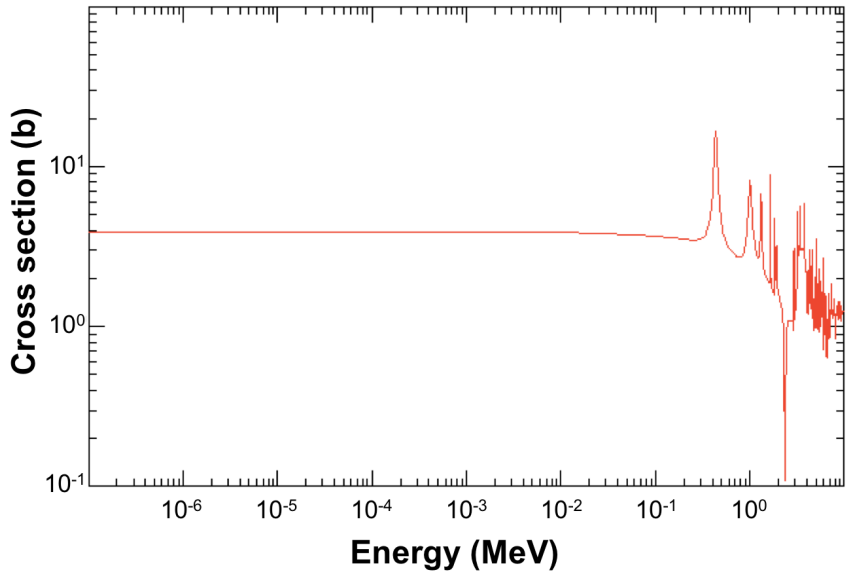


Figure C.2: Total neutron interaction $^{16}$O cross section.

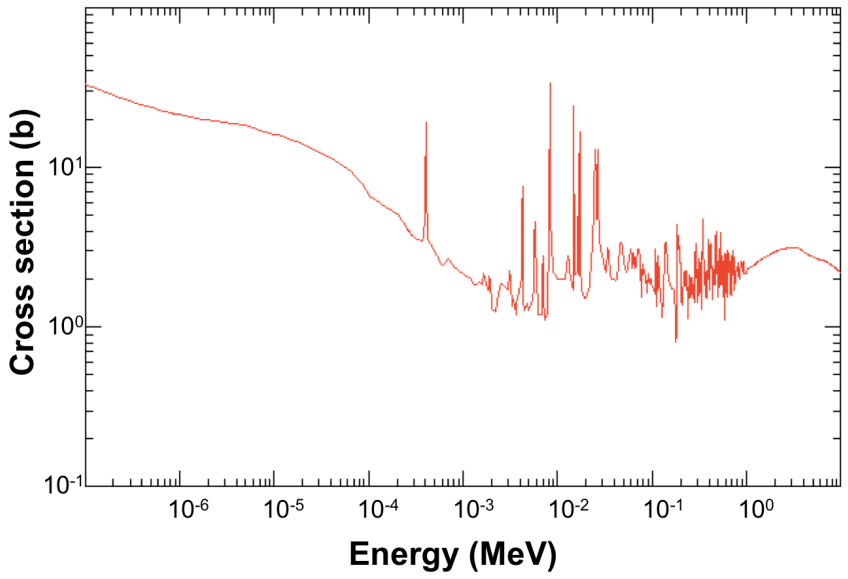


Figure C.3: Total natural chlorine neutron interaction cross section.

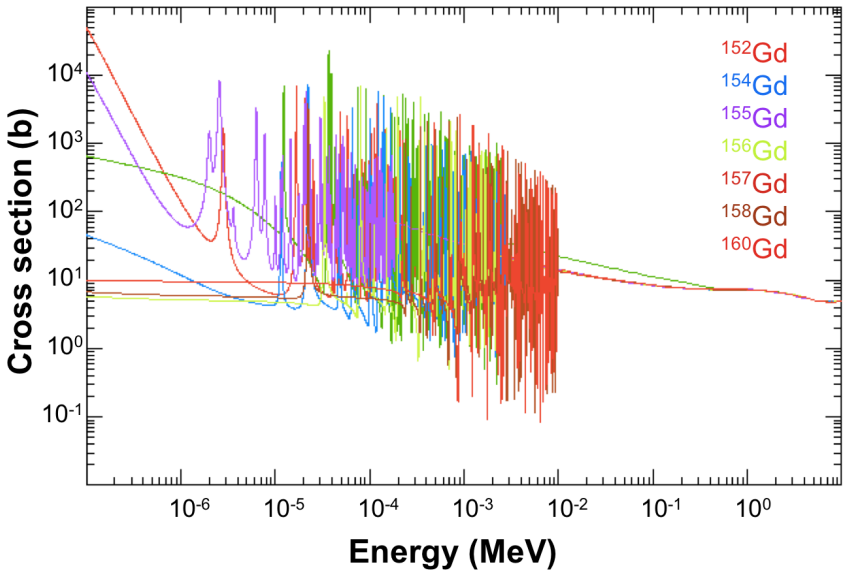


Figure C.4: Total isotopic gadolinium neutron interaction cross section.

# Bibliography


[1] John F. Kennedy. *News Conference*. Mar. 1963.

[2] Dwight D. Eisenhower. *Atoms for Peace Speech*. Dec. 1953.

[3] *Treaty on the Non-Proliferation of Nuclear Weapons*. 1970.

[4] *The Statute of the IAEA*. Oct. 1956.

[5] *Safeguards Agreements*. IAEA. URL: `https://www.iaea.org/safeguards/safeguards-legal-framework/safeguards-agreements`.

[6] *The Structure and Content of Agreements Between the Agency and States Required in Connection with the Treaty on the Non-proliferation of Nuclear Weapons (INFCIRC/153)*. June 1972.

[7] *IAEA Safeguards Glossary*. 2002.

[8] Mark M. Pickrell et al. "The IAEA Workshop on Requirements and Potential Technologies for Replacement of helium-3 Detectors in IAEA Safeguards Applications". In: *Journal of Nuclear Materials Management* 41.2 (2013), pp. 14–29.

[9] James E. Doyle. *Nuclear Safeguards, Security, and Nonproliferation*. Elsevier, 2008.

[10] S. J. Johnson et al. "Development of the Safeguards Approach for the Rokkasho Reprocessing Plant". In: *IAEA-SM-367/8/01* ().

[11] M. Zendel et al. "Nuclear Safeguards Verification Measurement Techniques". In: *Handbook of Nuclear Chemistry*. Ed. by A. Vértes et al. 2011.

[12] *Statement of Dr. William F. Brinkman, Director of the Office of Science for the U.S. Department of Energy before the Subcommittee on Investigations and Oversight Committee on Science and Technology, U.S. House of Representatives, House of Representatives Cong.* 2010.

[13] Daniel A. Shea and Daniel Morgan. "The Helium-3 Shortage: Supply, Demand, and Options for Congress". In: *Congressional Research Service* 41.7-5700 (Dec. 2010).

[14] Hisham Zerriffi. "Tritium: The environmental, health, budgetary, and strategic effects of the Department of Energys decision to produce tritium". In: *Institute for Energy and Environmental Research* 88 (1996).

[15] "Nuclear Weapons: National Nuclear Security Administration Needs to Ensure Continued Availability of Tritium for the Weapons Stockpile". In: *US Government Accountability Office* GAO-11-100 (Oct. 2010).

[16] Richard T. Kouzes, Azaree T. Lintereur, and Edward R. Siciliano. "Progress in Alternative Neutron Detection to Address the Helium-3 Shortage". In: *Nuclear Instruments and Methods in Physics Research A* 784 (June 2015), pp. 172–175.

[17] "Managing Critical Isotopes: Weaknesses in DOE's Management of Helium-3 Delayed the Federal Response to a Critical Supply Shortage". In: *US Government Accountability Office* GAO-11-472 (Sept. 2011).

[18] Adrian Cho. "Helium-3 Shortage Could Put Freeze On Low-Temperature Research". In: *Science* 326.5954 (2009), pp. 778–779.

[19] David Kramer. "For some, helium-3 supply picture is brightening". In: *Physics Today* 64.5 (2011).

[20] Brian K. Castle et al. "Plutonium Discharge Rates and Spent Nuclear Fuel Inventory Estimates for Nuclear Reactors Worldwide". In: *INL/EXT-12-27150* (Sept. 2012).

[21] Harold A. Feiveson et al. *Unmaking the Bomb: A Fissile Material Approach to Nuclear Disarmament and Nonproliferation*. 2014.

[22] S. J. Tobin, et al. "Next Generation Safeguards Initiative Research to Determine the Pu Mass in Spent Fuel Assemblies: Purpose, Approach, Constraints, Implementation, and Calibration". In: *Nuclear Instruments and Methods in Physics Research A* 652 (2011), pp. 73–75.

[23] Kenneth S. Krane and David Halliday. *Introductory Nuclear Physics*. 3rd ed. New York: Wiley, 1988.

[24] *Nuclear Binding Energy*. URL: `https://en.wikipedia.org/wiki/Nuclear_binding_energy`.

[25] Doug Reilly et al. "Passive Nondestructive Assay Manual - PANDA". In: *NUREG/CR-5550 LA-UR-90-732* (Mar. 1991).

[26] "Applications Guide to Neutron Multiplicity Counting". In: *LA-13422-M* (1998). Ed. by Jeff Skiby.

[27] N. Ensslin et al. "Passive Neutron Multiplicity Counting". In: *LA-UR-07-1402* (2007).

[28] Michael L'Annunziata. *Handbook of Radioactivity Analysis*. 3rd ed. San Diego: Academic Press, 2012.

[29] *Chart of Nuclides*. National Nuclear Data Center. URL: `http://www.nndc.bnl.gov/chart/`.

[30] *What Are the Attributes of Nuclear Materials?* Nuclear Safeguards Education Portal, Texas AM Engineering Experiment Portal. Jan. 2014. URL: http://nsspi.tamu.edu/nssep/courses/basic-radiation-detection/introduction/what-are-the-attributes-of-nuclear-materials/3)-what-are-the-attributes-of-nuclear-materials.

[31] L. F. Nakae et al. "Recent Developments in Fast Neutron Detection and Multiplicity Counting with Liquid Scintillator". In: *Proceedings of the Second Japan IAEA Workshop on Advanced Safeguards Technology for the Future Nuclear Fuel Cycle in Tokai, Japan* (2011).

[32] Glen F. Knoll. *Radiation Detection and Measurement*. 4th ed. John Wiley and Sons, Inc., 2010.

[33] *Nuclear Data Center at KAERI*. URL: http://atom.kaeri.re.kr:8080/cgi-bin/endfplot.pl.

[34] A. P. Simpson et al. "A Review of Neutron Detection Technology Alternatives to Helium-3 for Safeguards Applications". In: *INMM 52nd Annual Meeting, Palm Desert, California* (2011).

[35] United Nations Secretariat. "Committee of Experts on the Transport of Dangerous Goods and on the Globally Harmonized System of Classification and Labeling of Chemicals; Sub-Committee of Experts on the Transport of Dangerous Goods". In: (2012).

[36] *Neutrino Detection*. URL: http://t2k-experiment.org/neutrinos/neutrino-detection/.

[37] R. Becker-Szendy et al. "Search for muon neutrino oscillations with the Irvine-Michigan-Brookhaven detector". In: *Phys. Rev. Lett.* 69 (7 1992), pp. 1010–1013.

[38] S. Giani et al. *Astroparticle, Particle, Space Physics, and Detectors for Physics Applications*. Vol. 7. 2012.

[39] S. Fukuda et al. "The Super-Kamiokande detector". In: *Nuclear Instruments and Methods in Physics Research Section A* 501.2?3 (2003), pp. 418 –462.

[40] *Kamioka Observatory*. Brochure.

[41] M. Askins et al. "The Physics and Nuclear Nonproliferation Goals of WATCHMAN: A WAter CHerenkov Monitor for ANtineutrinos". In: *arXiv* (2015). arXiv:1502.01132.

[42] M. Sweany et al. "Large-scale gadolinium-doped water Cherenkov detector for nonproliferation". In: *Nuclear Instruments and Methods in Physics Research Section A* 654.1 (2011), pp. 377 –382.

[43] Steven Dazeley et al. "A water-based neutron detector as a well multiplicity counter". In: *Nuclear Instruments and Methods in Physics Research Section A* 771 (2015). ISSN: 0168-9002.

[44] S.A. Dazeley et al. *Gadolinium-Doped Water Cerenkov-Based Neutron and High Energy Gamma-Ray Detector and Radiation Portal Monitoring System*. US Patent 8,373,133. 2013.

[45] Hirokazu Ishino for the Super-Kamiokande Collaboration. "Gadolinium study for Super-Kamiokande". In: *Proceedings of the 31st International Cosmic Ray Conference, Łódź, Poland* (2009).

[46] Gábor L. Molnár, ed. *Handbook of Prompt Gamma Activation Analysis with Neutron Beams*. Chemical Research Centre, Budapest, Hungary, 2004.

[47] Claus Grupen and Boris Shwartz. *Particle Detectors*. 2nd ed. Cambridge Monographs on Particle Physics, Nuclear Physics, and Cosmology, 2008.

[48] Gregory S. Mitchell et al. "In vivo Cerenkov Luminescence Imaging: A New Tool for Molecular Imaging". In: *Philosophical Transactions of the Royal Society A* (2011).

[49] *Photocathode Area Photomultiplier Tubes*. Hamamatsu brochure.

[50] J. Allison et al. "Geant4 developments and applications". In: *Nuclear Science, IEEE Transactions on* 53.1 (2006), pp. 270–278.

[51] S. Agostinelli et al. "Geant4 - a simulation toolkit". In: *Nuclear Instruments and Methods in Physics Research Section A* 506.3 (2003), pp. 250 –303.

[52] S. Dazeley et al. "Performance Characterization of a Water-based Multiplicity Counter". In: *Institute of Nuclear Materials Management 55th Annual Meeting Conference Proceedings* (2014).

[53] K. Eguchi et al. (KamLAND Collaboration). "First Results from KamLAND: Evidence for Reactor Antineutrino Disappearance". In: *Phys. Rev. Letters* 90 (2 2003).

[54] T. E. Valentine. "Evaluation of Prompt Fission Gamma Rays for Use in Simulating Nuclear Safeguard Measurements". In: *Oak Ridge National Laboratory* ORNL/TM-1999/300 (1999).

[55] V. V. Verbinski, Hans Weber, and R. E. Sund. "Prompt Gamma Rays from $^{235}$U$(n, f)$, $^{239}$Pu$(n, f)$, and Spontaneous Fission of $^{252}$Cf". In: *Phys. Rev. C* 7 (1973), pp. 1173–1185.

[56] G.P. Rowell et al. "The treatment of skynoise in VHE gamma ray astronomy data". In: *Astroparticle Physics* 7.1-2 (1997), pp. 35–48.

[57] *Nuclear Nonproliferation Division: Safeguards and Security Systems Group*. URL: `http://www.lanl.gov/orgs/ndo/n4/`.

[58] Antech. *High Efficiency Passive Neutron Drum Monitor brochure*.